

PAOLO PIVATO

ANALYSIS AND CHARACTERIZATION OF WIRELESS POSITIONING
TECHNIQUES IN INDOOR ENVIRONMENT

ANALYSIS AND CHARACTERIZATION OF WIRELESS
POSITIONING TECHNIQUES IN INDOOR ENVIRONMENT



International Doctoral School in Information and Communication Technology
XXV Cycle
Department of Information Engineering and Computer Science
University of Trento

Doctoral Dissertation of:
PAOLO PIVATO

Advisor:

PROF. DARIO PETRI

Co-Advisor:

PROF. LUIGI PALOPOLI

November 2012

EXAMINATION COMMITTEE:

prof. DARIO PETRI	Chair, Advisor
prof. LUIGI PALOPOLI	Co-Advisor
prof. CLAUDIO NARDUZZI	Member
prof. ANTONIO MOSCHITTA	Member

Paolo Pivato: *Analysis and Characterization of Wireless Positioning Techniques in Indoor Environment*, Ph.D. in Information and Communication Technologies - Electronics Area, © November 2012

PUBLICATIONS

INTERNATIONAL JOURNALS

- [J1] P. Pivato, L. Palopoli, and D. Petri, "Accuracy of RSS-Based Centroid Localization Algorithms in an Indoor Environment," *IEEE Transactions on Instrumentation and Measurement*, vol. 60, no. 10, pp. 3451–3460, Oct. 2011.
- [J2] D. Macii, A. Colombo, P. Pivato, and D. Fontanelli, "A Data Fusion Technique for Wireless Ranging Performance Improvement," *IEEE Transactions on Instrumentation and Measurement*, vol. 61, no. 1, pp. 27–37, Jan. 2013.

INTERNATIONAL CONFERENCES

- [C1] P. Pivato, S. Dalpez, and D. Macii, "Performance Evaluation of Chirp Spread Spectrum Ranging for Indoor Embedded Navigation Systems," in *Proc. 7th IEEE International Symposium on Industrial Embedded Systems (SIES 2012)*, Karlsruhe, Germany, Jun. 2012, pp. 1–4.
- [C2] C. M. De Dominicis, P. Ferrari, E. Sisinni, A. Flammini, P. Pivato, and D. Macii, "Timestamping Performance Analysis of IEEE 802.15.4a Systems based on SDR Platforms," in *Proc. IEEE International Instrumentation and Measurement Technology Conference (I2MTC 2012)*, Graz, Austria, May 2012, pp. 2034–2039.
- [C3] P. Pivato, S. Dalpez, D. Macii, and D. Petri, "A Wearable Wireless Sensor Node for Body Fall Detection," in *Proc. IEEE International Workshop on Measurement and Networking (M&N 2011)*, Anacapri, Italy, Oct. 2011, pp. 116–121.
- [C4] D. Macii, P. Pivato, and F. Trenti, "A Robust Wireless Proximity Detection Techniques based on RSS and ToF measurements," in *Proc. IEEE International Workshop on Measurement and Networking (M&N 2011)*, Anacapri, Italy, Oct. 2011, pp. 31–36.
- [C5] P. Pivato, L. Fontana, L. Palopoli, and D. Petri, "Experimental Assessment of a RSS-based Localization Algorithm in Indoor Environment," in *Proc. IEEE International Instrumentation and Mea-*

surement Technology Conference (I2MTC 2010), Austin, TX, USA, May 2010, pp. 416–421.

- [C6] M. Corra, L. Zuech, C. Torghele, P. Pivato, D. Macii, and D. Petri, “WSNAP: a Flexible Platform for Wireless Sensor Networks Data Collection and Management,” in *Proc. IEEE Workshop on Environmental, Energy, and Structural Monitoring Systems (EESMS 2009)*, Crema, Italy, Sep. 2009, pp. 1–7.

ACKNOWLEDGMENTS

I would like to thank my advisor, prof. Dario Petri, and my co-advisor, prof. Luigi Palopoli, for their valuable guidance and support during my Ph.D., teaching me the values of objectivity and independence in doing research.

A dutiful thank you to prof. David Macii for his professionalism and humanity shown to me several times.

CONTENTS

1	INTRODUCTION	1
1.1	Objectives and Novel Contribution of the Research . . .	2
1.2	Thesis Organization	3
2	STATE OF THE ART	5
2.1	Introduction	5
2.2	Positioning Techniques	6
2.2.1	Lateration	6
2.2.2	Angulation	7
2.3	Wireless Ranging	8
2.3.1	Received-Signal-Strength Ranging	9
2.3.2	Time-of-Flight Ranging	11
2.4	Related Work	13
2.4.1	Infrared	13
2.4.2	Ultrasound	14
2.4.3	Radio-frequency	14
3	RSS-BASED RANGING AND POSITIONING IN INDOOR EN- VIRONMENT	17
3.1	Introduction	17
3.2	Measurement Context	19
3.3	RF Channel Characterization	20
3.3.1	Indoor RF Channel Propagation Model	20
3.3.2	RF Channel Parameters Estimation	23
3.4	Localization Algorithms	26
3.4.1	Weighted Centroid Localization	26
3.4.2	Relative Span Exponential Weighted Localization	30
3.5	Conclusion	36
4	HYBRID RSS-RTT METHOD FOR RANGING PERFORMANCE IMPROVEMENT	39
4.1	Introduction	39
4.2	Uncertainty of RSS and RTT Ranging Techniques . . .	40
4.3	Data Fusion Algorithm for Distance Estimation	43
4.3.1	Data Acquisition and Filtering	44
4.3.2	System Model	47

4.3.3	Kalman Filter Definition	48
4.3.4	Data Fusion	49
4.4	Hardware Platform Description	49
4.5	Experimental Results	52
4.5.1	Uncertainty Evaluation of Individual Quantities	52
4.5.2	Accuracy Analysis in Dynamic Conditions . . .	56
4.6	Conclusion	60
5	TIMESTAMPING OF IEEE 802.15.4A CSS SIGNALS	63
5.1	Introduction	63
5.2	Overview of IEEE 802.15.4a Chirp Spread Spectrum . .	66
5.3	Theoretical Model	70
5.4	Uncertainty Analysis and Symbol Timestamp Definition	72
5.4.1	Incoherent baseband sampling and finite tem- poral resolution	73
5.4.2	Wideband Noise	74
5.4.3	Frequency Offsets	74
5.4.4	Multipath Propagation	78
5.4.5	Definition of Symbol Timestamp	80
5.5	Experimental Characterization	81
5.5.1	Experimental Setup	81
5.5.2	Performance Metrics	83
5.6	Experimental Results	84
5.7	Conclusion	86
6	CONCLUSION	89
6.1	Contributions	91
6.2	Future Research Work	92
A	EQUIVALENCE BETWEEN REWL AND WCL ALGORITHMS	93
	BIBLIOGRAPHY	95

LIST OF FIGURES

Figure 2.1	Lateration positioning method.	7
Figure 2.2	Angulation positioning method.	8
Figure 3.1	Location test points within the <i>Domotic Appli- cation Lab.</i>	18
Figure 3.2	RSS measurements and related channel models	22
Figure 3.3	RSS error histograms	25
Figure 3.4	WCL distance error	29
Figure 3.5	WCL algorithm errors cumulative histograms	33
Figure 3.6	REWL distance error	35
Figure 3.7	REWL algorithm errors cumulative histograms	37
Figure 4.1	Distance estimation algorithm block diagram .	45
Figure 4.2	Functional block diagram and snapshot of the Mobile Tracking System	50
Figure 4.3	RSS- and ToF-based distance measurements stan- dard uncertainty and RMSE values	54
Figure 4.4	Average probability of using the heuristic cri- terion as a function of the MA window size . .	55
Figure 4.5	Average RMSE patterns related to different RSS- and ToF-based distance estimators	55
Figure 4.6	Histogram of the measured sampling time val- ues.	57
Figure 4.7	Measurement results obtained with the pro- posed data fusion algorithm	59
Figure 4.8	Distance uncertainty box-and-whiskers plot: tar- get moving along a straight line	61
Figure 4.9	Distance uncertainty box-and-whiskers plot: tar- get moving along an arc of circle	61
Figure 5.1	Qualitative shape of four different IEEE 802.15.4a CSS symbols as a function of time	67
Figure 5.2	IEEE 802.15.4a subchirp correlation pulse for $k = 2$	72
Figure 5.3	Effect of AWGN on timestamping jitter	75
Figure 5.4	Mean value and standard deviation of ϵ_o as a function of different systematic transmitter- receiver frequency offsets for subchirps $k = 2$.	77

Figure 5.5	Distribution of ε_p in the presence of a strong multipath interference for a mean interarrival time equal to 5 ns	79
Figure 5.6	Definition and benefits of IEEE 802.15.4a CSS frame timestamping at the symbol level.	81
Figure 5.7	Symbol timestamping on the timescales of transmitter and receiver	82
Figure 5.8	Distribution of the symbol timestamping errors in the case of data transfers between two N210 platforms	87

LIST OF TABLES

Table 2.1	Comparison of indoor positioning systems	14
Table 3.1	Log-normal channel parameters	24
Table 3.2	WCL algorithm mean distance error	31
Table 3.3	WCL algorithm RMS distance error	31
Table 3.4	REWL algorithm mean distance error	34
Table 3.5	REWL algorithm RMS distance error	34
Table 5.1	Sub-band center frequencies, chirping directions and temporal parameter of subchirps	69
Table 5.2	Post-interpolation errors for 10 different fractional delays between 0 and T_s	73
Table 5.3	Single subchirp timestamping accuracy analysis.	84
Table 5.4	Symbol timestamping accuracy analysis.	85

ACRONYMS AND ABBREVIATIONS

2D	two-dimensional
3D	three-dimensional
AAL	ambient assisted living
ACK	acknowledgement

ADC	analog-to-digital converter
AoA	angle-of-arrival
ATS	Average TimeSynch
AWGN	additive white Gaussian noise
BS	base station
CL	centroid localization
COTS	commercial off-the-shelf
CRB	Crámer-Rao bound
CSMA	carrier sense multiple access
CSMA-CA	carrier sense multiple access with collision avoidance
CSS	chirp spread spectrum
DAC	digital-to-analog converter
DCR	direct conversion receiver
DDC	digital down-converter
DQPSK	differential quadrature phase-shift keying
DUC	digital up-converter
ENBW	equivalent noise bandwidth
FA	fixed anchor
FIR	finite impulse response
FPGA	field programmable gate array
FTSP	Flooding Time Synchronization Protocol
GNSS	global navigation satellite system
GPS	global positioning system
ID	identification data
IEEE	Institute of Electrical and Electronic Engineers
IIR	infinite impulse response
IMS	instrumentation scientific and medical

ISI	intersymbol interference
KF	Kalman filter
KF A	Kalman filter A
KF B	Kalman filter B
LOS	line-of-sight
LR-WPAN	low-rate wireless personal area network
LSM	least squares method
MA	moving-average
MAC	media access control
MCU	microcontroller unit
MT	mobile target
MTS	mobile tracking system
NLOS	non-line-of-sight
OWR	one-way ranging
PAN	personal area network
PDA	personal device assistant
PHY	physical layer
PTP	Precision Time Protocol
RAM	random-access memory
RBS	Reference-Broadcast Synchronization
REWL	relative-span exponential weighted localization
RF	radio-frequency
RFID	radio-frequency identification
RMS	root-mean square
RMSE	root-mean-square error
RSS	received-signal-strength
RSSI	received-signal-strength indicator

RTT	round-trip time
RX	receiver
SD	secure digital
SDR	software-defined radio
SFD	start frame delimiter
SNR	signal-to-noise ratio
SPI	serial peripheral interface
TDC	time-to-digital converter
TDoA	time-difference-of-arrival
ToA	time-of-arrival
ToF	time-of-flight
TDMA	time-division multiple access
TWR	two-way ranging
TX	transmitter
USB	universal serial bus
USRP	universal software radio peripheral
UWB	ultra-wide band
WCL	weighted centroid localization
WLAN	wireless local area network
WSN	wireless sensor network

INTRODUCTION

INDOOR POSITIONING, also referred to as *indoor localization*, shall be defined as the process of providing accurate people or objects coordinates inside a covered structure, such as an airport, an hospital, and any other building.

The applications and services which are enabled by indoor localization are various, and their number is constantly growing. Industrial monitoring and control, home automation and safety, security, logistics, information services, ubiquitous computing, health care, and ambient assisted living (AAL) are just a few of the domains that indoor positioning technology can benefit. A significant example is offered by local information pushing. In this case, a positioning system sends information to a user based on her/his location. For instance, a processing plant may push workflow information to employees regarding operating and safety procedures relevant to their locations in the plant. The positioning system tracks each employee, and has knowledge of the floor plan of the facility as well as the procedures. When an employee walks inside a defined perimeter of a particular area, such as packaging department, the positioning systems displays on the user's personal device assistant (PDA) information regarding the work expected to be done in that area. This significantly increases efficiency and safety by ensuring that employees follow carefully designed guidelines. Location-enabled applications like this are becoming commonplace and will play important roles in our everyday life.

The design of a positioning system for indoor applications is to be regarded as a challenging task. In fact, the global positioning system (GPS) is a great solution for outdoor uses, but its applicability is strongly limited indoors because the signals coming from GPS satellites cannot penetrate the structure of most buildings. For this reason, considerable research interest for alternative non-satellite-based indoor positioning solutions has arisen in the last years.

Actually, the positioning problem is strictly related with the measurement of the distance between the object to be located and a number of landmarks with known coordinates. Then, the position of the

target is commonly determined by means of appropriate statistical or geometrical algorithms.

Several approaches have been proposed, and various are the fundamental technologies that have been used so far. Today, distance measurement between two objects can be easily obtained by using laser-, optical- and ultrasounds-based devices. However, evident drawbacks of these systems are their sensitivity to line-of-sight (LOS) constraint, and the strict object-to-object bearing requirement. The latter becomes an even worse downside when the topology of the system dynamically changes due to mobility of the target.

On the other hand, wireless-based ranging solutions are more insensitive to obstacles and non-alignment condition of devices. In addition, they may take advantage of existing radio modules and infrastructures used for communications. Accordingly, the ever growing popularity of mobile and portable embedded devices provided with wireless connectivity has encouraged the study and the development of radio-frequency (RF)-based positioning techniques. The core of such systems is the measurement of distance-related parameters of the wireless signal.

The two most common approaches for wireless ranging are based on received-signal-strength (RSS) and message time-of-flight (ToF) measurements, respectively. In particular:

- the RSS-based method relies on the relationship between the measured received signal power and the transmitter-receiver distance, assuming that the signal propagation model and the transmitted power are known;
- the ToF-based technique leans on the measured signal propagation time and the light speed, owing to the fundamental law that relates distance to time.

1.1 OBJECTIVES AND NOVEL CONTRIBUTION OF THE RESEARCH

The work presented in this dissertation is aimed at investigating and defining novel techniques for positioning in indoor environment based on wireless distance measurements.

In particular, this study is devoted to the analysis and in depth evaluation of the use of RSS and ToF measurements for different indoor positioning applications. State of the art techniques relying on RSS- and ToF-based ranging methods have already proven to be effective

for the localization of objects inside buildings. Nevertheless, several limitations exist (e.g., on the accuracy of the ranging, its impact on localization algorithms, etc.).

The work presented in this dissertation attempts to:

1. investigate the main sources of uncertainty affecting RSS- and ToF-based indoor distance measurement;
2. analyze the impact of ranging error on the accuracy of positioning;
3. propose, on the basis of the understanding gained from 1. and 2., novel and effective systems in order to overcome the above-mentioned limitations and improve localization performance.

The novel contributions of this thesis can be summarized as follows:

- In-depth analysis of both RSS- and ToF-based distance measurement techniques, in order to assess advantages and disadvantages of each of them.
- Guidelines for using different ranging methods in different conditions and applications.
- Implementation and field testing of a novel data fusion algorithm combining both RSS and ToF techniques to improve ranging accuracy.
- Theoretical and simulation-based analysis of chirp spread spectrum (CSS) signals for low-level timestamping.
- Experimental assessment of CSS-based timestamping as key enabler for high accuracy ToF-based ranging and time synchronization.

1.2 THESIS ORGANIZATION

This thesis is organized in six Chapters, including the present one, and one Appendix.

[Chapter 2](#) presents some fundamental concepts of positioning and introduces the basic definitions and terminology that we will use throughout this study. In addition, for the sake of clarity, we establish a generalized scenario describing the tasks that a positioning system is expected to perform. Moreover, a survey of significant works concerning indoor localization based on wireless techniques is given.

[Chapter 3](#) analyze the accuracy of indoor localization based on RSS measurements in a wireless sensor network (WSN). Two different classes of low-computational-effort algorithms based on the centroid concept are considered. The different sources of measurement uncertainty are investigated by means of theoretical simulations and experimental results.

[Chapter 4](#) examines in detail the RSS and ToF methods in order to evaluate the main uncertainty contributions affecting either measurement procedure. This preliminary analysis serves as the basis for the proposal of a new data fusion algorithm combining both techniques in order to improve ranging accuracy. The implementation of the proposed algorithm is discussed, and several experimental results are provided to prove the efficacy of the algorithm in reducing measurement uncertainty.

[Chapter 5](#) introduces the main features of the CSS physical layer (PHY) described in the amendment IEEE 802.15.a-2007 and discusses the basic CSS signal detection problem in ideal conditions and under the effect of various uncertainty contributions. In particular, an optimal solution for frame timestamping at the symbol level is proposed. Some experimental results based on a software-defined radio (SDR) implementation of the IEEE 802.15.4a PHY show that CSS can be successfully adopted for accurate ranging and, as side effect, also for time synchronization.

Finally, [Chapter 6](#) presents a general discussion of the work described in this thesis reviewing the main contribution of the research. Specific concluding remarks on the research topics treated in the dissertation are also given. In addition, perspectives on possible future developments of the work are provided.

2.1 INTRODUCTION

AS ALREADY mentioned in the Introduction, *positioning*, also called *localization*, can be generally defined as the process of finding location coordinates of people or objects within a reference frame, in a two-dimensional (2D) or three-dimensional (3D) space.

In the last years, the astonishing growth of mobile and portable devices provided with wireless connectivity has paved the way for the development of positioning systems relying on the measurement of different location-related parameters of the wireless signal. For instance, signal strength of an RF link notoriously depends on the range between transmitter and receiver, according to a law whose details depend on the propagation model of the physical environment where communication occurs. Similarly, RF signal propagation time depends on the distance between the communicating devices, and can be determined by knowing the signal propagation speed in the medium. Furthermore, the angle at which RF signal arrives at the receiver yields important information about the position of the transmitter, and can be related to the transmitter-receiver separation as well. Accordingly, distance can be indirectly determined from the measurement of such parameters, and later processed by means of appropriate methods to estimate the position.

Probably, the best known and most widespread example of wireless localization technique is the global positioning system (GPS). However, it is not the ultimate solution for all location-enabled applications. In fact, GPS fulfills the demand for outdoor localization, where the devices can receive the signals coming from satellites, but its performance drastically deteriorates in the presence of obstructions limiting the LOS, e.g., inside of buildings. The fact that indoor environments cannot take advantage of GPS has fostered the research for alternative non-satellite-based positioning solutions.

Within this context, we speak of *wireless indoor positioning* when the location procedure is performed using wireless systems and the reference frame is placed in indoor environment. One more informa-

tion is needed. Broadly speaking, especially in the literature, various positioning systems are referred to as *wireless* in the sense that they require *no electric wiring*. In this work, the term *wireless* refers exclusively to systems based on *RF technologies* that rely on distance estimates to determine the location of an object.

In the remainder of this Chapter, we aim to provide an overview of wireless indoor positioning systems, as a means of establishing a background for the present research. First, we describe the methods used to derive the location of an object through position-related measurements of the wireless link. Then, we focus on the range-based positioning approach and, in particular, on the techniques used to infer distance estimates from RF signal measurements. Finally, we review the relevant literature on the subject.

2.2 POSITIONING TECHNIQUES

Before we delve deep into the depths of wireless indoor positioning techniques, it is useful to introduce a generalized scenario that, regardless of the underlying technology and the final application, may describe the fundamental tasks that a positioning system is expected to perform. Within this generalized scenario, the essential requirement is the communication between a device that need to be localized and a set of reference devices with fixed specific coordinates. According to the context of the scenario being discussed and in agreement with terms commonly used in the literature, along this thesis we interchangeably use the words *target*, *object*, *mobile*, and combinations of thereof to indicate the wireless device whose location coordinates have to be estimated. Similarly, any reference device with known position coordinates used to accomplish the location process is usually referred to as *anchor*, *beacon*, *reference*, or *landmark*. In both cases, above mentioned terms are often followed by the word *node* or *device*.

2.2.1 Lateration

As aforementioned, positioning and ranging are two closely related concepts. Actually, the vast majority of wireless positioning systems rely on the use of multiple target-to-anchor range measurements inferred from distance-related parameters of the RF signal. Later, these distances are suitably managed to obtain location.

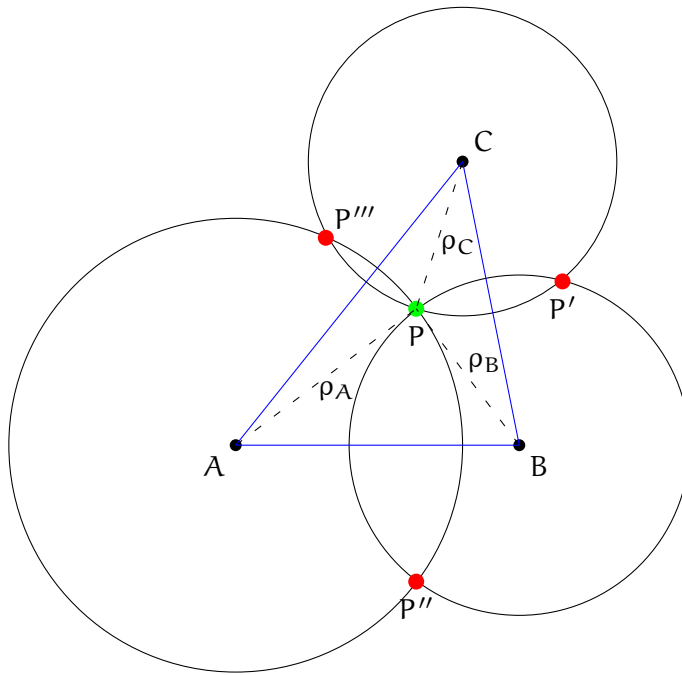


Figure 2.1: Lateralation positioning method.

The most commonly used positioning technique determines target location by finding the intersection of circles with centers corresponding to the anchors coordinates and radii the distances from the target [1]. This range-based method is usually called *multilateration*. In ideal conditions, i.e., in the absence of noise or ranging errors, three intersecting circles, i.e., three anchors, are sufficient to achieve target location without ambiguity in a 2D space. In this case, the process is referred to as *trilateration*, since the anchors layout represents a triangle. Figure 2.1 shows an example. A, B and C denote three anchors whose coordinates in a reference system are known, whereas P denotes a target whose position has to be determined. All the four devices lie in the same plane. The intersection of the circles centered in A, B, and C, with radii ρ_A , ρ_B , and ρ_C , respectively, is marked in green and represents the location of target P. The intersections P' , P'' , and P''' , respectively, are marked in red and point out the ambiguities that would be caused if only two anchors were used.

2.2.2 Angulation

Target position can furthermore be determined by finding the intersection of bearing lines each one passing through the point given by anchor coordinates, and slope the angle off target location. This

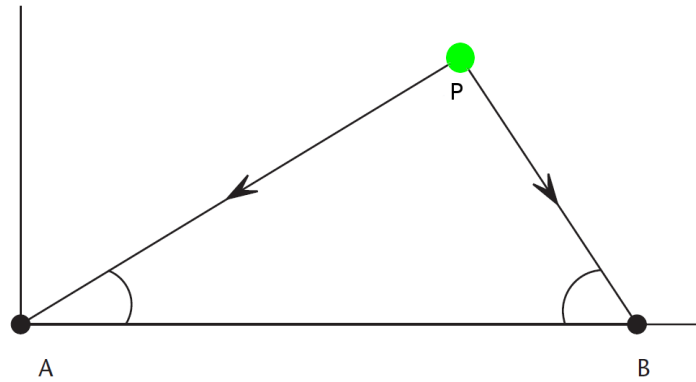


Figure 2.2: Angulation positioning method.

method is traditionally known as *angulation*. In the case of no noise or angle measurement inaccuracies, at least two target-to-anchor bearing lines are required to obtain positioning in a 2D space [1], as shown in Figure 2.2. Let A and B denote two anchors whose coordinates in a reference system are known, and P denote a target whose position has to be determined. The three devices are in the same plane. The intersection of the bearing lines through A and B, with slope α and β , respectively, indicates the location of target P. The coordinates of P can be computed by measuring angles α and β and considering the distance between A and B found from their known coordinates.

2.3 WIRELESS RANGING

Certainly, distance measurement forms the heart of any range-based positioning system. As a consequence, the accuracy of positioning strongly depends on the accuracy of ranging.

In the last years, several approaches relying on different sensing technologies have been proposed for indoor positioning and ranging. Nowadays, the distance between two objects can be accurately measured by using ultrasonics devices [2], infrared sensors [3], laser range finders [4] video cameras [5], or combinations thereof [6, 7]. However, such systems suffer from limitations imposed by LOS constraints, as they usually work properly only in a specified direction. As a consequence, they are effective if the sensor-to-target bearing is known in advance or if sophisticated and time-consuming pointing systems are used. Unfortunately, strongly directional sensors can be hardly used anytime power consumption is a concern and human intervention should be avoided. In fact, achieving both omni-directionality and ac-

curacy in the short range is notoriously quite hard and, consequently, it is still a hot research topic worldwide.

Camera-based solutions are very effective in terms of accuracy, even in the presence of partial occlusions. However, they are not always usable because of privacy issues and because they suffer from scalability problems. To overcome the directional constraint of such systems, pan-tilt and omni-directional cameras have been also proposed [8]. Their main drawback is the high computational burden when multiple targets have to be recognized and tracked.

The most accurate approach is provided by laser-based systems, e.g., based on scanning heads, which also address the target pointing problem [9]. Unfortunately, these systems are much more expensive than the other solutions.

RF-based ranging techniques are inherently less sensitive to obstacles and dissipate less power than optical and ultrasound solutions. In addition, they may exploit the same wireless modules used for communication and they are particularly suitable for wearable indoor applications. As stated before, in wireless distance measurement techniques the range between two objects is obtained indirectly from some distance-related parameters of the RF signal. The two most common approaches are based on RSS and signal ToF measurements. In the following Sections we present the fundamental aspects of RSS and ToF techniques, discussing the different phenomena that limit the accuracy of these measurements.

2.3.1 Received-Signal-Strength Ranging

The RSS-based ranging technique relies on the relationship between the measured received signal power and the transmitter-receiver distance. If the transmitted power and the signal propagation model are known, the distance from the transmitter can be estimated by reversing the equation of the model.

The fundamental propagation model predicting the received signal-strength at a given distance from the transmitter in LOS path conditions is the so-called *free-space* path loss model [10]. It is described by the well-known free-space Friis equation as

$$s = s_t g_t g_r \left(\frac{\lambda}{4\pi d} \right)^2 \quad (2.1)$$

where s is the received signal power, s_t is the transmitted signal power, g_t and g_r are transmitter and receiver antenna gains respectively, d is the distance between transmitter and receiver (expressed in meters) and λ is the wavelength (expressed in meters). Clearly, (2.1) does not hold when d equals to zero. Moreover, the Friis free-space model is valid only for values of d which are in the far-field, or Fraunhofer region, of the transmitting antenna. For this reason, a reference distance denoted as d_0 is introduced in the model as a known received power reference point in free-space. The value of such reference distance must be chosen so that it lies in the far-field region of the transmitting antenna and is smaller than any other distance considered in the wireless link. Then, the received power s at any distance d from the transmitter greater than d_0 can be expressed as

$$s = s_0 \left(\frac{d_0}{d} \right)^2 \quad (2.2)$$

where s_0 is the received power at d_0 , which can be derived from (2.1), or by considering the average received power at several points located at a radial distance d_0 from the transmitter. When the transmitted power s_t or the received power s_0 at the reference point is known, it is easy to obtain the range between transmitter and receiver in free-space LOS conditions by reversing (2.1) or (2.2), respectively.

However, in practical wireless link the propagation path between transmitter and receiver may be non-line-of-sight (NLOS). Moreover, signal propagation can be subjected to the effect of various propagation phenomena such as reflection, diffraction and scattering, which alter the relationship between received power and distance. A number of propagation models which take into account the different factors impacting on signal propagation have been proposed in the literature, both for indoor and outdoor environments. Among these, a model widely adopted in indoor environments is the *log-distance shadowing* path loss model [10]. It can be considered as a generalization of the free-space path loss model and is given by

$$s(t) = s_0 - 10 \log \left(\frac{d}{d_0} \right)^\eta + w \quad (2.3)$$

where $s(t)$ is a random variable describing the received power (expressed in decibels) at time t and distance d from the transmitter, s_0 is the random variable modeling the received power (expressed in decibels) at the reference distance d_0 , η is the path loss coefficient,

i.e., the rate at which the signal power decays with respect to distance, and w is a random variable with zero mean and variance σ_w^2 , which accounts for the random shadowing effects occurring over a large number of measurement positions which have the same distance between transmitter and receiver, but have different levels of clutter on the propagation path. From (2.3) the distance between transmitter and receiver can be readily estimated as follows

$$d_R(t) = d_0 \cdot 10^{\frac{s_0 - s(t)}{10 \cdot \eta}} \quad (2.4)$$

Usually the RSS can be measured easily and without additional circuitry, because most of integrated wireless chips are natively equipped with a received-signal-strength indicator (RSSI). In recent years, the RSS-based ranging has been widely analyzed both theoretically and experimentally. An exhaustive empirical analysis of this method is available in [11, 12]. The main drawback of RSS-based distance measurements is its considerable sensitivity to multipath and shadowing phenomena, which are particularly critical indoor for IEEE 802.15.4 networks [13, 14]. Some researchers state that the performance of RSS-based approaches cannot be significantly improved by means of signal processing techniques, since it is limited by the intrinsic variability of the RSS in the chosen environment [15]. However, other authors believe that the total uncertainty can be mitigated through subsequent refinements [16].

2.3.2 Time-of-Flight Ranging

The ToF-based ranging method relies on the measurement of the propagation time of the RF signal. In general, two alternative ToF-based distance measurement techniques exist, i.e., the time-of-arrival (ToA) and the round-trip time (RTT) approach, respectively.

The ToA technique, also known as one-way ranging (OWR), relies on the estimation of the propagation time of a signal traveling between two wireless devices [17]. In particular, the estimated distance results from the product of the signal propagation time and the light speed. However, the OWR technique requires that the transmitter and the receiver are tightly synchronized (i.e. in the order of 1 ns or less for short-range communications), which is particularly challenging [18].

The RTT method instead, sometimes referred to also as two-way ranging (TWR), is based on the measurement of the time interval be-

tween the time instant when a message is sent and the time instant when the corresponding response message is received by the same device [19]. In this case, the ToF value is obtained by dividing the measured RTT by two after removing the time spent by the message on either devices [20, 21]. Since the RTT is measured by the same node, no clock synchronization is required. For this reason, this approach is more frequently used. In principle, using the RTT method the distance between transmitter and receiver can be easily estimated as follows

$$d_{\tau}(t) = \frac{c}{2} \cdot [\tau(t) - o_{\tau}(t)] \quad (2.5)$$

where $\tau(t)$ is a random variable modeling the total RTT, c is the speed of light, and $o_{\tau}(t)$ is the random temporal overhead given by the sum of:

- the latency between the moment when a message is timestamped on the sender side and the moment when the corresponding bit actually leaves the antenna;
- the time spent on the destination node to receive the incoming message and to reply with an acknowledgement (ACK) message;
- the latency between the moment when the first bit of the ACK message reaches the antenna and the moment when the message is timestamped by the receiver.

The simplest and most effective approach to measure the RTT between every device and its nearby partner nodes is to use a start-stop timer or a time-to-digital converter (TDC) with sub-nanosecond resolution. Each timer or TDC is reset and triggered just before a node sends a new message to its partner and it is stopped as soon as the ACK message is received [19]. Accordingly, the ToF and the distance between nodes can be estimated by dividing the measured RTT value by two after the time spent to encode and to decode frames is removed at both ends. Nowadays, the best available solutions based on the RTT method rely on ultra-wide band (UWB) signals [22, 23], as they proved to be less sensitive to multipath propagation. However, they require custom and sometimes power-hungry circuits that can be hardly used on wearable devices. Alternatively, solutions based on CSS signals have been recently proposed, although their performance is not very clear yet [24, 25]. With other widely used wireless

technologies (e.g., based on the standard IEEE 802.15.4), accuracy typically drops due to the large random jitter associated with time interval measurements [26].

2.4 RELATED WORK

A number of indoor positioning systems have been developed in the last years to meet distinctive requirements of various applications and services.

Considering recent advances in this emerging field, performance evaluations of systems created almost ten years ago are hardly valid today to represent a useful state-of-the-art background. Moreover, most updated surveys on indoor positioning systems available in the literature highlight variety in the applications addressed, conceptual heterogeneity, and differences in design and in the adopted technology [27, 28]. Therefore, it is difficult – if not impossible – to accomplish objective performance comparison and benchmarking between several systems. Furthermore, it is beyond the scope of our research to provide a complete overview of positioning systems available till now. Nevertheless, we think it is worthwhile reviewing the most significant work in the field of indoor positioning systems, despite of their age or the outdated technique used, reviewing the key features of each of them.

A number of classification schemes are used in the literature to survey indoor positioning systems. In this dissertation, we classify the systems based on their enabling technology. Table 2.1 summarizes the main features of indoor positioning solutions reviewed in the following Sections.

2.4.1 *Infrared*

Active Badge [29] is one of the early positioning systems designed for people localization inside buildings. The system is based on infrared technology. Each person to be located wears a small, lightweight infrared transmitter badge – the so-called Active Badge – which broadcasts a globally unique identifier by emitting short infrared pulses every 15 s. These pulses are detected by one or more infrared receivers mounted in fixed positions on the ceiling. The position of an Active Badge device is determined using the proximity method, and the information provided is just symbolic, i.e., the room where the badge

Table 2.1: Comparison of various indoor positioning systems.

SYSTEM	TECHNOLOGY	METHODOLOGY	ACCURACY
Active Badge (1992)	Infrared	Proximity	Room level
Active Bat (1997)	Ultrasounds	ToF, lateration	3 cm
SpotON (2000)	RFID	RSS, lateration	3 m
RADAR (2000)	WLAN	RSS, fingerprinting	3 m
Ubisense (2005)	UWB	TDoA, AoA, triangulation	15 cm

is located. Although infrared technology is inexpensive, the system has a number of drawbacks due to the characteristics of infrared signals, i.e., short range (about 4 m), reflections, sensitivity to fluorescent lighting and direct sunlight.

2.4.2 Ultrasound

Active Bat [30] is widely regarded as the pioneering system for indoor people localization based on ultrasound technology. Similarly to the Active Badge system, whose represents an evolution, the Active Bat platform consists of an ultrasonic transmitter worn by each person to be located – the so-called Bat – and several ultrasonic receivers mounted on the ceiling. The transmitter periodically sends a short pulse of ultrasounds that are received by a network of receivers mounted on the ceiling in fixed known positions. The location of the user carrying the Bat is determined through lateration by means of ToF-based distance measurements. In addition, the system implements a statistical rejection algorithm in order to eliminate large ranging errors due to reflections of the ultrasonic signals. An experimental test bed consisting of 720 receivers deployed over a 1000 m² ceiling and 75 transceivers provided a localization accuracy of 3 cm for 95% of the measurements. However, the large number of receivers needed to achieve high accuracy is very demanding both in terms of cost and deployment time, thus limiting the scalability of the system.

2.4.3 Radio-frequency

SpotON [31] is an indoor localization system based on radio-frequency identification (RFID) technology. Each target to be located is provided with an RFID tag. Position estimate is obtained by applying

the lateration method on inter-tag distances derived from RSS measurements of the signal. The system has significant limitations due to the poor location accuracy, of about 3 m, and the long time required to accomplish the positioning process, i.e., between 10 and 20 s.

RADAR [32] provides one of the first experimental works on indoor positioning based on IEEE 802.11 wireless local area network (WLAN) technology. The system adopts the RSS mapping technique, i.e., a database of RSS-location pairs collected within the reference frame. Then, given an RSS measurement, the target is assigned the location associated with the nearest RSS value stored in the database in terms of some defined metrics. The average location error reported by RADAR is approximately 3 m.

Ubisense [33] is a commercial indoor positioning system relying on UWB technology in the 6.5–8 GHz band. The system is made up of active tags, that have to be located, and a set of receivers deployed in known fixed positions. Position determination is carried out by triangulation using a combination of time-difference-of-arrival (TDoA) and angle-of-arrival (AoA) measurements of the UWB pulses transmitted by the active tags. The specified accuracy of Ubisense system is 15 cm.

RSS-BASED RANGING AND POSITIONING IN INDOOR ENVIRONMENT

3.1 INTRODUCTION

AS INTRODUCED in [Chapter 2](#), a number approaches for wireless indoor localization rely on RSS measurements collected in a WSN. In fact, RSS can be used to estimate the range between a target node and a number of anchor nodes with known coordinates. The location of the target node is then determined by multilateration [27]. RSS-based technique is an appealing approach [34], mainly due to the fact that RSS measurements can be obtained with minimal effort and do not require extra circuitry, with remarkable savings in cost and energy consumption of a sensor node. In fact, most of WSN transceiver chips have a built-in RSSI, which provides RSS measurement without any extra cost. Moreover, wireless nodes present some advantages in terms of system miniaturization, scalability, quick and easy network development, and reduced energy consumption.

In the literature there exist many works about RSS-based outdoor localization, most of which analyze the problem through simulations and experimental data [35, 36]. Some of these studies showed the large variability of the RSS, due to the degrading effects of reflections, shadowing and fading of the radio waves [13, 14, 15, 37]. This results in significant estimated distance errors and, finally, in lack of accuracy of positioning.

Conversely, to the best of our knowledge, less attention has been given to RSS-based indoor localization. Actually, the available results are obtained mainly by means of simulations. Furthermore, the models adopted in these simulations use either the same or different path loss coefficients for each link, but they usually do not account for the different nonidealities of RF signal propagation in indoor envi-

Parts of this Chapter were published in:

P. Pivato, L. Palopoli, and D. Petri, "Accuracy of RSS-Based Centroid Localization Algorithms in an Indoor Environment," *IEEE Transactions on Instrumentation and Measurement*, vol. 60, no. 10, pp. 3451–3460, Oct. 2011.

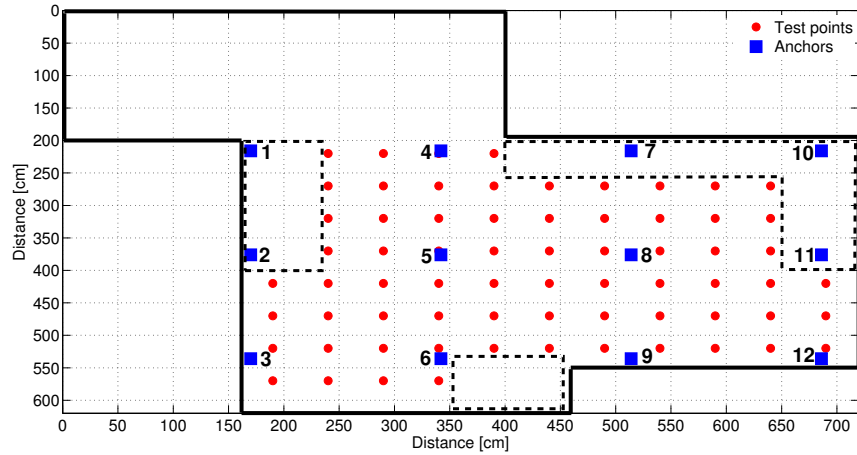


Figure 3.1: Location test points within the *Domotic Application Lab*.

ronments [38]. As a matter of fact, there is a lack of experimental data, which are necessary to adequately validate the proposed solutions [32]. For this reason, it is meaningful to investigate the accuracy of RSS-based indoor ranging and positioning. Therefore, in this Chapter we aim to present:

- a deep analysis of the impact of different disturbing phenomena such as reflections, diffraction and scattering on the accuracy of the RSS measurement;
- an exhaustive study of the influence of the error introduced by low-computational-complexity localization algorithms recently proposed in the literature.

At first, we consider a log-distance path loss model, which is widely used for the analysis of indoor wireless channels, and characterize it with respect to a specific measurement context. In this case our goal is the identification of the channel parameters by applying linear regression to a significant set of RSS measurements. Afterwards, in addition to the characterization of the adopted channel propagation model, we carry on analyzing the accuracy of the so-called weighted centroid localization (WCL) and relative-span exponential weighted localization (REWL) algorithms. The proposed metrological characterization of the RSS-based indoor localization system allows us to provide an insightful interpretation of the limits of this approach. Finally, this improved knowledge will address the course of our research on indoor wireless ranging and positioning techniques, which will be presented in the following Chapters.

The remainder of this Chapter is organized as follows. [Section 3.2](#) describes the experimental framework and details the measurement

scenario. The characterization of the indoor propagation channel is discussed in [Section 3.3](#), dealing with the adopted channel model and the related channel parameters estimation. In [Section 3.4](#), after a brief overview on the centroid localization (CL) approach, the algorithms used in our experiments are analyzed by means of meaningful simulation and experimental results. Finally, we draw the conclusions in [Section 3.5](#).

3.2 MEASUREMENT CONTEXT

In order to characterize the indoor propagation channel and investigate the accuracy of the WCL and REWL algorithms, we perform several experimental activities. The experiments were conducted in the *Domotic Application Lab*, Department of Information Engineering and Computer Science, University of Trento. This laboratory consists of a room of size 5.8 m \times 4 m, furnished like a real living room (e.g., with a sofa, a table, some chairs, a TV set, and a small kitchen). Therefore, the proposed testbed well reproduces a real-world domestic indoor environment.

The system infrastructure was composed of:

- 1 *mobile target* (MT) node;
- 1 *base station* (BS) node;
- 12 *fixed anchor* (FA) nodes.

The wireless sensing platform used for all experimental activities was a commercial Crossbow TelosB [39]. TelosB node is based on a Texas Instruments MSP430F1611 microprocessor, and equipped with a Chipcon CC2420 wireless module compliant with the standard IEEE 802.15.4. The module is able to transmit up to 128 bytes per packet at a nominal peak rate of 250 kbit/s. We used this type of platform because of its remarkably popularity in the academic community and the wealth of open-source software available.

The MT was set on top of a 50 cm dielectric pole that was placed in different test point during the experiment. The linoleum floor was divided into 68 test point located on a grid with a resolution of 50 cm. They are represented with circles in [Figure 3.1](#) on the facing page. The 12 FAs were hanged on the ceiling, 260 cm high. They are represented with squares in [Figure 3.1](#) and are labeled with a number. The displacement of the FAs formed a rectangular grid covering all the

monitored environment. In order to verify the existence of an optimal coverage pattern assuring the communications in LOS conditions between all the nodes, a preliminary evaluation of various placements of the nodes on the roof and on the ceiling was made. As a matter of fact, we verified that the radio link was good in any configurations. Moreover, we tested different relative antenna orientation between each MT and FA pair, without noticing remarkable differences in the RSS values measured. Then, we arranged the MT and the FAs so that their antennas were as parallel as possible in order to optimize the quality of the radio link.

The system performed the RSS measurements from the messages exchanged between the MT and each FA. The MT sent a ping to each of the 12 FAs requesting a reply. Then each FA replied in turn with a message containing the node identification data (ID) and the transmitted power level. When the MT received a reply message, it measured the signal strength through the built-in RSSI and read the other information contained in the message. The procedure was repeated several times. All the measured RSS values were sent to the BS linked to a laptop personal computer, which stored the data. Finally, the collected RSS values were processed and analyzed in order to extract statistical information, to characterize the indoor propagation channel as reported in [Section 3.3.2](#) and to evaluate the performance of the localization algorithms described in [Section 3.4](#). It is worth noticing that to minimize the exchange of messages and the energy consumption, data collection and processing should be performed on the MT node. We made a different choice because using a personal computer allows for an exhaustive statistical analysis and an easier implementation of different localization algorithms. The measuring procedure was repeated 30 times for each of the 68 test point locations, resulting in a total amount of 24 480 RSS values collected. The achieved measurement repeatability was quite high, i.e., always within ± 1 dBm.

3.3 RF CHANNEL CHARACTERIZATION

3.3.1 *Indoor RF Channel Propagation Model*

In order to characterize the indoor propagation channel we assume that the signal strength follows the log-distance shadowing path loss model previously discussed in [Chapter 2, Section 2.3.1](#) on [page 10](#),

and expressed in (2.3) [10]. An alternative formulation for (2.3) is as follows

$$\mathbf{s} = s_t + K - 10 \log \left(\frac{d}{d_0} \right)^\eta + \mathbf{w} \quad (3.1)$$

where s_t is the transmitted signal power (expressed in decibel-milliwatts), and K is the attenuation factor at the reference distance d_0 . Let d denote the true distance between the MT and a FA, and let \mathbf{d}_R express the distance estimated by inverting (2.4) and using the measured value for \mathbf{s} , i.e., the RSS values. Under the assumptions made in (2.3) and applying the law of propagation of uncertainty [40] to (3.1), we obtain that the distance estimator is biased, and its relative bias is given by

$$\frac{b[\mathbf{d}_R]}{d} \simeq 0.03 \frac{\sigma_w^2}{\eta^2} \quad (3.2)$$

whereas the relative standard deviation results as

$$\frac{\sigma[\mathbf{d}_R]}{d} \simeq 0.23 \frac{\sigma_w}{\eta}. \quad (3.3)$$

Both these formulas have been validated by simulations not reported here for the sake of conciseness. In particular, from (3.2) and (3.3), we have the following:

$$\frac{b[\mathbf{d}_R]}{\sigma[\mathbf{d}_R]} \simeq 0.11 \frac{\sigma_w}{\eta} \quad (3.4)$$

Considering η ranging between 1 and 4, as commonly occurred in practice, (3.4) returns values in $(0.03 \sigma_w, 0.11 \sigma_w)$. Therefore, the distance estimator bias could be significant. For instance, for $\eta = 2.3$ and $\sigma_w = 6.1$ dB, as occurred in our experimental results, we have $b[\mathbf{d}_R]/\sigma[\mathbf{d}_R] \simeq 30\%$. Moreover, according to (3.3), the relative standard deviation of the estimated distance increases for about 5% to 20% for each decibel-milliwatt of RSS standard uncertainty. Thus, we can conclude that any distance estimator based on model (2.3) is very sensitive to RSS uncertainty. To the best of our knowledge this interesting result has not been reported in the literature before.

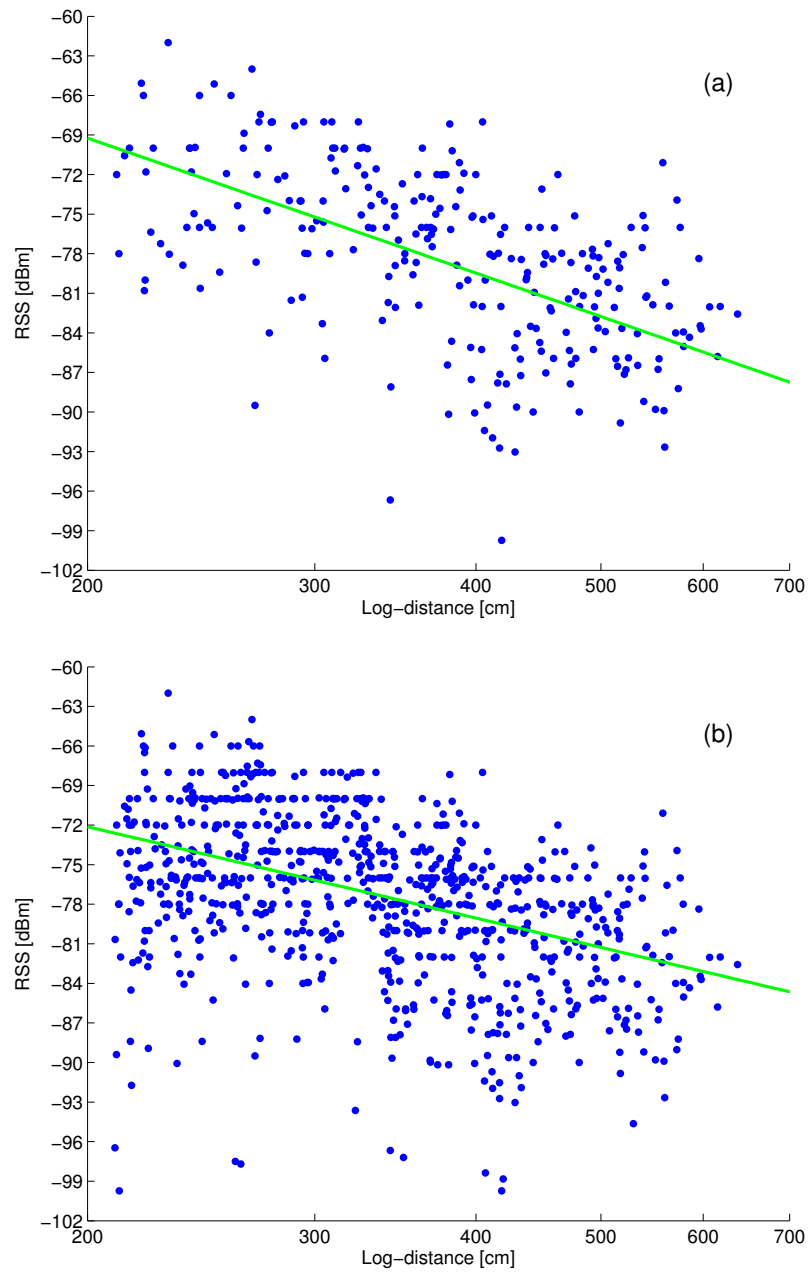


Figure 3.2: RSS measurements and related channel models, considering (a) the 4 FAs in the corners of the room and (b) all the 12 FAs reported in Figure 3.1.

3.3.2 RF Channel Parameters Estimation

The data set of RSS measurements, which was collected as described in Section 3.2, was used to estimate the channel parameters K and η . The transmission power s_t was set to -25 dBm in all nodes. This value was chosen because it was the minimum available power level ensuring a complete coverage of the room, thus allowing a good balance between coverage and energy consumption. The reference distance d_0 , which is related to the antenna far field region, was set to be equal to 10 cm.

At first, we estimated the channel parameters by applying the linear least squares method (LSM) to all the 24480 RSS values collected, obtaining $K = -17.2$ dB and $\eta = 2.3$. The achieved result is shown in Figure 3.2(b) on the preceding page, where the dots represent RSS measurements and the solid line refers to the theoretical path-loss model derived by linear regression. In order to determine if the data well fit the derived parameters, we computed also the regression coefficient ρ , which resulted to be equal to 0.42. Moreover, the standard deviation of the RSS measurements was $\sigma_w = 6.1$ dB, leading to a relative bias on the estimated distance of 17%, and a relative standard deviation of 60%, as given by (3.2) and (3.3), respectively.

Secondly, we analyzed the path-loss model considering each FA node individually, while the MT was still moved in each of the 68 test points. The channel parameters K and η were still estimated by using the LSM for each data set of 2040 collected RSS values.

Then, we considered the four FAs (i.e., FAs 1, 3, 10 and 12) located in the corners of the room and the six-FA configuration given by the four FAs in the corners and the two FAs (i.e., FAs 5 and 8) in the middle of the room. We collected 8160 and 12240 RSS values, respectively, and as described before, we used these values to estimate the channel parameters η and K through the LSM.

Table 3.1 on the following page lists the log-distance channel parameters estimated in each case, together with the error standard deviation and the related regression coefficient. As shown, the channel-model-error standard deviation is nearly constant for all the considered sets of FAs, whereas the resulting path-loss exponents is quite changing. In particular, considering the channels related to each single FA, it ranges from a minimum of 0.5 for FA 4 to a maximum of 4.1 for FA 12. The corresponding regression coefficients behave in a similar way, ranging from 0.15 to 0.63 respectively. From a distance

Table 3.1: Log Normal Channel Parameters.

FA #	η	K [dB]	σ_w [dB]	ρ
1–12	2.3	−17.2	6.1	0.42
1	3.1	−6.8	5.1	0.58
2	2.2	−19.0	4.4	0.48
3	3.3	−0.4	6.4	0.53
4	0.5	−46.2	5.9	0.15
5	3.6	0.2	6.1	0.44
6	2.4	−17.0	6.8	0.35
7	1.1	−36.7	5.7	0.17
8	1.9	−25.1	7.5	0.24
9	2.9	−8.4	7.5	0.42
10	2.8	−9.3	5.9	0.50
11	2.0	−22.7	5.3	0.45
12	4.1	11.7	6.1	0.63
1, 3, 10, 12	3.4	0	6.0	0.56
1, 3, 5, 8, 10, 12	2.7	−11.3	6.4	0.48

estimation point of view, these FAs represent the worst and the best case, respectively. Indeed, a higher value of the regression coefficient means that the data received by the related FA carry more information about the unknown distance. It is worth noticing that the four FAs located in the corners of the room provided the highest value of the regression coefficient; thus, they can be considered as the more informative ones. To the best of our knowledge, no previous work has reported remarkable differences of the channel parameters when considering each FA node singularly. However, given the different positions of the FAs, the received signal is expected to be not affected by the same reflections, fading and multipath interference, thus leading to a significant difference in the channel models. It is worth noticing that similar observations on the irregularity of the wireless communication channel were presented in [41], in which an extension to the isotropic radio model for outdoor environment was proposed.

The histograms h_w of the RSS error w are depicted in Figure 3.3 on the next page, for the case of the 4 and 12 FAs, respectively. Both distributions show a behavior far from Gaussian, which is conversely to the assumption commonly made in the literature [10].

Moreover, we considered the RSS error histograms obtained for different distance intervals of equal amplitude (i.e., 50 and 100 cm). The

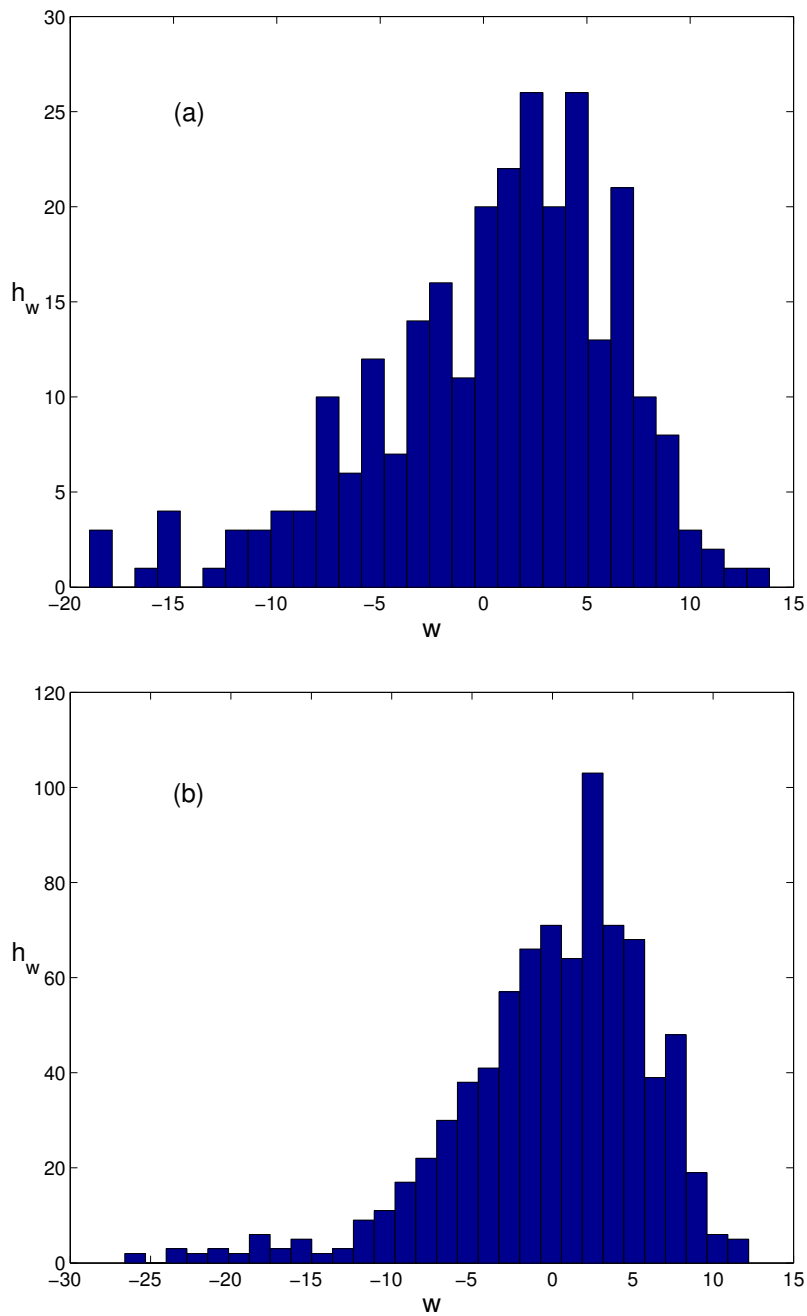


Figure 3.3: RSS error histograms obtained considering (a) the 4 FAs in the corners of the room, and (b) all the 12 FAs reported in Figure 3.1.

obtained histograms noticeably differ each other, suggesting a nonstationary behavior of the RSS error with respect to the distance, which is different from what we would expect from the model suggested in [10].

3.4 LOCALIZATION ALGORITHMS

The localization problem can shortly be formalized as follows. Consider a set of nodes $\mathcal{N} = \{A_1, A_2, \dots, A_n\}$, each one with a fixed and known position. Note that we are working with the common assumption of 2D localization, since the third dimension usually is not of primary interest in indoor environment. Thus, the position of a FA is a two-tuple $a_i = (x_i, y_i)$, where x_i and y_i are evaluated with respect to origin O of the reference system. Let p denote the position of a MT node of unknown coordinates (x, y) , and let RSS_i denote the measured intensity of the signal strength from FA a_i experienced by the MT. The goal of a RSS-based localization algorithm is to provide estimate $\hat{p} = (\hat{x}, \hat{y})$ of position p given the vector $[RSS_1, RSS_2, \dots, RSS_n]$.

RSS-based positioning algorithms can be categorized into two classes [27, 42]:

- the *range-based* algorithm, which use several target-to-anchor distance estimations obtained through the RSS measurements to determine the position of the MT node;
- the *range-free* algorithm, which determines the position of the MT node without performing distance estimation.

In the following, we analyze two different approaches, the WCL and the REWL, respectively. The former belongs to the class of range-based solutions, whereas the latter is a range-free method. Both algorithms are characterized by a low computational effort. This, combined with low transmission power, allows to significantly limit node energy consumption.

3.4.1 Weighted Centroid Localization

The WCL algorithm is based on the so-called CL proposed in [43]. This solution approximates location p of the MT node by calculating the centroid of the coordinates $a_i = (x_i, y_i)$ of the so-called visible anchors, i.e., the FA nodes for which a communication has been es-

established during the measurement. More specifically, the estimated position of the MT node is given by:

$$\hat{p} = \frac{1}{m} \cdot \sum_{i=1}^m \alpha_i \quad (3.5)$$

where m is the cardinality of the subset $\bar{\mathcal{N}}$ of visible FAs. It is worth noticing that when the MT node communicates with all the FAs, i.e., all FAs are visible, the centroid results the center of the FAs coordinates. Notice that the CL approach assumes all the visible FAs equally near the MT node. Since this assumption is most likely not satisfied in practice, in [44], the introduction of a function which assigns a greater weight to the FAs closest to the target, was proposed. The result is the WCL algorithm, which estimates the position of the MT node as:

$$\hat{p} = \frac{\sum_{i=1}^n (\hat{d}_i^{-g} \cdot \alpha_i)}{\sum_{i=1}^n (\hat{d}_i^{-g})} \quad (3.6)$$

where \hat{d}_i is the distance between the MT and FA α_i , which is estimated through RSS_i of the visible FAs. Exponent $g > 0$ determines the weight of the contribution of each FA. If $g = 0$, then \hat{p} is simply the sample mean of α_i , and the WCL reduces to the CL approach. Increasing the value of g causes the FAs to reduce the range of their “attraction field” with respect to the MT node, thus increasing the relative weight of the nearest FAs.

The plots in [Figure 3.4](#) on [page 29](#) show the results of simulations running the WCL algorithm with 4, 6 and 12 FAs positioned as described in [Section 3.2](#) and [3.3](#), and considering $g = 1.8$. Each surface represents the algorithm error e_{alg} in terms of the distance between the true position and the position estimated using the WCL algorithm with a grid resolution of 5 cm. The algorithm inputs were the true distances between the MT and the FAs, calculated from their known coordinates. As shown, passing from 4 to 12 FAs, the error globally decreases, whereas it is drastically reduced in the proximity of FA positions. Furthermore, we can observe that using six FAs the error tends to increase with respect to the four-FA configuration. This is likely due to the presence of the two additional FAs placed in the center of the room, which increases the center clustering behavior featured by algorithms based on the CL approach.

Similar error surfaces were obtained assuming that additive white Gaussian noise (AWGN) with different values of standard deviation affects the RSS measurements. We noticed that, on average, the maximum values of the algorithm error are little sensitive to the noise. Otherwise, the noise affects significantly areas with small error values, usually located near the center of the room, therefore increasing the center clustering behavior of the algorithm.

Table 3.2 and 3.3 on page 31 show the mean and root-mean square (RMS) values of the total distance error in the estimated position e_{tot} , which is achieved by running the WCL algorithm on the experimental data, with 4, 6 and 12 anchors, and considering different values of the exponent g within the range (1.0, 1.8). In particular, the algorithm inputs were the distances between the MT and each FA, which are estimated by inverting (3.1) and using the RSS values measured in each of the 68 test points, as described in Section 3.2 and Section 3.3. The same Tables also summarize the mean and the RSS of the algorithm distance error e_{alg} and the experimental noise distance error e_w determined for the same sets of FAs and values of the exponent g . The experimental noise distance error was obtained as the difference between the position estimates determined by running the WCL algorithm using both the true and estimated distances. Notice that this latter error is due to the noise component w in (3.1). In particular, Table 3.2 and 3.3 show that, on the first approximation, mean μ_{alg} and RMS_{alg} of the algorithm error depend little on the FA position (i.e., FA number) and decrease with a raising exponent g . This behavior is partially compensated by the noise error, whose mean μ_w and RMS_w values increase with an increasing value of g and decrease with a raising number of FAs. As a result, the effect of the algorithm error on the total error is negligible for the four FAs, while it counts for 6 and 12 FAs.

Furthermore, considering any two different FA configurations (e.g., 4 and 12 FAs) it is interesting to note that the ratio of the correspondent mean μ_w and RMS RSS_w values of the noise error reported in Table 3.2 and 3.3 tend to be inversely proportional to the square root of the product between the number of FAs n and the regression coefficient ρ given in Table 3.1 on page 24, i.e.,

$$\mu_w \propto \sqrt{\frac{1}{n \cdot \rho}} \quad (3.7)$$

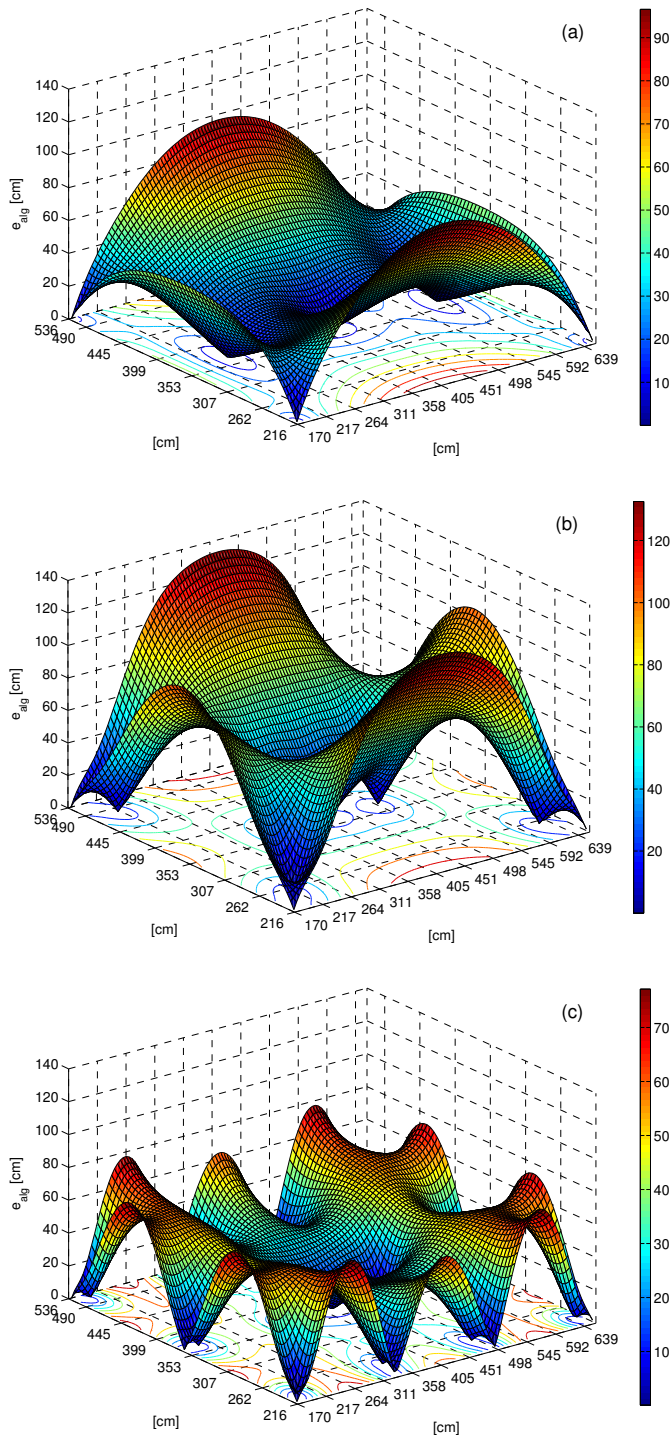


Figure 3.4: WCL distance error for $g = 1.8$ considering (a) the 4 FAs in the corners of the room, (b) 6 FAs, and (c) all the 12 FAs reported in Figure 3.1.

and

$$\text{RMS}_w \propto \sqrt{\frac{1}{n \cdot \rho}} \quad (3.8)$$

Since a growing number of FAs results in a decrease in the regression coefficient, using more FAs reduces the effect of noise by a factor that is smaller than the square root of the number of FAs. In any case, (3.7) and (3.8) can provide some useful hints on the expected effect of noise in different system configurations with changing number of FAs.

Figure 3.5 on page 33 depicts the cumulative histograms H of the WCL estimation errors considering the four FAs in the corners of the room and all the 12 FAs. As expected, the median total estimation error is about 1 m using both 4 or 12 FAs. Indeed the 4 FAs in the corners carry most of the information about the unknown distance, as shown in Section 3.3. Notice also that the use of 12 FAs, although does not produce a significant reduction of the average estimation error, has a beneficial effect on the maximum error.

3.4.2 Relative Span Exponential Weighted Localization

The REWL is an RSS-based range-free localization algorithm recently proposed in the literature [45]. This algorithm is inspired by the WCL method. The weights are obtained by the relative placement of each FA RSS value within the span of all the RSS values measured by the MT node. In the estimation of the MT position, the REWL algorithm favors the FAs which exhibit higher RSS values and therefore are likely to be closer to the MT node. This is obtained using the weighting factor λ , according to the exponentially moving average concept [45]. The estimated MT node position is given by [45]

$$\hat{\mathbf{p}} = \frac{\sum_{i=1}^n [(1-\lambda)^{\text{RSS}_{\max} - \text{RSS}_i} \times \mathbf{a}_i]}{\sum_{i=1}^n (1-\lambda)^{\text{RSS}_{\max} - \text{RSS}_i}} \quad (3.9)$$

where RSS_{\max} is the maximum value in the span of the RSS values measured by the MT node. Suggested values for λ , which are experimentally determined, range from 0.10 to 0.20 [45]. Actually, assuming the path-loss model (3.1), it can be shown that in case of no noise the

Table 3.2: WCL Algorithm Mean Distance Error.

		g				
		1.0	1.2	1.4	1.6	1.8
4 anchors	μ_{tot} [cm]	113	113	116	120	124
	μ_{alg} [cm]	67	52	42	38	40
	μ_w [cm]	78	89	99	107	114
6 anchors	μ_{tot} [cm]	116	112	110	109	110
	μ_{alg} [cm]	94	83	75	69	64
	μ_w [cm]	55	63	71	78	84
12 anchors	μ_{tot} [cm]	123	117	114	111	109
	μ_{alg} [cm]	87	73	60	50	41
	μ_w [cm]	50	59	68	76	83

Table 3.3: WCL Algorithm RMS Distance Error.

		g				
		1.0	1.2	1.4	1.6	1.8
4 anchors	RMS_{tot} [cm]	129	130	134	139	144
	RMS_{alg} [cm]	73	60	51	47	46
	RMS_w [cm]	92	105	117	128	137
6 anchors	RMS_{tot} [cm]	129	126	125	125	126
	RMS_{alg} [cm]	101	90	82	75	71
	RMS_w [cm]	64	74	83	90	97
12 anchors	RMS_{tot} [cm]	134	130	126	124	122
	RMS_{alg} [cm]	95	80	67	55	46
	RMS_w [cm]	57	67	77	85	92

REWL algorithm reduces to (3.6), where g ranges between 0.5 and 3.9 when η and λ assume values in (1, 4) and (0.1, 0.2) intervals, respectively (as given in the Appendix A).

Figure 3.6 on page 35 shows the surfaces representing the algorithm distance error e_{alg} , which is obtained by running simulations of the REWL algorithm for $\lambda = 0.15$, with 4, 6, and 12 FAs and with a grid resolution of 5 cm. The inputs of the algorithm were the theoretical RSS values that might be measured by the MT in each point of the grid in the absence of noise. These values were evaluated using the path-loss model (3.1), considering for each set of anchors the related channel parameters η and K reported in Table 3.1 on page 24 and the true distances d between the MT and the FAs, which are calculated from their known coordinates. The transmission power was assumed to be $P_{tx} = -25$ dB, and the reference distance was $d_0 = 10$ cm. Clearly, the error tends to decrease with the increasing number of FAs. The shape of the error surfaces is substantially similar to the one of the WCL algorithm, with the exception of the four-FA configuration that features an higher error around the center of the grid. As previously highlighted for the WCL, the six-FA configuration exhibits higher algorithm error values with respect to the four-FA configuration. Moreover, we analyzed also the error surfaces obtained by assuming the RSS values affected by AWGN. Assessment on these is similar to the ones drawn for the WCL algorithm.

Table 3.4 and 3.5 on page 34 report the mean and RMS values of the total distance error in the estimated position e_{tot} , which is achieved by running the REWL algorithm with 4, 6, and 12 FAs and considering $\lambda = 0.10$, $\lambda = 0.15$, and $\lambda = 0.20$. The algorithm inputs were the RSS values measured by the MT node in each of the 68 test point, as described in Section 3.2 and 3.3. The same Tables show also the mean and RMS values of the algorithm distance error e_{alg} and the experimental noise distance error e_w . This latter error is determined as the difference between the position estimates achieved by running the REWL algorithm on both the theoretical and measured RSS values. As shown, mean μ_{alg} and RMS_{alg} of the algorithm error depend on the number of FAs, but they feature a different behavior as the weighting factor λ changes. In fact, with four FAs they increase passing from $\lambda = 0.10$ to $\lambda = 0.20$, whereas with 6 and 12 FAs, they decrease significantly when λ increases. Mean μ_w and RMS_w of the noise error decrease with an increasing number of FAs, whereas they decrease with a raising value of λ . As regard to mean μ_{tot} and RMS_{tot} of the

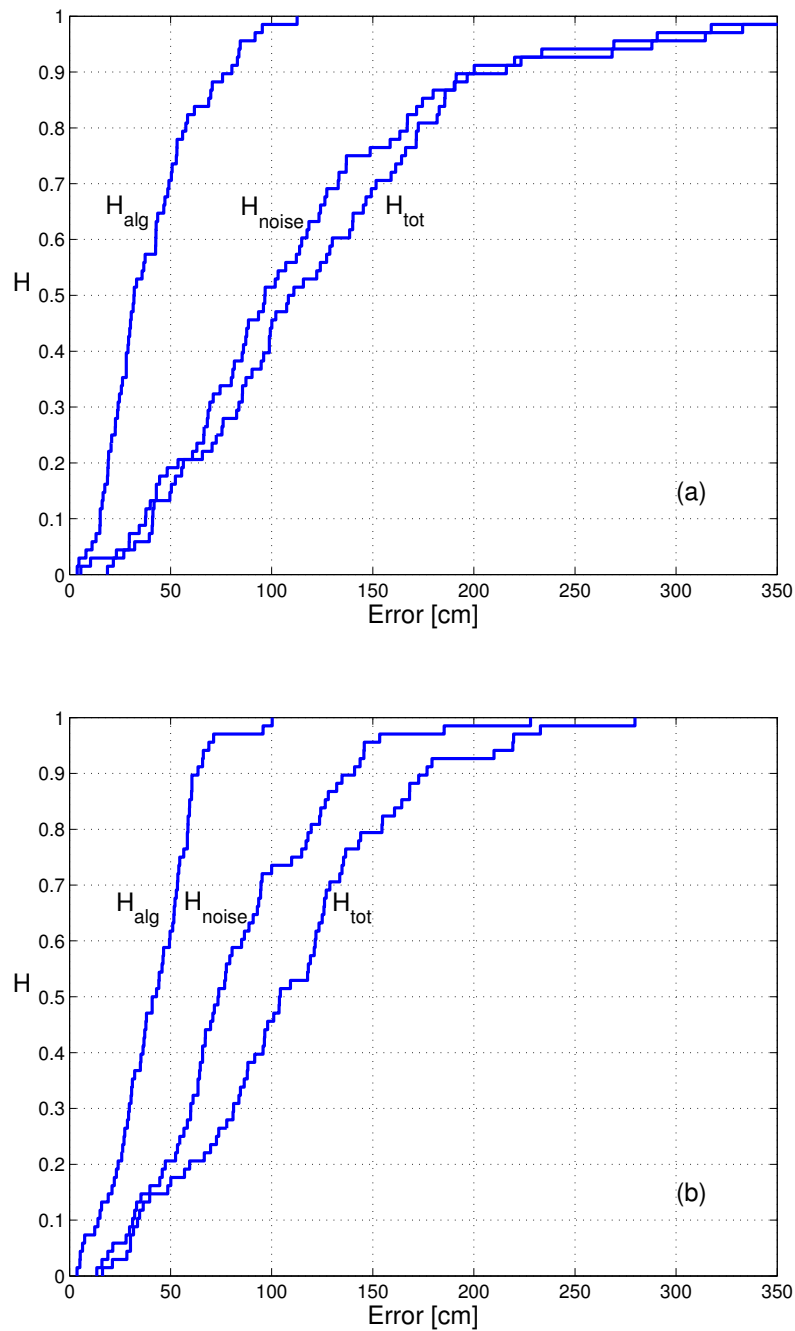


Figure 3.5: Cumulative histograms for the WCL localization algorithm errors considering (a) the 4 FAs in the corners of the room, and (b) all the 12 FAs reported in Figure 3.1.

Table 3.4: REWL Algorithm Mean Distance Error.

		λ		
		0.10	0.15	0.20
4 anchors	μ_{tot} [cm]	111	114	125
	μ_{alg} [cm]	38	58	77
	μ_w [cm]	95	117	130
4 anchors	μ_{tot} [cm]	116	106	105
	μ_{alg} [cm]	82	62	59
	μ_w [cm]	56	76	91
12 anchors	μ_{tot} [cm]	127	113	105
	μ_{alg} [cm]	83	49	30
	μ_w [cm]	51	75	92

Table 3.5: REWL Algorithm RMS Distance Error.

		λ		
		0.10	0.15	0.20
4 anchors	RMS_{tot} [cm]	127	131	144
	RMS_{alg} [cm]	47	59	82
	RMS_w [cm]	111	138	157
6 anchors	RMS_{tot} [cm]	130	121	120
	RMS_{alg} [cm]	89	69	65
	RMS_w [cm]	69	91	107
12 anchors	RMS_{tot} [cm]	139	126	120
	RMS_{alg} [cm]	91	54	33
	RMS_w [cm]	61	87	104

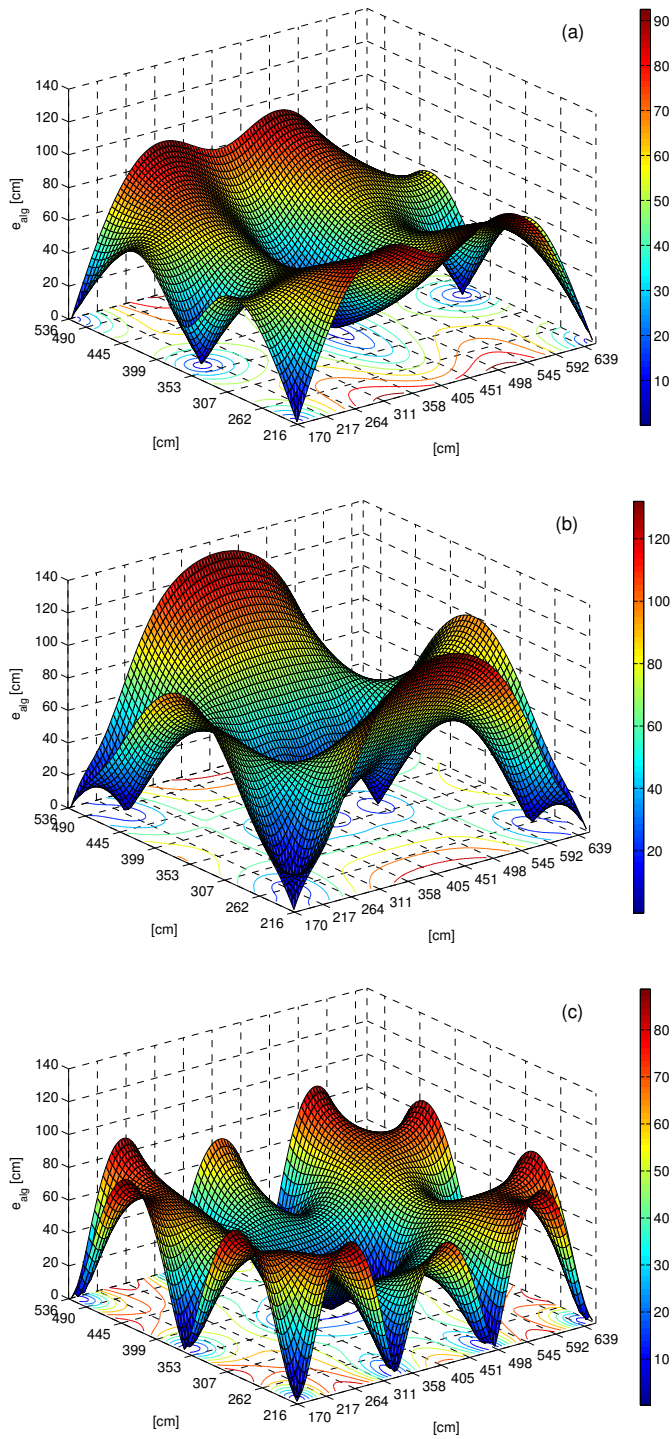


Figure 3.6: REWL distance error for $\lambda = 0.15$ considering (a) the 4 FAs in the corners of the room, (b) 6 FAs, and (c) all the 12 FAs reported in Figure 3.1

total error, they depend little on both the FA position (i.e., FA number) and the weighting factor λ .

Figure 3.7 shows the cumulative histograms H of the localization errors resulting when running the REWL algorithm with $\lambda = 0.15$ and for the four FAs on the corners of the room and for all 12 FA nodes, respectively. Considerations similar to those expressed for the WCL algorithm can be done. In particular, for the 12-FA configuration, the maximum total distance error e_{tot} is limited, while the algorithm distance error e_{alg} is not negligible.

3.5 CONCLUSION

In this Chapter, we have analyzed the performance of indoor ranging and positioning based on RSS measurements collected by a WSN. The accuracy of two classes of low-computational-effort positioning algorithms relying on the centroid concept, which are called WCL and REWL, has been investigated. The measurement system was deployed in a real indoor environment where, by the online running of the studied algorithms, we obtained the estimated position of a MT node in different test points inside an observation field.

At first, we characterized the indoor wireless propagation channel using the log-distance shadowing path loss model, which is largely adopted in the literature. We showed that this model is affected by a quite high relative bias and standard uncertainty. This is most likely due to the severe propagation conditions of the indoor radio channel, i.e., affected by multipath and shadowing phenomena. Therefore, we might expect that the ranging error and, as a consequence, the MT positioning error grows as the distance from the FAs increases.

Secondly, we found that the information carried by each FA strongly depends on the FA position. Hence, for both the considered positioning algorithms, an increasing number of FAs does not necessarily improve measurement accuracy, i.e., conversely to what we would expect.

Furthermore, we studied the uncertainty introduced by the use of approximated localization algorithms, such as WCL and REWL. In particular, we found that the error produced by the algorithm is usually negligible compared to the uncertainty caused by the wireless propagation channel noise; nevertheless the algorithm error may become significant when the number of FAs raises. In spite of that, the measurement uncertainty is primarily determined by the noise asso-

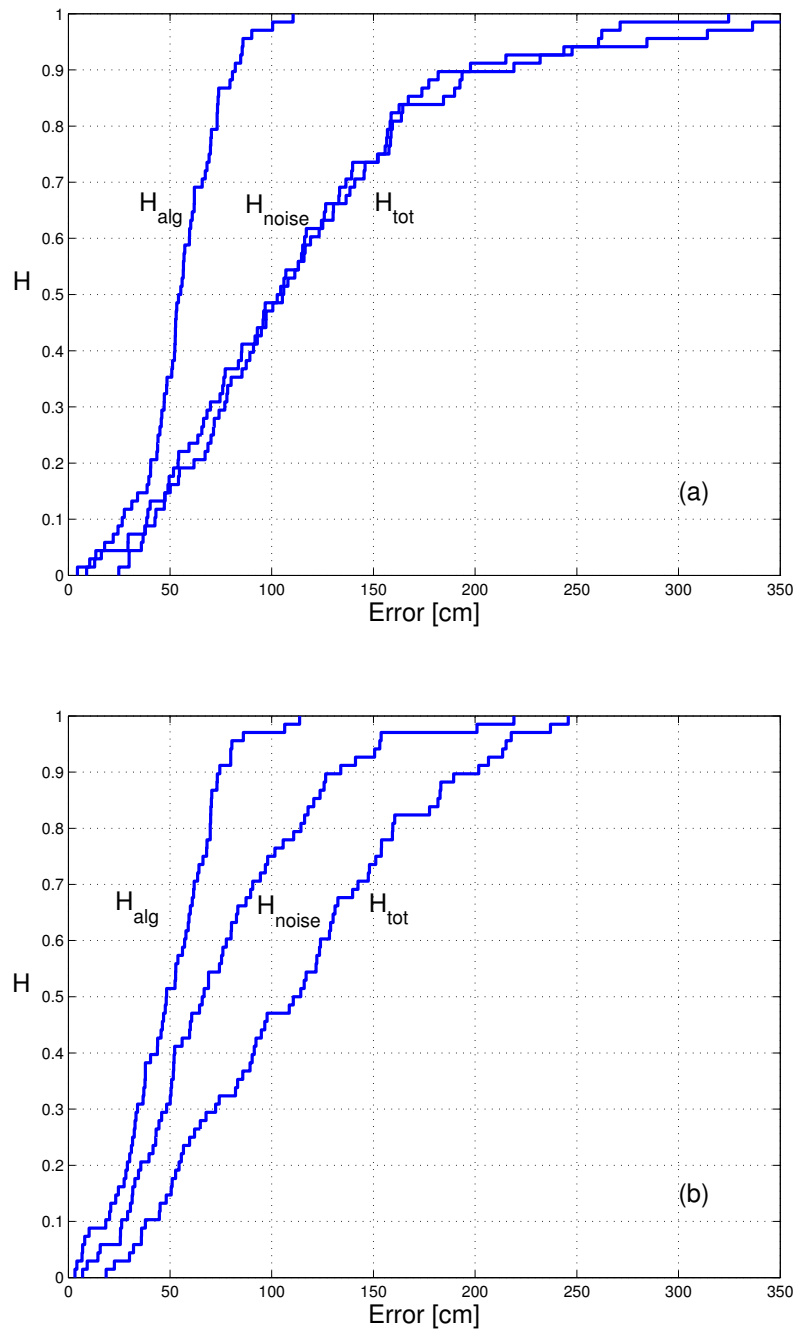


Figure 3.7: Cumulative histograms for the REWL localization algorithm errors for $\lambda = 0.15$ considering (a) the 4 FAs in the corners of the room, and (b) all the 12 FAs reported in Figure 3.1.

ciated to the wireless propagation channel model and, in any case, it results as high as few tens of percent of the size of the considered indoor environment.

To the best of our knowledge, this study first points out the relationship between absolute and relative distance error, highlighting the tendency of the RSS uncertainty to propagate as a relative distance uncertainty. In addition, starting from the experimental data, we suggest that the noise component of the error is inversely proportional to the square root of the product of the FA amount and the regression coefficient of the channel propagation model.

HYBRID RSS-RTT METHOD FOR RANGING PERFORMANCE IMPROVEMENT

4.1 INTRODUCTION

THE STUDY we carried out in [Chapter 3](#) highlighted the considerable sensitivity of the RSS-based ranging and positioning to multipath and shadowing phenomena. In particular, the multipath propagation alters the relationship between RSS values and distance described by the log-distance shadowing path loss model (2.3), and yields to non-monotonic and space-varying measurement results. Apparently, the RSS values exhibit large space-varying fluctuations, but a quite small variance over time when the receiving and the transmitting devices are still and the environment is not perturbed by other moving objects. Despite these limitations, the wide availability of wireless transceiver chips equipped with RSSI makes the RSS-based ranging an easy and cost-effective means to enable object positioning in indoor environment.

On the other hand, as mentioned in [Chapter 2](#), the distance between two wireless devices can be derived from the signal ToF obtained by means of RTT measurement. It is worth reminding that the RTT is measured by the same device, so no common time reference between transmitter and receiver is needed. Therefore, the RTT-based approach eliminates the error due to imperfect time synchronization between the devices. The ranging accuracy in this case depends on a variety of factors, such as the signal modulation type, the properties of the adopted transceiver and the timestamping mechanisms at the transmitting and receiving ends, i.e., the technique used to record the moment when a message is whether sent or received [46].

All things considered, by leveraging the possibility of combining different measurements by means of multisensor data fusion tech-

Parts of this Chapter are going to appear in:

D. Macii, A. Colombo, P. Pivato, and D. Fontanelli, "A Data Fusion Technique for Wireless Ranging Performance Improvement," *IEEE Transactions on Instrumentation and Measurement*, vol. 61, no. 1, pp. 27–37, Jan. 2013.

niques [47, 48], we believe that an hybrid ranging scheme exploiting the complementary behavior of RSS- and RTT-based distance measurements will improve the overall performance of indoor wireless ranging and positioning. Some hybrid solutions to the problem of RF-based distance measurement have been presented in the literature yet. In [49] two hybrid schemes based on the combination of RSS and ToA measurements are discussed, and the Crámer-Rao bound (CRB) on position estimation accuracy is computed. Results show that, for short-range wireless links, the hybrid approach provides improved accuracy with respect to the traditional ToA and RSS methods. In [50] Hatami et al. implements an algorithm of neural networks for an hybrid method that combines RSS and ToA measurements, enhancing the overall performance of the localization scheme. The study described in [51] suggests an hybrid positioning method combining RSS and RTT measurements. However, it is implemented in outdoor environment and employs RTT measurements coming from the cellular network and RTT measured values from the global navigation satellite system (GNSS). The solution from [52] et al. is probably the closest to the solution described in this Chapter. In fact, the authors present a RSS-RTT joint approach for ranging that operates in cluttered indoor environments. However, the proposed implementation relies on an IEEE 802.11 wireless network infrastructure.

In this Chapter, we propose a new data fusion algorithm combining the RSS and the RTT techniques in order to improve ranging accuracy. A preliminary detailed analysis and comparison of the performance limitations of the two considered wireless ranging techniques is given in Section 4.2. The proposed approach, which relies on the improvement of the algorithm reported in [53], is described in Section 4.3 Finally, in Section 4.5 after a exhaustive description of the experimental setup and a preliminary evaluation of the measurement uncertainty associated with either technique in static conditions, several experimental results in two orthogonal dynamic scenarios are reported.

4.2 UNCERTAINTY OF RSS AND RTT RANGING TECHNIQUES

As aforementioned, two different types of wireless RF ranging techniques are commonly used, i.e., those based on RSS measurements and those relying on ToF values. With the RSS-based approach the

distance that separates two wireless devices can be estimated by using (2.4) as follows

$$\mathbf{d}_R(t) = d_0 \cdot 10^{\frac{s_0 - s(t)}{10 \cdot \eta}} \quad (4.1)$$

While apparently simple, the distance measured through (4.1) is affected by multiple uncertainty contributions that may considerably alter measurement results. First of all, in indoor environments, η typically deviates from the ideal value (i.e., 2 assuming the classic free-space attenuation model) as it ranges from ≈ 1.5 in a long corridor to ≈ 3 in furnished rooms [54]. Second, both s_0 and $s(t)$ are affected by multipath propagation and fading. In this respect, several research results confirm that the amplitude of a radio signal at various distances from a transmitter located in the same room exhibits a *Rice* rather than a *Rayleigh* distribution, because the LOS contribution is significantly larger than the signal replicas received after one or multiple reflections [55]. In particular, the so-called K-factor (namely, the ratio between the power of the LOS term and the total power of the other signal replicas) typically ranges from 2 to 5 [56]. In principle, this value should monotonically decrease, but in practice, it exhibits sudden oscillations [57, 58]. In addition, the antenna anisotropy and the limited resolution of the RSS detector integrated in most radio chips make uncertainty estimation even more difficult. If the law of propagation of uncertainty is applied to (4.1) under the assumption that all individual uncertainty terms are perfectly correlated and that the position-dependent systematic offsets are properly estimated and compensated [40], the worst case standard uncertainty is given by

$$\begin{aligned} u(\mathbf{d}_R(t)) = & \frac{d_0 \cdot 10^{\left(\frac{|\hat{s}_0 - \hat{s}(t)|}{10 \cdot \hat{\eta}} - 1\right)}}{\hat{\eta}} \cdot \\ & \cdot \left[u(s_0) + u(s(t)) + \frac{|\hat{s}_0 - \hat{s}(t)|}{\hat{\eta}} u(\eta) \right] \quad (4.2) \end{aligned}$$

where $u(s(t))$, $u(s_0)$ and $u(\eta)$ are the standard uncertainties associated with the individual input quantities, while \hat{s}_0 , $\hat{s}(t)$ and $\hat{\eta}$ are the corresponding values measured at time t . Unfortunately, a trustworthy uncertainty stochastic model for the RSS is hard to find, and it is still an active research topic. Equation (4.2) suggests that the ranging uncertainty can be reduced by calibrating the system in different positions at the same reference distance d_0 from the target in order to make $u(s_0)$ as little as possible. Observe that (4.2) tends to expo-

nentially grow with the difference in RSS. This means that a properly calibrated RSS-based system could be potentially a good *proximity detector* with threshold d_0 . However, it can be hardly used for accurate ranging at arbitrary distances.

The situation is quite different when the distance between two devices is estimated through the RTT by using (2.5) as follows

$$\mathbf{d}_T(t) = \frac{c}{2} \cdot [\tau(t) - \mathbf{o}_\tau(t)] \quad (4.3)$$

Note that (4.3) returns an accurate distance estimate only if:

1. the node distance variation during the whole RTT is negligible;
2. $\mathbf{o}_\tau(t)$ is approximately constant so that it can be properly estimated and compensated.

While the first assumption is reasonably true for people moving indoor (i.e., quite slowly), the second one holds only if the various random latency contributions (particularly those due to the specific channel access mechanism employed) are negligible. Since, in general, this is not true, it is reasonable to assume that, due to the superimposition of multiple independent terms, the random fluctuations associated with $\tau(t)$ and $\mathbf{o}_\tau(t)$ are quite large and normally distributed. In addition, the mean value of $\mathbf{o}_\tau(t)$ is expected to be much larger than the pure propagation time, but it can be estimated from the average of multiple RTT values collected when the destination node is placed at a known reference distance d_0 . Accordingly, the worst case standard uncertainty associated with (4.3) after compensating possible position-dependent systematic offsets is simply given by [40]

$$u(\mathbf{d}_T(t)) = \frac{c}{2} \cdot [u(\tau(t)) + u(\mathbf{o}_\tau(t))] \quad (4.4)$$

where the standard uncertainty terms $u(\tau(t))$ and $u(\mathbf{o}_\tau(t))$ are assumed to be stationary and perfectly correlated, and the wireless traffic is low enough as not to perturb the RTT significantly. In such conditions, (4.4) depends mainly on the message timestamping jitter both at the transmitting and at the receiving end. In particular, if the receiving timestamp is collected as soon as the first symbol or at least the first field of an incoming packet [e.g., the start frame delimiter (SFD)] is correctly detected, the RTT uncertainty is certainly quite smaller than the cumulative jitter associated with the reception of the whole message. In this case, the RTT measurement uncertainty depends on the random time at which the peak generated by the

correlator at the input of the receiver crosses the detection threshold. Such a jitter is a function of the rising time of the correlation peak, and it depends on both the signal-to-noise ratio (SNR) at the receiver input and the chosen modulation scheme. However, if the LOS contribution is much stronger than the various multipath replicas and the distance between nodes is not so large as to make the SNR excessively low for reliable symbol detection, the jitter associated with the LOS correlation peak does not significantly change with distance. Usually, such a jitter is in the order of a few tens of nanoseconds if no special modulation schemes (e.g., CSS) are used [59]. Under such conditions, the relative impact of ToF uncertainty on ranging uncertainty tends to decrease as the distance between the transmitter and the receiver grows. However, it certainly grows back as soon as the SNR drops.

4.3 DATA FUSION ALGORITHM FOR DISTANCE ESTIMATION

From the previous analysis, it follows that the RSS-based ranging approach is preferable around the reference distance d_0 , particularly in the very short range, where it is easier to have a better calibration. Conversely, the RTT-based technique looks more promising over a longer range. Therefore, combining both approaches is a sensible strategy to improve wireless ranging accuracy.

In order to perform object tracking, the distance between two nodes should be continuously measured over time. Assuming that one node is fixed, whereas the other is moving, the distance can be measured by either node (e.g., the moving device) as soon as it receives the response or acknowledgment message sent by its partner. Thus, every distance value estimated through either (4.1) or (4.3) is intrinsically event driven. If the communication between nodes periodically occurs, the time interval T_c between two consecutive messages received by the node measuring the distance can be regarded as the *sampling period* of the ranging system. In theory, T_c can be arbitrarily set by the user. The lower bound to T_c is given by the sum of the minimum RTT value including the time spent to process any sent or received packet and the computing time due to the distance estimation algorithm. Of course, T_c is generally subject to some fluctuations (e.g., due to timestamping jitter, channel access, or processing latency variations). However, if T_c is set much larger than these fluctuations, their effect on the performance of the digital ranging system is negligible, as shown in [Section 4.5.2](#).

As stated in [Section 4.2](#), in principle, the RSS and ToF data are affected by different uncertainty contributions. Therefore, the distance values estimated with (4.1) and (4.3) can be assumed to be just weakly correlated, and they can be merged in a variety of ways, e.g., by simply averaging both estimates or using one of them to measure the relative speed between nodes. In the following, the main steps of a new distance estimation algorithm based on RSS and ToF data fusion are reported. A visual description of this algorithm is offered in [Figure 4.1](#) on the next page. The related symbols are defined in the following subsections.

4.3.1 Data Acquisition and Filtering

An essential preliminary step to improve ranging accuracy is data filtering. The purpose of this operation is not only to reduce the random fluctuations affecting raw measurement results (particularly the ToF values) but also to remove possible values that are not compatible with the movement of a real target (e.g., sudden large distance variations). Data filtering can be implemented in a variety of ways. However, the simultaneous presence of both wideband stationary noise and nonstationary disturbances suggests using an ad hoc solution based on the series connection of a linear filter with a nonlinear heuristic technique. As far as the linear part is concerned, a plain moving-average (MA) filter is used. In fact, not only is the MA filter extremely simple from the computational point of view, but it is also *optimal* in reducing the random wideband noise, since it has the smallest equivalent noise bandwidth (ENBW) among other finite impulse response (FIR) filters of the same order. In addition, it assures the sharpest step response [60, 61]. Moreover, unlike infinite impulse response (IIR) filters, the MA filter exhibits a perfect linear phase response, i.e., with no phase distortion and a constant and predictable group delay. The order M of the MA filters results from the trade-off between four contrasting issues, i.e., output noise variance, filter bandwidth, available memory and delay. The first two quantities decrease with M . However, if the filter bandwidth is too small, possible sharp direction changes of the moving target could be heavily filtered, thus degrading accuracy in dynamic conditions. In addition, the overall estimation delay should be lower than 1 or 2 s, in order not to excessively perturb the system responsiveness perceived by the user. Since the group delay of an MA filter in the analog domain

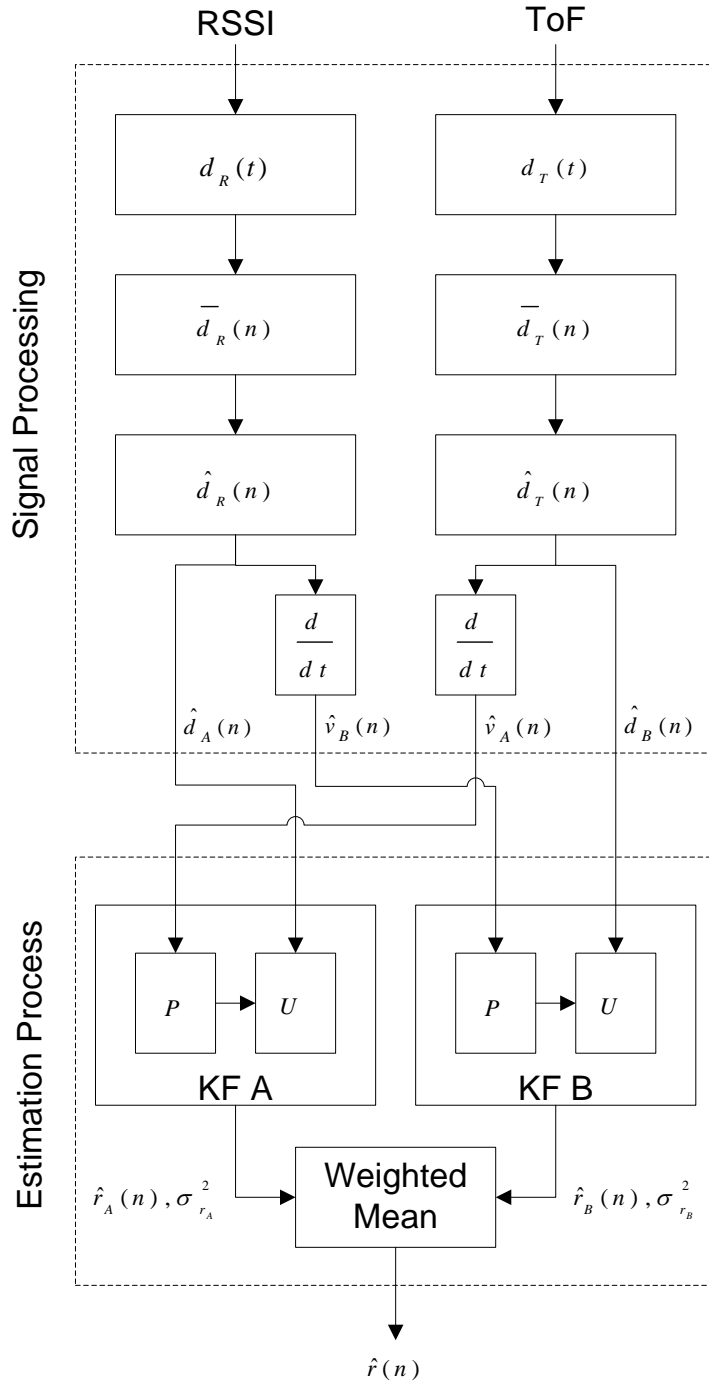


Figure 4.1: Block diagram of the distance estimation algorithm based on RSS and ToF data fusion. The P and U initials in the diagram stand for Prediction step and Update step.

is $(T_c \cdot M)/2$, by reducing T_c for a given value of M , filter responsiveness can be improved at no price in terms of accuracy. Thus, if M consecutive raw RSS and ToF data are filtered by an MA, the distance values resulting from either technique are given respectively by

$$\bar{d}_R(n) = d_0 \cdot 10^{\frac{\hat{s}_0 - \frac{1}{M} \sum_{i=0}^{M-1} \hat{s}(n-i)}{10 \cdot \hat{\eta}}} \quad (4.5)$$

and

$$\bar{d}_T(n) = \frac{c}{2} \left[\frac{1}{M} \sum_{i=0}^{M-1} \hat{\tau}(n-i) - \hat{\delta}_\tau \right] \quad (4.6)$$

where \hat{s}_0 , $\hat{\eta}$ and $\hat{\delta}_\tau$ are assumed to be previously estimated through calibration, while $\hat{s}(n)$ and $\hat{\tau}(n)$ are measured in real-time as soon as the n th ACK message is received. Of course, $\hat{s}(-1) = \dots = \hat{s}(-M+1) = 0$ and $\hat{\tau}(-1) = \dots = \hat{\tau}(-M+1) = 0$ by definition. Note that in (4.5) and (4.6) the MA is computed over raw measurement data *before* applying functions (4.1) and (4.3), as suggested in [40]. This approach is preferable in the case of indirect measurements based on nonlinear functional models, because it reduces the estimation bias caused by the intrinsic variance of the individual input quantities [62].

Unfortunately, as stated above, wideband noise is not the only uncertainty source in the considered measurement problem. Other position-dependent errors may significantly alter measurement results. In order to tackle this additional problem, a heuristic criterion based on human motion-constraints is used. In fact, the human speed in an indoor environment is usually smaller than $v_{\max} = 2 \text{ m/s}$ [63]. Therefore, any value returned by (4.5) and (4.6) can be considered as acceptable only if the variation from the last estimated distance does not exceed $\pm v_{\max} T_c$. In practice, this criterion leads to the definition of the following nonlinear filters:

$$\hat{d}_R(n) = \begin{cases} \hat{d}_R(n-1) + v_{\max} T_c & \bar{d}_R(n) - \hat{d}_R(n-1) \geq v_{\max} T_c \\ \hat{d}_R(n-1) - v_{\max} T_c & \bar{d}_R(n) - \hat{d}_R(n-1) \leq -v_{\max} T_c \\ \bar{d}_R(n) & \text{otherwise} \end{cases} \quad (4.7)$$

and

$$\hat{d}_T(n) = \begin{cases} \hat{d}_T(n-1) + v_{\max} T_c & \bar{d}_T(n) - \hat{d}_T(n-1) \geq v_{\max} T_c \\ \hat{d}_T(n-1) - v_{\max} T_c & \bar{d}_T(n) - \hat{d}_T(n-1) \leq -v_{\max} T_c \\ \bar{d}_T(n) & \text{otherwise} \end{cases} \quad (4.8)$$

Note that the probability of saturation in (4.7) and (4.8) depends not only on the environmental and position-dependent disturbances but also on the order M of the MA filter. Some experimental data showing the effectiveness of the heuristic criterion are reported in [Section 4.5.1](#).

4.3.2 System Model

Let $r(t)$ be the LOS distance between two wireless nodes at time t . The dynamic of $r(t)$ can be described by the following simple linear kinematic model:

$$\begin{cases} \dot{r}(t) = v(t) \\ d(t) = r(t) \end{cases} \quad (4.9)$$

where the input $v(t)$ is the speed component of the moving object in the direction of the fixed node (in the following simply called as *relative radial speed*), and the distance $d(t)$ can be regarded as the output of the system. Given that either node can measure the values of $v(t)$ and $d(t)$ only when an ACK packet is received, system (4.9) can be discretized as follows:

$$\begin{cases} r(n+1) = r(n) + T_c v(n) + T_c \nu(n) \\ d(n) = r(n) + \epsilon(n) \end{cases} \quad (4.10)$$

where $r(n)$ and $v(n)$ are the distance and the radial speed values, respectively, after n message pairs are exchanged between nodes. It is worth emphasizing that the model defined by (4.10) holds both when T_c can be assumed to be constant and when T_c changes as a function of time. Of course, in the latter case, T_c should be also measured at run-time. The two discrete-time random sequences $\nu(\cdot)$ and $\epsilon(\cdot)$ in (4.10) model the effect of speed and distance measurement uncertainty. Both sequences depend on the superimposition of multiple nonstationary uncertainty contributions, e.g., the relative orientation of the antennas and the presence of obstacles or walls. As

a consequence, $\nu(\cdot)$ and $\epsilon(\cdot)$ may exhibit time and/or space fluctuations that survive the preliminary filtering step. In particular, the position-dependent distance offsets randomly change when the target moves, thus becoming either positive or negative. Therefore, in a first approximation, $\nu(\cdot)$ and $\epsilon(\cdot)$ can be assumed to have zero-mean and time-varying variance in the spatio-temporal domain.

4.3.3 Kalman Filter Definition

Since no clear assumptions can be made on the stochastic distribution of $\nu(\cdot)$ and $\epsilon(\cdot)$, finding an optimal dynamic state estimator of (4.10) is very difficult. For this reason, a simple but effective suboptimal approach was used to solve the estimation problem at hand. In fact, it is known that the Kalman filter (KF) is the best linear state estimator when either the process noise or the measurement uncertainty have unknown distributions [64]. A typical KF has a recursive structure that estimates the internal state of a linear dynamic system from a sequence of noisy measurement data. In particular, a KF consists of two main stages connected in a loop, i.e., the *prediction step* and the *update step*. If the superscript $*$ is used to denote the *predicted* quantities, the *prediction* equations of the KF based on (4.10) are [64]

$$\begin{aligned}\hat{\mathbf{r}}^*(n+1) &= \hat{\mathbf{r}}(n) + T_c \hat{\mathbf{v}}(n) \\ \hat{\mathbf{d}}^*(n+1) &= \hat{\mathbf{r}}^*(n+1) \\ \sigma_r^{*2}(n+1) &= \sigma_r^2(n) + T_c^2 \sigma_v^2(n)\end{aligned}\tag{4.11}$$

where $\sigma_r^2(n)$ and $\sigma_v^2(n)$ are the variance values associated with $\hat{\mathbf{r}}(n)$ and $\mathbf{v}(n)$, respectively, as soon as the n th ACK message is received. Since the system (4.10) is monodimensional, the covariance terms in (4.11) are just variances. While $\sigma_r^2(\cdot)$ is updated by the KF itself in the subsequent *update step*, $\sigma_v^2(\cdot)$ is estimated and modified in real-time using the collected input data (e.g., over a window of fixed size) due to the nonstationary behavior of $\mathbf{v}(\cdot)$.

In the *update step* it can be easily shown that [64]:

$$\begin{aligned}\hat{\mathbf{r}}(n+1) &= \hat{\mathbf{r}}^*(n+1) + K(n+1)[\hat{\mathbf{d}}(n+1) - \hat{\mathbf{d}}^*(n+1)] \\ \sigma_r^2(n+1) &= [1 - \sigma_r^{*2}(n+1)]K(n+1)\end{aligned}\tag{4.12}$$

where $K(n+1) = \sigma_r^{*2}(n+1)[\sigma_r^{*2}(n+1) + \sigma_e^2(n+1)]^{-1}$ is the so-called *Kalman gain*, and $\sigma_e^2(n+1)$ is the variance of $\epsilon(n+1)$ when

the $(n + 1)$ th ACK message is received. In practice, $\sigma_\epsilon^2(\cdot)$ can be estimated through a preliminary analysis of the distribution of $\epsilon(\cdot)$ in the considered environment, as described in [Section 4.5.1](#).

4.3.4 Data Fusion

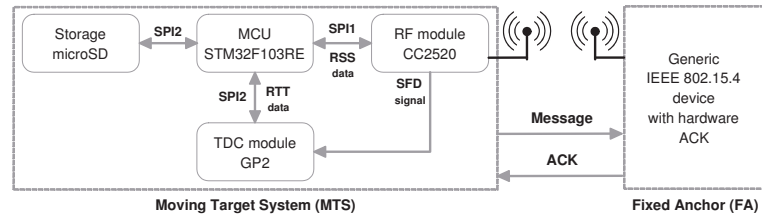
According to (4.11) and (4.12), independent speed and position data are required to implement the KF. In particular, the relative radial speed between two nodes can be estimated as the ratio between the backward Euler difference of two consecutive distance measures and T_c . Given that RSS- and ToF-based distance values estimated with (4.7) and (4.8), respectively, can be assumed to be just weakly correlated, either (4.7) is used to measure $\hat{d}(\cdot)$ and (4.8) is employed to estimate $\hat{v}(\cdot)$ (*Kalman filter A*, or KF A for brevity), or *vice versa* (*Kalman filter B*, or KF B). In the former case, the relative radial speed to be used as input of (4.11) is given by $\hat{v}_A(\cdot) = [\hat{d}_T(n) - \hat{d}_T(n-1)]/T_c$, whereas the sequence of distance measures to be injected into (4.12) is simply $\hat{d}_A(n) = \hat{d}_R(n)$. Dually, in the latter case, radial speed and distance values result from $\hat{d}_B(n) = \hat{d}_T(n)$ and $\hat{v}_B(\cdot) = [\hat{d}_R(n) - \hat{d}_R(n-1)]/T_c$, respectively. In principle, only one of the two KFs should be used. However, both of them are suboptimal since the distribution of the uncertainty contributions is unknown and nonstationary both in time and in space. As a consequence, the most sensible approach is to run both KFs in parallel and then to weigh $\hat{r}_A(n)$ and $\hat{r}_B(n)$ using the reciprocal values of the respective variances. As a result, the measured distance is finally given by

$$\hat{r}(n) = \frac{\sigma_{r_B}^2(n) \hat{r}_A(n) + \sigma_{r_A}^2(n) \hat{r}_B(n)}{\sigma_{r_A}^2(n) + \sigma_{r_B}^2(n)} \quad (4.13)$$

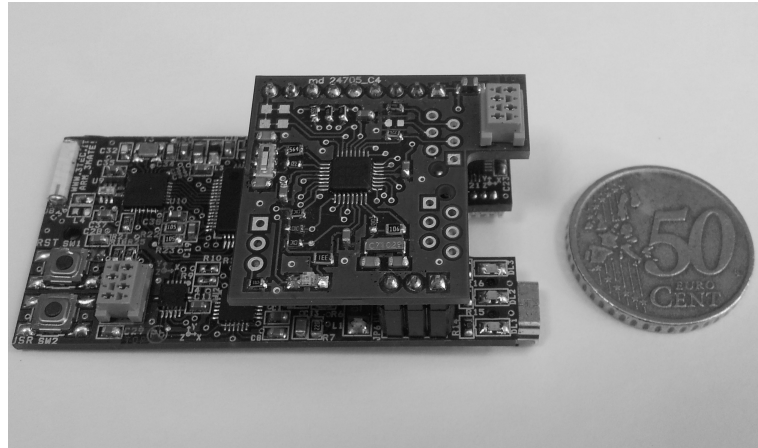
This way, the output depends mainly on the term with the smaller estimated uncertainty.

4.4 HARDWARE PLATFORM DESCRIPTION

In order to evaluate the performance of the data fusion algorithm described in [Section 4.3](#), a new wireless node prototype developed in cooperation with Trettec S.r.L., Trento, Italy, was used for all experimental activities. The block diagram and a snapshot of the node are shown in [Figure 4.2\(a\)](#) and [4.2\(b\)](#), respectively, on the following page.



(a)



(b)

Figure 4.2: Functional block diagram (a) and snapshot (b) of the Mobile Tracking System (MTS) (by courtesy of Trettec S.r.l., Trento).

The system results from the evolution of the node employed for similar experiments in [53], but it is smaller in size and it is equipped with a faster microcontroller unit (MCU) and a larger memory. In particular, the node consists of:

- a TI CC2520 RF transceiver compliant with the standard IEEE 802.15.4;
- a 32-bit STM32F103T8 MCU based on a 72-MHz ARM Cortex M3 architecture with 20 kB of RAM and 64 kB of flash memory;
- a tiny piggyback daughterboard provided with a TDC TDC-GP2 by Acam Mess Electronic with an RMS resolution of 50 ps;
- a 3.7 V 800 mA/h rechargeable lithium-ion polymer battery;
- a chip antenna WE-MCA by Würth Elektronik located in one of the corners of the node prototype along with its own balun;
- a micro secure digital (SD) slot for data logging purposes;
- a universal serial bus (USB) port for node programming and battery charging.

The node, in the following simply referred to as *mobile tracking system* (MTS), is able to measure both RSS and RTT data relative to a chosen fixed anchor (FA), which must be preliminary tuned on the same IEEE 802.15.4 channel used by the mobile tracking system (MTS). The lifetime of the node at room temperature when it is fully active (i.e., uninterruptedly used for high-rate distance measurements) is about 12 hours when the transmission power is set to 0 dBm. The MCU is provided with two serial peripheral interfaces (SPIs): one is used to handle and to exchange information with the transceiver, whereas the other one is linked to the TDC. The TDC is triggered by the rising edge of the SFD flag signal generated by the transceiver when the first bit of the SFD field of an IEEE 802.15.4 message is sent. Similarly, the TDC is stopped by the rising edge of the same flag signal as soon as the SFD field of the corresponding ACK message is received. After the TDC is stopped, the corresponding RTT value is read by the MCU, followed by the RSS value associated with the ACK. Such data are buffered and timestamped by one of the timers of the MTS. If an excessive amount of time elapses between the edges starting and stopping the TDC, the TDC is reset and the corresponding RTT value is discarded. In order to reduce the RTT latency as much as possible, the payload size of each message is set to the minimum specified in the standard IEEE 802.15.4 [65]. In addition, the MTS is configured to operate in a low-level mode, i.e., disabling the carrier sense multiple access with collision avoidance (CSMA-CA) mechanism. As a consequence, the transmission and the channel access times are not affected by the random back-off delays normally introduced by the media access control (MAC) layer. In addition, the FA ACK response latency in a nonbeacon-enabled personal area network (PAN) is deterministic and equal to the radio turnaround time [65]. It is worth highlighting that the FA is not required to be a special device, as instead it was in [53]. On the contrary, any IEEE 802.15.4-compliant node (e.g., a TelosB or a Tmote Sky) can play the role of the FA provided that its transceiver is configured to send ACK messages automatically, i.e., without MCU intervention. The T_c value can be arbitrarily set by the user, but, as stated in Section 4.3, it must be larger than the sum of the worst case RTT, the total computational time of the MCU and the time necessary to save the results into the micro SD memory card. Of course, faster transmission rates improve trajectory tracking and reduce estimation uncertainty for the same reasons described in [53]. By pressing a small button on the MTS, a user moving along a given

trajectory can mark when he/she reaches specified points of interest, thus enabling a fair comparison between the estimated distance and the real one.

4.5 EXPERIMENTAL RESULTS

Different types of experiments were conducted in the *Domotic Application Lab*, Department of Information Engineering and Computer Science, University of Trento. This laboratory consists of a 25 m² room furnished like a real living room (e.g., with a sofa, a table, some chairs, a TV set, and a small kitchen). The proposed testbed (which was purposely established and instrumented to support several projects dealing with domotics) offers the possibility to reproduce a real-world domestic indoor environment, while assuring repeatable conditions. At first, the MTS prototype was calibrated at known, fixed distances. Afterward, the standard uncertainty associated with raw distance measures as well as the average root-mean-square error (RMSE) in different positions of the room with and without using the heuristic filter were evaluated, as described in [Section 4.5.1](#). Finally, the accuracy of the MTS was analyzed in repeatable dynamic conditions, i.e., with the node carried by a user moving along given trajectories. The details of such experiments are described in [Section 4.5.2](#). All data were saved into the onboard SD memory and were eventually processed offline to extract interesting statistics about performance.

4.5.1 *Uncertainty Evaluation of Individual Quantities*

The standard uncertainty associated with individual RSS- and ToF-based measurements was evaluated with a Type A approach [40], namely, with a statistical data analysis.

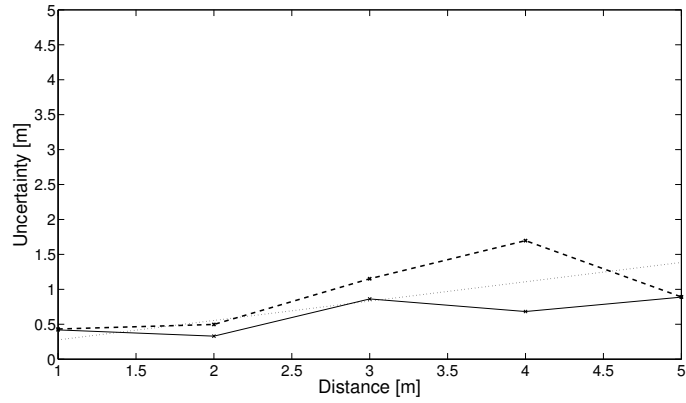
A commercial Crossbow TelosB node configured as a FA was put on top of a 90-cm plastic pole at about 1 m from one of the walls of the room. The MTS prototype was put on another 90-cm pole that was placed in LOS conditions at various distances from the FA. Both nodes were tuned on the same IEEE 802.15.4 channel (i.e., channel 16 centered at 2.43 GHz) with a nominal transmission power equal to 0 dBm and with their antennas as parallel as possible in order to optimize the quality of the radio link. The MTS was calibrated in two steps. In the first one about 5000 RSS and RTT raw values were collected at the reference distance $d_0 = 1$ m in 4 different orthogonal

positions around the FA. The resulting average reference RSS value is $\hat{s}_0 = -55$ dBm with standard uncertainty $u(\hat{s}_0) = 4$ dBm. Similarly, the mean overhead latency estimated from (4.3) after averaging all RTT values collected at $d_0 = 1$ m is $\hat{\delta}_\tau = 433\,065$ ns with negligible standard uncertainty.

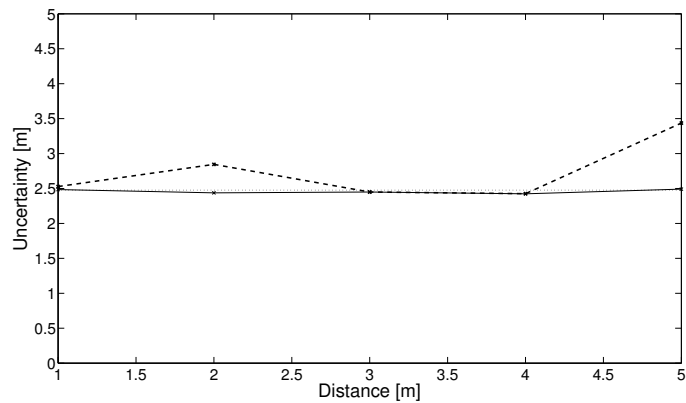
In the second step of the calibration procedure about 5000 RSS and RTT values were collected by the MTS at 2, 3, 4 and 5 m from the FA. The path loss coefficient can be estimated through linear regression, after applying the base-10 logarithm function to both terms of (4.1). From this procedure it follows that $\hat{\eta} = 2.14$ with negligible uncertainty.

In Figure 4.3(a) and 4.3(b) on the next page, the standard uncertainty and the RMSE patterns associated with $d_R(n)$ and $d_T(n)$, respectively, are plotted as a function of the real distance. The solid lines result from a Type A uncertainty evaluation at different known distances from the FA, after removing the static position-dependent offsets. The dotted lines refer to the theoretical worst case standard uncertainty values given by (4.2) and (4.4), respectively. Clearly, the theoretical and experimental uncertainty patterns are in good agreement. In particular, the uncertainty associated with the RSS data tends to grow with distance, whereas the uncertainty related to ToF-based estimates is approximately constant, as expected. The dashed lines in Figure 4.3(a) and 4.3(b) represent the experimental RMSE patterns including the effect of both random fluctuations and position-dependent offsets. When the MTS is steadily located in the same place the position-dependent offsets associated with each method are approximately systematic and they can not be removed by the preliminary filtering. Observe that the position-dependent offsets can significantly affect the RMSE, but their influence on RSS- and ToF-based measurement results can be different even when they refer to the same position. This justifies the use of an estimator based on the combination of dual techniques, such as the one proposed in this paper.

Figure 4.4 on page 55 shows the probability that the saturation due to the heuristic criteria in (4.7) and (4.8) are actually activated when either the RSS values (dotted line) or the ToF values (solid line) are used for distance estimation. Both probability curves are computed as a function of the MA window size M over about 50 000 values collected at various known distances. The probability patterns show that the heuristic has a relevant impact when M is small and it becomes less and less significant as M grows. This is quite obvious because



(a)



(b)

Figure 4.3: Standard uncertainty and RMSE values associated with individual RSS-based (a) and ToF-based (b) distance measurements. The solid lines result from a Type A uncertainty evaluation. The dotted lines in (a) and (b) refer to the worst-case theoretical standard uncertainty values given by (4.2) and (4.4), respectively. Finally, the dashed lines represent the experimental RMSE values including the effect of both random fluctuations and position-dependent offsets.

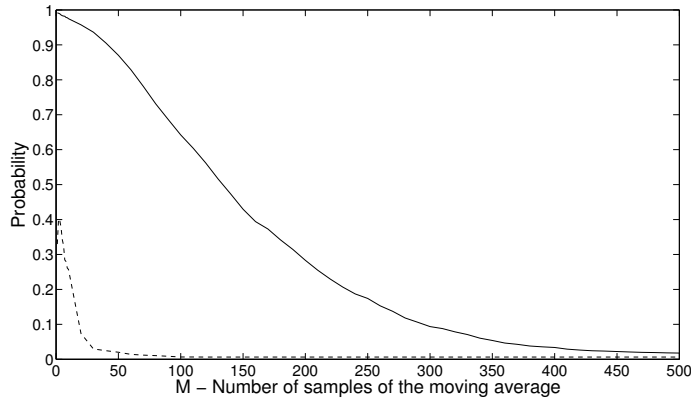


Figure 4.4: Average probability of using the heuristic criterion as a function of the MA window size, when either the RSS values (dotted line) or the ToF values (solid line) are used for distance estimation.

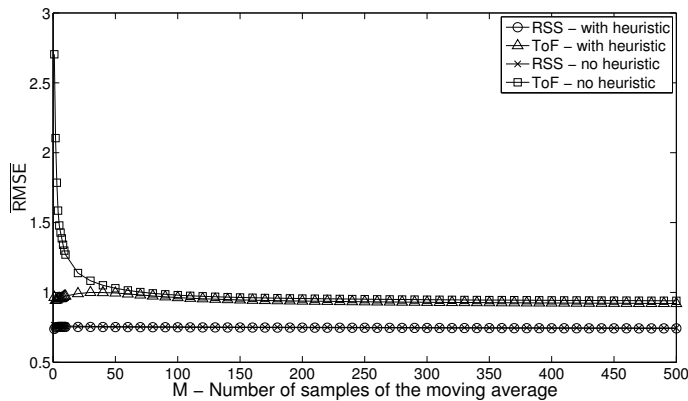


Figure 4.5: Average RMSE patterns related to different RSS-based and ToF-based distance estimators (i.e., MA filters only and MA filters enhanced with the heuristic).

with an MA computed over an increasingly large number of samples, all distance variations are heavily filtered. However, this also negatively affects the tracking capability of the MTS. Note that the heuristic is particularly useful in the case of ToF-based measurements. This is due to the fact that when M is small, the wideband noise affecting raw RTT values is so large as to trigger the heuristic with a very high probability.

Figure 4.5 shows the average RMSE related to the same set of experiments as in Figure 4.4. Different markers refer to RSS- and ToF-based distance estimators both with and without using the heuristic, i.e., based on (4.5), (4.6), (4.7) and (4.8), respectively. The benefits of the heuristic are evident for ToF-based distance measurements. In this case the RMSE obtained with (4.8) is always smaller than the value

resulting from (4.6). In additions, it converges to the asymptotic value with a smaller number of samples M . In this case, the residual error is clearly dominated by the average position-dependent offset. Observe that for $M \geq 100$, accuracy improvements are negligible. Therefore, it is pointless to compute an MA over a larger number of samples.

In the case of RSS-based distance measurements, the benefits of the heuristic criteria are typically minor. Nonetheless, in dynamic conditions the heuristic can be very useful to remove sporadic large distance variations (i.e., outliers) due to abnormal RSS changes occurring in the considered environment.

4.5.2 Accuracy Analysis in Dynamic Conditions

The uncertainty analysis described in the previous Section is essential for three main purposes:

1. To estimate the calibration parameters $\hat{\delta}_0$, $\hat{\eta}$ and $\hat{\delta}_\tau$;
2. To define the size of the MA filter M ;
3. To initialize both KFs.

As stated in Section 4.5.1, the value of M should be set equal to 100. Since the MTS prototype is much faster than the platform described in [53], the minimum nominal value of T_c assuring both reliable radio communication and real-time data acquisition and processing is equal to 10 ms. Consequently, the group delay of the preliminary MA filter is just 0.5 s, i.e., low enough not to disturb the responsiveness perceived by the user. The random fluctuations affecting T_c are particularly small in the considered scenario. This is clearly visible in the histogram shown in Figure 4.6 on the next page, which reports the relative frequency of occurrence of the measured sampling periods out of several tens of thousands samples. Observe that more than 90% of values lie in the range 10 ± 0.2 ms. This is mainly due to fact that the CSMA channel access mechanism is disabled and that the firmware is very optimized. A few outliers (below 1%) are caused by some lost packets.

The state variables of both KFs are initialized to 2.5 m with variance $\sigma_{r_A}^2(1) = \sigma_{r_B}^2(1) = 25 \text{ m}^2$. The initial speed values instead are set equal to zero. While the speed variances $\sigma_{v_A}^2(\cdot)$ and $\sigma_{v_B}^2(\cdot)$ are estimated in real-time over the same M -long window used to compute the MA, the variances $\sigma_{e_A}^2(\cdot) = 4 \text{ m}^2$ and $\sigma_{e_B}^2(\cdot) = 4 \text{ m}^2$ associated

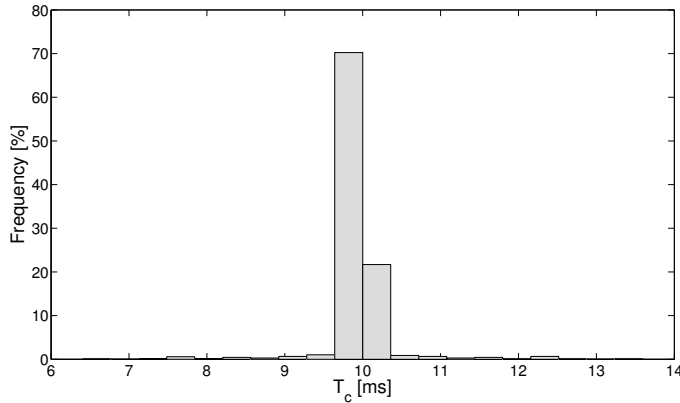


Figure 4.6: Histogram of the measured sampling time values.

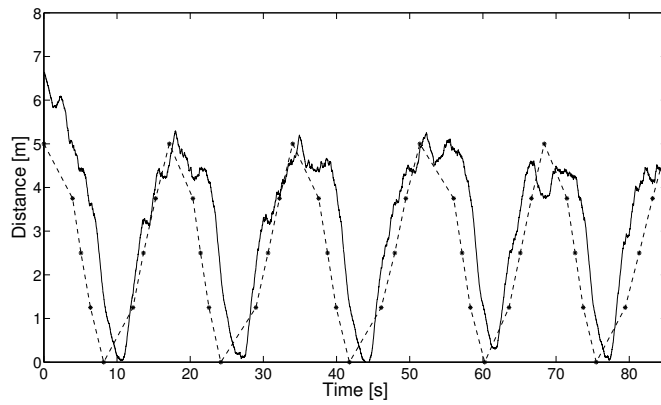
with the measured distances are kept constant as they are mostly due to the position-dependent uncertainty contributions.

In order to test the performance of the algorithm in dynamic and realistic repeatable conditions, two kinds of orthogonal experiments were conducted in the *Domotic Application Lab*. In all cases, the FA was steadily kept on top of a fixed 90-cm plastic pole located in different positions, but always at about 1 m from the walls of the room. The MTS instead was manually held by the moving user just in front of the body at about 1 m from the floor, with the MTS and FA antennas reasonably parallel to each other and always in LOS conditions. No obstacles or bodies were used to obstruct steadily the LOS communication between the two wireless devices. However, the environment was perturbed by another person moving randomly in the room.

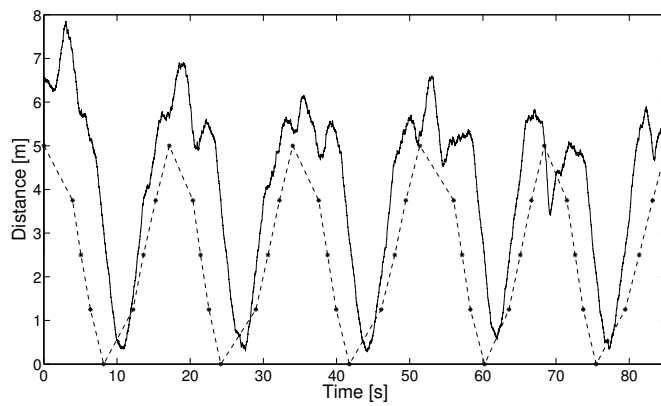
In the first experimental session, a target person repeatedly moved forth and back along a 5-m straight line radial trajectory till touching the FA. In order to make the trajectories as repeatable as possible, some reference adhesive labels were put on the floor at known distances from the FA. The values measured by the MTS in four check points (i.e., at 1.25, 2.5, 3.75 and 5 m in either direction) were marked by the user by pressing one of the buttons of the MTS, as soon as the user's leg treading on one of the labels was approximately vertical with a residual uncertainty of a few centimeters. The button press latency (including both the human reaction time and the interrupt service processing time) is roughly 200 ms. At a speed of about 1 m/s, this means that the overall intrinsic uncertainty due to the chosen experimental setup is in the order of 20 cm. The results of one of these experiments in the time domain are shown in Figure 4.7(a)-(c). In particular, Figure 4.7(a) shows the distance estimated with the proposed

algorithm, while the patterns in [Figure 4.7\(b\)](#) and [Figure 4.7\(c\)](#) refer to the output of Kalman filter A (KF A) and Kalman filter B (KF B), respectively. The quasi-triangular waveforms (dashed lines) shown in each picture represent the real trajectory as a function of time. In addition, the star markers highlight the check points, namely the moments when the button was pressed by the moving user. Note that the proposed approach improves the estimation accuracy of either individual ranging technique.

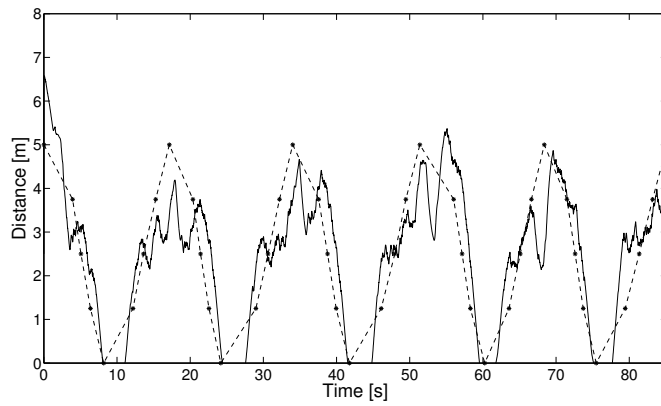
The results of a more detailed analysis are reported in [Figure 4.8](#) on page 61, which shows the box-and-whiskers plots of the errors associated with any of the four check points mentioned above. Each box refers to more than 50 data. Observe that the uncertainty is generally about 1 m. However, it may occasionally reach 2 m. Similar results are also confirmed by the second group of experiments, in which a target person moved repeatedly along a 2-m arc of a circle with the center in the FA and the radius equal to 1, 2, 3 and 4 m, respectively. Again, some stickers put on the floor and a wire of adjustable length used as a compass were used to keep the trajectories as stable and repeatable as possible. In this case the intrinsic uncertainty due to the setup is in the order of a few centimeters. The corresponding box-and-whiskers plot is shown in [Figure 4.9](#) on page 61. Observe that the worst case uncertainty tends to grow with distance, but it is quite low in the very short range. In applications where real users are involved, two main further intrinsic uncertainty contributions may seriously affect measurement results, i.e., possible changes in the relative orientation of MTS and FA antennas and poor LOS visibility (e.g., due to the posture of the person wearing the MTS or to other people steadily obstructing the LOS communication between MTS and FA). When such situations occur, uncertainty may grow from twice to three times as much. This is a common issue for all RF wireless ranging techniques, even those based on commercial platforms [66]. Nonetheless, the proposed data fusion algorithm is at least able to mitigate the detrimental effects of the uncertainty contributions described above, because the distance estimated through (4.13) relies prevalently on the measurement result with the smaller overall variance. To further reduce this problem, the position of MTS and FAs should be always chosen so as to maximize nodes reciprocal visibility (e.g., with the MTS worn on a special hat and the FAs installed at least 2 m above the floor).



(a)



(b)



(c)

Figure 4.7: Measurement results obtained with the proposed algorithm (a), with the KF A only (b) and with the KF B only (c). In all cases the target was moving forwards and backwards along a straight-line radial trajectory. The almost triangular waveform (dashed line) represents the real movement over time. The check points at 1.25, 2.50, 3.75 and 5 m from the FA are highlighted with star markers.

4.6 CONCLUSION

In this Chapter, we presented a data fusion algorithm merging RSS and ToF measurement results in order to improve wireless ranging accuracy. Both approaches have been analyzed in detail in order to evaluate the main uncertainty contributions affecting either measurement procedure. The proposed algorithm has a general validity (i.e., independent of the chosen implementation) and it relies on two MA filters to reduce the input wideband noise, a heuristic criterion able to remove easily possible large position-dependent offsets, and two KFs that use RSS- and ToF-based measurement results in a complementary manner. Due to its moderate complexity the algorithm could be integrated in future transceiver chips to support possible positioning services (e.g., for wireless sensor networks). At the moment the algorithm has been implemented and tested on the field using a dedicated embedded system made up of commercial off-the-shelf (COTS) components. The estimated accuracy is generally about 1 m, but it can be so small as 50–60 cm around a given reference distance. Accordingly, such a distance can be also set as a threshold for adjustable and omnidirectional proximity detection. This could be indeed an alternative use of the proposed technique in case of major hardware limitations. Unfortunately, the accuracy of the developed prototype is limited by the features of some hardware components, particularly the antenna that is not so isotropic as specified in the data sheet. Moreover, ToF measurement accuracy could be much better if message timestamping were done in the transceiver front end as soon as the first symbol of any packet is sent or received. However, this is not possible with COTS components. Due to the limitations above, the developed prototype can not be used in AAL applications with tracking accuracy requirements in the order of a few tens of centimeters. Nevertheless, the system is accurate enough for reliable indoor zoning and proximity detection. For instance, the platform is going to be used in an AAL project where the staff assisting mentally disabled people (e.g., affected by Alzheimer's disease) should be alerted as soon as patients enter into potentially dangerous areas, e.g., within 1 m from windows, doors, staircases, or gas cookers.

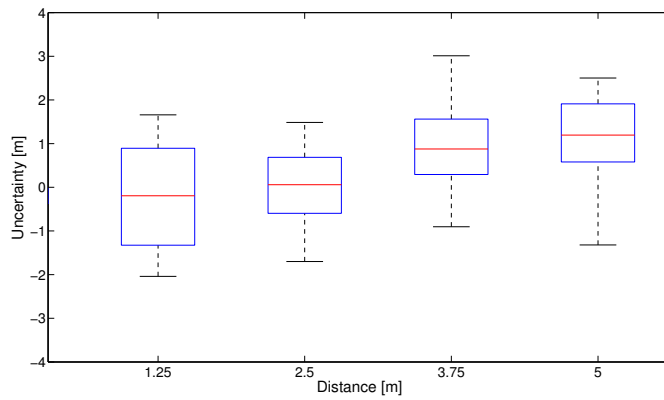


Figure 4.8: Box-and-whiskers plot of the distance uncertainty at 1.25, 2.5, 3.75 and 5 m collected when the target moves along a 5-meter straight-line forth-and-back trajectory.

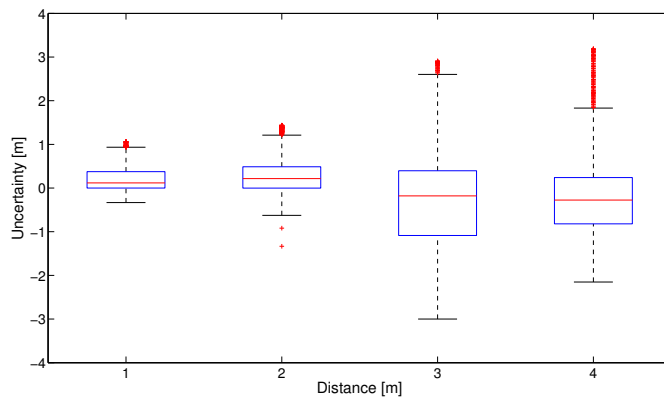


Figure 4.9: Box-and-whiskers plot of the distance uncertainty at 1, 2, 3 and 4 m collected when the target moves repeatedly along a 2-m arc of a circle with the center in the FA.

5.1 INTRODUCTION

THE STUDY we conducted in the previous Chapters deeply analyzed the main uncertainty contributions affecting both the RSS- and ToF-based wireless ranging measurement, and the related impact on the accuracy of positioning. In addition, we proposed, implemented, and tested on the field a new data fusion algorithm merging RSS and ToF measurements, that showed how combining both approaches is a sensible strategy to significantly reduce measurement uncertainty, i.e., to improve wireless ranging accuracy.

Nonetheless, as previously observed, the accuracy of ToF measurement based on the RTT is limited by the intrinsic difficulty to timestamp the received radio message with uncertainty lower than a few nanoseconds. RTT measurement uncertainty can be reduced by collecting the timestamp of any message departure or arrival at the physical layer, i.e., when the first bit or the first symbol of a frame are sent or detected by the front-end of the radio transceiver. In this case, RTT uncertainty is certainly smaller than the cumulative jitter associated with the reception of the whole message, and depends on the random time at which the peak generated by the correlator at the input of the receiver crosses the detection threshold. The latter is a function of the rising time of the correlation peak, and it results from both the SNR at the receiver input and the chosen modulation scheme. In fact, an additional key element affecting accuracy is the robustness of the adopted radio communication scheme to typical RF vagaries, such as multipath fading and interferences. For instance, it is known that the timestamping jitter can be greatly reduced when UWB signals are used [22, 67, 68]. UWB signals are indeed less sensitive than others to multipath propagation, thus making the discrimination of LOS pulses easier. Unfortunately, UWB transmitters tend to dissipate a larger amount of energy for a given range. This is the main reason why they are not commonly used in WSNs, despite a UWB physical layer (explicitly conceived for ranging purposes) has been included in the amendment IEEE 802.15.4a-2007 for PANs [69]. The same doc-

ument also describes another physical layer based on CSS. Such a scheme is to be preferred in scenarios where nodes have a high mobility, but it has been successfully used also for ranging [70, 24] and time synchronization [59] in WSNs.

Wireless ranging and time synchronization for short range PANs are typically regarded as distinct measurement problems. As a consequence, often they are also addressed independently. However, some researchers have recently pointed out that they are closely related [71]. As a matter of fact, the diffusion of measurement and control solutions based on distributed wireless embedded platforms requires that networked systems are synchronized to a common timescale (either global or local) in order to assure task coordination [72], data aggregation and fusion [48], as well as energy-efficient duty cycling [73]. Such problems are even more critical if the network topology is supposed to change, e.g., when systems are located on moving objects or worn by people. In addition, there are some applicative areas, such as surveillance, industrial monitoring or AAL, in which event detection is useless without some information on *where* and *when* this event occurs. Therefore, the problem of positioning and time synchronization can be potentially addressed using a joint approach [74], although the uncertainty sources of one problem can seriously influence the other. Indeed, if on the one hand any uncertainty contribution in the time domain will certainly affect the estimated distance between pairs of network nodes, nonetheless on the other hand the lower bound to time synchronization uncertainty depends on the inter-node communication latency (which also depends on node distance), if this is not properly estimated and compensated. The conceptual element of contact between time synchronization and wireless time-based ranging is represented by *frame timestamping*, namely the technique used to record the moment when a frame is either sent or received. It is worth emphasizing that the timestamping accuracy requirements for time synchronization are generally quite different from the ranging ones.

Time synchronization implies that time is continuously measured by every node of the network by means of a free-running counter or *clock* starting from a common epoch. Timestamping accuracy is generally not very strict at the application layer, since differences in the order of a few milliseconds are typically adequate for distributed monitoring tasks or sensor data aggregation. Sometimes synchronization uncertainty has to be so low as a few microseconds, e.g., when a time-division multiple access (TDMA) communication scheme has to

be used. In any case, MAC timestamping is usually reasonably accurate for such purposes. This means that the clock values are read as soon as a frame is encoded or decoded at the MAC layer. This is quite common for instance in WSNs relying on specific protocols such as the Flooding Time Synchronization Protocol (FTSP) [75], Tiny-Sync [76] and Average TimeSynch (ATS) [77]. Generally, MAC-layer timestamping uncertainty at the receiving end can be hardly smaller than some tens of microseconds. However, if timestamps are collected as soon as the SFD field of an incoming packet is received, uncertainty can be reduced down to 1 or 2 μs [78]. Timestamp values can be used for synchronization in two alternative ways. Either they are mapped from the local to the common network timescale *a posteriori*, i.e., on the basis of the previously estimated time and frequency offsets between pairs of nodes (this is the case of the so-called *post-facto* time synchronization used in Reference-Broadcast Synchronization (RBS) [79]) or they are used to discipline the tick rate of each local clock through a suitable controller, usually referred to as a *servo clock*. This approach is adopted also by the well-known Precision Time Protocol (PTP), currently standardized as IEEE 1588 [80], which is becoming increasingly popular even for wireless networks [81, 82, 83].

In the case of wireless ranging time synchronization is, of course, neither required, nor possible with the *two-way* RTT approach, since the measurement results refer to independent time intervals. However, if nodes were synchronized within a few nanoseconds on a common timescale, both ToA and node distance values could be easily estimated with a *one-way approach*, namely from the difference of the timestamps collected by different nodes after the frequency skew between them is compensated. Obviously, this approach requires in any case both local clocks with a (sub)-nanosecond resolution and PHY-layer timestamping.

The remainder of this Chapter is structured as follows. [Section 5.2](#) offers a short summary about the main features of the amendment IEEE 802.15.4a-2007 CSS. In [Section 5.3](#) the basic CSS signal detection problem in ideal conditions is discussed, and it is related to the moment when PHY timestamping should be performed. The underlying theoretical framework justifies and extends the validity of the experimental results presented in [59] and [84]. [Section 5.4](#) analyzes through simulations the effect of various uncertainty contributions on CSS jitter at the receiving side. In addition, an optimal frame timestamping policy at the symbol level is proposed to reduce the effect of such

contributions, thus potentially improving both ranging and time synchronization accuracy. In [Section 5.5](#) some experimental results collected using two SDR platforms are reported. Finally, in [Section 5.7](#) we draw the conclusions.

5.2 OVERVIEW OF IEEE 802.15.4A CHIRP SPREAD SPECTRUM

As shortly mentioned in the Introduction, CSS is one the alternative PHY layers for low-rate wireless personal area network (LR-WPAN) recommended in the amendment IEEE 802.15.4a-2007 [69]. The adopted modulation scheme is differential quadrature phase-shift keying DQPSK supporting a mandatory data rate of 1 Mbit/s and an optional one of 250 kbit/s with 8-ary or 64-ary bi-orthogonal coding, respectively. A total of 14 frequency channels is available in the instrumentation scientific and medical (ISM) band at 2.4 GHz. The central frequencies of such channels are spaced by 5 MHz from one another.

Generally, a chirp waveform is a modulated pulse whose instantaneous frequency changes monotonically as a function of time over an interval of duration T_{chirp} . Chirp signals are commonly used in radars [85]. A generic complex chirp waveform can be expressed as

$$s(t) = \begin{cases} c(t)e^{j\omega t} & \\ 0 & \end{cases} = \begin{cases} c(t)e^{j[2\pi f_c + \mu(t)]t} & -\frac{T_{\text{chirp}}}{2} \leq t \leq \frac{T_{\text{chirp}}}{2} \\ 0 & \text{otherwise} \end{cases} \quad (5.1)$$

where $c(t)$ is the envelope of the signal (e.g., constant if the input signal is modulated in phase), f_c is the waveform frequency at time $t = 0$ and $\mu(t)$ is the so-called chirp rate, namely the rate of change of the instantaneous frequency. If $\mu(t)$ is constant over time, then the instantaneous frequency is a linear function of t . In this case the chirp signal is referred to as a linear chirp and its bandwidth is $B = \mu T_{\text{chirp}}$. Usually, linear chirps are called up-chirps when $\mu > 0$ (i.e., when the instantaneous frequency grows over time) and down-chirps when $\mu < 0$. In the standard IEEE 802.15.4a the proposed CSS scheme is considerably more complex than the basic one described above, since communication must be robust not only to noise, but also to the interference caused by other systems potentially operating in the same area and in the same band. In particular, the standard document defines four quasi-orthogonal symbol shapes. Each symbol type (labeled as I, II, III or IV) results in turn from the sequence of four different linear subchirps of duration $T_{\text{sub}} = 1.1875 \mu\text{s}$, which occupy

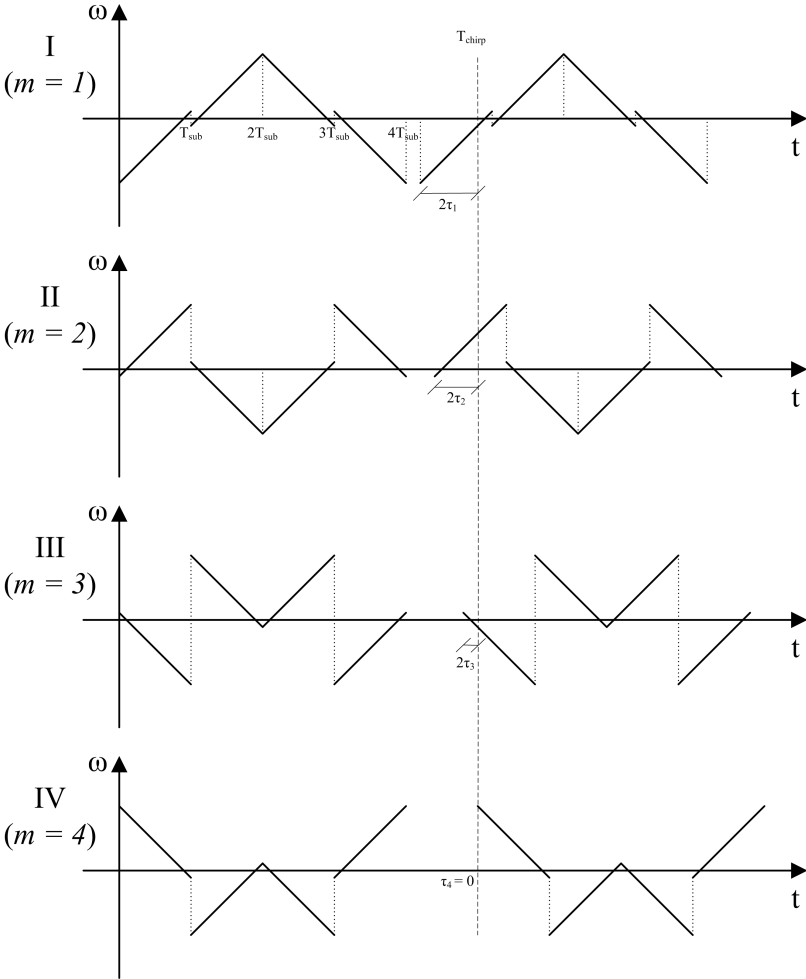


Figure 5.1: Qualitative shape of four different IEEE 802.15.4a CSS symbols as a function of time. Each type of symbol consists of four subchirps. The distance between symbols differs for $m = 1, 2, 3, 4$.

two adjacent frequency bands and differ for center frequency, chirping direction and delay between subsequent symbols. In all cases, the average chirp duration T_{chirp} is equal to $6 \mu\text{s}$.

Figure 5.1 on the preceding page shows the four different chirp symbol types as a function of time. The sub-band center frequency offsets with respect to the channel center values (expressed in MHz), the subchirp slope signs and the timing parameters for any subchirp type $k = 1, 2, 3, 4$ and for every symbol shape $m = 1, 2, 3, 4$ are reported in Table 5.1(a)-(c), respectively. The general expression of a continuous-time signal composed of N chirp symbols of type m is given by [69]

$$\begin{aligned}
 s_m(t) &= \sum_{n=0}^{N-1} s_m(t, n) = \\
 &= \sum_{n=0}^{N-1} \sum_{k=1}^4 c_{n,k} s_{k,m}(t - T_{n,k,m}) \cdot \text{PRC}(t - T_{n,k,m}) = \\
 &= \sum_{n=0}^{N-1} \sum_{k=1}^4 n_{n,k} e^{j(\omega_{k,m} + \frac{\mu}{2} \xi_{k,m} (t - T_{n,k,m}))(t - T_{n,k,m}) \cdot \text{PRC}(t - T_{n,k,m})}
 \end{aligned} \tag{5.2}$$

where:

- $n = 0, \dots, N - 1$ is the sequence number of the chirp symbol within the considered frame;
- $c_{n,k}$ is the complex data sequence resulting from the differential quadrature phase-shift keying (DQPSK) input coding;
- $\mu = 2 \cdot \pi \cdot 7.3158 \cdot 10^{12} [\text{rad/s}^2]$ is the rate of change of the subchirp frequency;
- $\omega_{k,m} = 2\pi f_{k,n}$ represents the center frequency of the k th subchirp in the channel centered in f_c ;
- $\xi_{k,m} = \{+1, -1\}$ provides the chirping direction;
- the term

$$T_{n,k,m} = \left(k + \frac{1}{2}\right) T_{\text{sub}} + n T_{\text{chirp}} - [1 - (-1)^n] \tau_m \tag{5.3}$$

defines the delay of the k th subchirp of the n th symbol from the beginning of the considered frame, and τ_m is the time gap

Table 5.1: Sub-band center frequencies $f_{k,m}$ in MHz (a), chirping directions $\xi_{k,m}$ (b) and temporal parameters (c) of different subchirps for different symbol types as reported in the standard IEEE 802.15.4a.

(a)

$m \backslash k$	1	2	3	4
1	$f_c - 3.15$	$f_c + 3.15$	$f_c + 3.15$	$f_c - 3.15$
2	$f_c + 3.15$	$f_c - 3.15$	$f_c - 3.15$	$f_c + 3.15$
3	$f_c - 3.15$	$f_c + 3.15$	$f_c + 3.15$	$f_c - 3.15$
4	$f_c + 3.15$	$f_c - 3.15$	$f_c - 3.15$	$f_c + 3.15$

(b)

$m \backslash k$	1	2	3	4
1	+1	+1	-1	-1
2	+1	-1	+1	-1
3	-1	-1	+1	+1
4	-1	+1	-1	+1

(c)

Parameter	Value	Multiple of 1/32 MHz
T_{chirp}	6 μs	192
T_{sub}	1.1875 μs	38
τ_1	468.75 ns	15
τ_2	312.5 ns	10
τ_3	156.25 ns	5
τ_4	0 ns	0

between two subsequent chirp symbols of type m , as shown in [Figure 5.1](#).

Finally,

$$P_{\text{RC}}(t) = \begin{cases} 1 & |t| \leq \frac{3}{5} \frac{T_{\text{sub}}}{2} \\ \frac{1}{2} + \frac{1}{2} \cos \left[\frac{5\pi}{T_{\text{sub}}} \left(|t| - \frac{3}{5} \frac{T_{\text{sub}}}{2} \right) \right] & \frac{3}{5} \frac{T_{\text{sub}}}{2} < |t| \leq \frac{T_{\text{sub}}}{2} \\ 0 & |t| > \frac{T_{\text{sub}}}{2} \end{cases} \quad (5.4)$$

is a raised cosine window which is applied to every subchirp to reduce intersymbol interference (ISI). It is worth noticing that, even if [\(5.2\)](#) is a continuous-time function, the default baseband sampling frequency of IEEE 802.15.4a signals is 32 MSa/s. This is the reason why all temporal parameters, such as those shown in [Table 5.1\(c\)](#), can be equivalently expressed in terms of a multiple of the sampling period.

5.3 THEORETICAL MODEL

As described in [Section 5.2](#), an IEEE 802.15.4a CSS symbol consists of four subchirps. If we focus our attention only on the detection of a single subchirp of type k , regardless of the symbol shape and of the position of the subchirp in the symbol itself, the subscripts n and m in [\(5.2\)](#) and [\(5.3\)](#) can be safely omitted. Consequently, the received signal can be approximately modeled as

$$r_k(t) = \sum_{p=1}^P a_p \tilde{s}_k(t - D_{k,p}) + w(t) \quad (5.5)$$

where $\tilde{s}_k(\cdot)$ results from the down-conversion of $s_{k,m}(\cdot)$, P is the number of significant subchirp replicas due to multipath propagation, a_p is a complex quantity representing the attenuated I/Q components of the p th replica, $w(t)$ is a zero-mean complex wideband AWGN with variance σ_w^2 and $T_{n,k,m}$ can be replaced by a generic delay term $D_{k,p}$ including both the sending time elapsed from a given arbitrary epoch and the ToA of the considered subchirp along the p th propagation path. Let $h_k(t) = s_k^*(-t)$ be an ideal continuous-time matched filter for subchirp of type k . If we assume that

1. the AWGN is negligible;

2. the LOS contribution in (5.5) is much larger than the scattered replicas (i.e., $a_1 \gg a_p$ for $p = 2, \dots, P$);
3. the raised cosine function (5.4) is approximated by a rectangular window having the same duration T_{sub} and the same energy as (5.4);

after some mathematical steps it results that the signal at the output of the matched filter is

$$y_k(t) \cong \int_{-\infty}^{+\infty} a_1 \tilde{s}_k(\tau - D_{k,1}) h_k(t - \tau) dt \cong \begin{cases} a_1 \frac{4}{5} \left(T_{\text{sub}} - |t - D_{k,1}| \right) \cdot \text{sinc} \left[\frac{\mu \xi_k}{2} (t - D_{k,1}) \right] \cdot \left(T_{\text{sub}} - |t - D_{k,1}| \right) \cdot e^{j\tilde{\omega}_k(t - D_{k,1})} & -T_{\text{sub}} \leq |t - D_{k,1}| \leq T_{\text{sub}} \\ 0 & \text{otherwise} \end{cases} \quad (5.6)$$

where $\tilde{\omega}_k = \omega_{k,m} - \omega_c$ is the center frequency of the k th subchirp after down-conversion. Of course, in the case of direct conversion receiver (DCR) then. Observe that the magnitude of (5.6) is maximum (i.e., equal to $4/5 \cdot T_{\text{sub}}$) for $t = D_{k,1}$. Unfortunately, when also (5.4) is considered in the computation, the analytical expression of the correlation result is too cumbersome to be reported.

The two pulses in Figure 5.2 on the next page refer to the theoretical approximate expression (5.6) (dashed line) and the numerical results obtained including the additional raised cosine window (5.4). Clearly, the results are very similar within the main pulse (which is the most interesting part), although the amplitude of the simulated correlation peak is about 5% smaller than $4/5 \cdot T_{\text{sub}}$ due to the smooth roll-off of the raised cosine window. Nonetheless, it is worth noticing that the position of the peaks is exactly the same in both cases.

Expression (5.6) suggests that the subchirp correlation pulse can be effectively used for PHY-layer timestamping on the receiving side. In fact, using this approach the uncertainty contributions introduced by MAC and upper layers are inherently bypassed. Nevertheless, the moment when the peak is detected is generally affected by the following phenomena, i.e.:

- Incoherent baseband sampling and finite temporal resolution;
- Wideband noise;

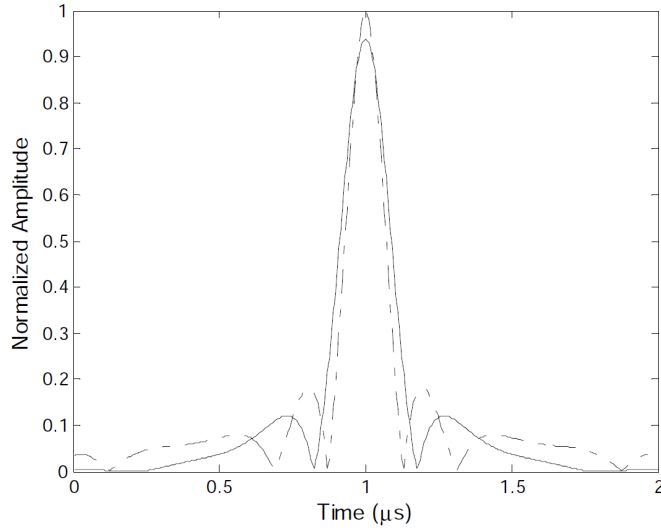


Figure 5.2: IEEE 802.15.4a subchirp correlation pulse for $k = 2$. The dashed line refers to the theoretical curve given by (5.6), whereas the solid one results from simulations. The difference between curves is due to the raised cosine (5.4), but the position of the peaks is the same in both cases.

- Frequency offsets between transmitters and receivers;
- Multipath propagation and fading.

Therefore, any timestamp value associated with the detection of a single subchirp can be described by the following random variable:

$$\mathbf{D}_k = \arg \max_{t \in \mathbb{R}} \{y_k(t)\} + \varepsilon_s + \varepsilon_n + \varepsilon_o + \varepsilon_p \quad (5.7)$$

where the random variables ε_s , ε_n , ε_o and ε_p refer to the uncertainty contributions due to effect of sampling, noise, frequency offsets, and multipath, respectively. In the next Section, the impact of any of such contributions is analyzed both qualitatively and through simulations. Observe that in the leftmost term of (5.7) the p subscript is not reported because \mathbf{D}_k depends indeed on the superimposition of all replicas.

5.4 UNCERTAINTY ANALYSIS AND SYMBOL TIMESTAMP DEFINITION

The influence of each individual uncertainty contribution defined in Section 5.3 has been assessed through numerical simulations over 10 000 runs. If no otherwise stated, the subchirp simulation parameters refer to the second subchirp (i.e., $k = 2$) of symbol $m = 4$.

Table 5.2: Post-interpolation errors for 10 different fractional delays between 0 and T_s .

Fractional delay	0	10%	20%	30%	40%	50%	60%	70%	80%	90%
[% of T_s]										
ε_s [ps]	0	-110	-194	-223	-169	0	169	223	194	110

However, the obtained results can be immediately generalized to any other subchirp and symbol type.

5.4.1 Incoherent baseband sampling and finite temporal resolution

Since the down-converted IEEE 802.15.4a waveforms are supposed to be sampled at $F_s = 32 \text{ MSa/s}$ [69], the correlation defined in (5.6) is actually implemented in the digital domain. However, waveform sampling is generally incoherent, namely asynchronous with the input signals. Therefore, the peak of (5.6) may occur at any time between two consecutive sampling instants. This equivalently means that the uncertainty contribution ε_s in (5.7) can be reasonably modeled with a uniform random variable in the range $[0, T_s]$, with $T_s = 1/F_s$. The corresponding standard deviation is about $T_s/2\sqrt{3} = 9 \text{ ns}$. This value can be reduced through well-known interpolation techniques. In particular, parabolic interpolation offers a good trade-off between accuracy and computational complexity (i.e., suitable for a possible on-chip implementation). Accordingly, the estimated position of the correlation peak results from [86]

$$\hat{D}_k = \left(l_{\text{peak}} + \frac{|y_k[l_{\text{peak}} - 1]| - |y_k[l_{\text{peak}} + 1]|}{2(|y_k[l_{\text{peak}} - 1]| - 2|y_k[l_{\text{peak}}]| + |y_k[l_{\text{peak}} + 1]|)} \right) \cdot T_s \quad (5.8)$$

where $y_k[l] \triangleq y_k(l \cdot T_s)$, and $l_{\text{peak}} = \arg \max_{t \in \mathbb{Z}} \{y_k[t]\}$. If sampling period fluctuations and additive noise are assumed to be negligible, the residual post-interpolation uncertainty (still described by the random variable ε_s for brevity) is expected to be much smaller than $T_s/2\sqrt{3}$. Table 5.2 reports the post-interpolation error values for 10 different fractional delays between 0 and T_s . Observe that ε_s exhibits a cyclic behavior and the corresponding absolute values are much

smaller than 1 ns. Such uncertainty values are compatible with the timestamping requirements described in the Introduction, regardless of the distribution of ε_s .

5.4.2 Wideband Noise

As known, the AWGN superimposed to the rising or falling edges of a binary waveform affects the time when a given threshold level is crossed. In particular, if the SNR is large enough, such a timing jitter exhibits a zero-mean Gaussian distribution with a standard deviation that, in a first approximation, grows linearly with the standard deviation of the noise and it is inversely proportional to the absolute value of the edge slope. Similar considerations hold also for the random variable ε_n in (5.7), since the sides of the correlation pulse in (5.6) are almost linear. However, in this case the overall jitter is about twice as much because the peak of the correlation pulse results from the intersection of a rising and a falling edge. In order to quantify the effect of the additive noise on D_k (taking into account both the thermal noise and the internal noise of the receiver), various distributions of ε_n for different SNR values were generated through Monte Carlo simulations. In all simulations $D_{k,1} = 1000 \cdot T_s$ (i.e., an integer multiple of T_s) and the AWGN was added to the received waveform *before* the matched filter and the digital interpolator described in Section 5.4.1. Some results are shown in Figure 5.3. An histogram describing the distribution of ε_n for SNR = 30 dB is shown in Figure 5.3(a). Clearly, the distribution is Gaussian and centered in zero, as expected. A more complete analysis of the effects of the wideband noise is visible in Figure 5.3(b), where the mean and the standard deviation values of ε_n are reported as a function of the SNR. Observe that the mean values are always negligible, whereas the standard deviation is about 2.8 ns for SNR = 10 dB and becomes smaller than 1 ns for SNR > 20 dB. Therefore, the effect of wideband noise on subchirp peak detection is generally not very relevant for typical SNR values.

5.4.3 Frequency Offsets

In the general analysis reported in Section 5.3, the instantaneous frequency of the received subchirp is assumed to be exactly the same as the chirping frequency used in the matched filter. However, this condition is not very realistic, because of the tolerances and the jit-

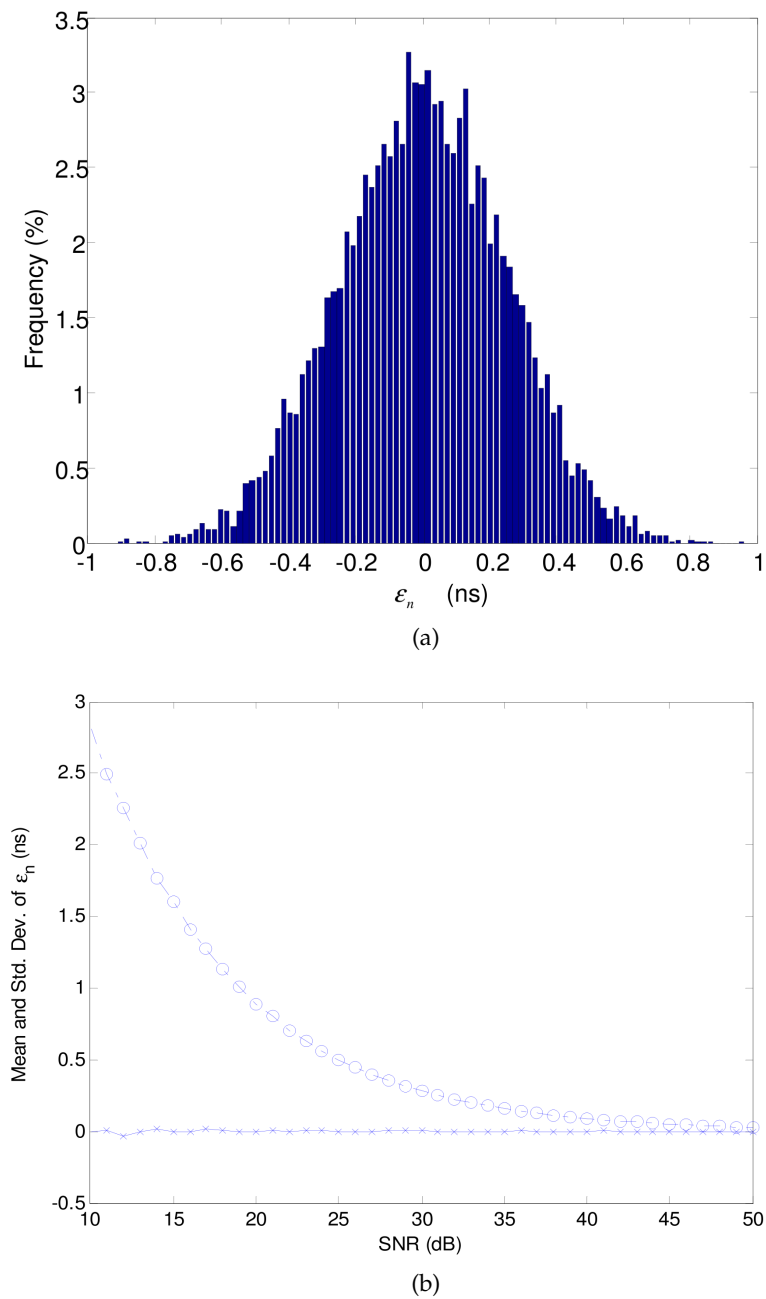


Figure 5.3: Effect of AWGN on timestamping jitter. In (a) the histogram refers to SNR = 30 dB. In (b) the mean value (solid line with cross markers) and the standard deviation (dashed line with dot markers) of ε_n are reported as a function of the SNR.

ter of the oscillators used both in the transmitter (TX) and in the receiver (RX). If we refer to $\Delta\tilde{\omega}_k$ as the random variable modeling the TX-RX frequency offset after down-conversion, the output of the matched filter under the same assumptions specified in Section 5.3 is given by

$$y_k(t) \cong \begin{cases} a_1 \frac{4}{5} (T_{\text{sub}} - |t - D_{k,1}|) \cdot \\ \quad \cdot \text{sinc} \left[\left(\frac{\Delta\tilde{\omega}_k + \mu\xi_k(t - D_{k,1})}{2} \right) \right] \cdot \\ \quad \cdot (T_{\text{sub}} - |t - D_{k,1}|) \cdot \\ \quad \cdot e^{j\frac{2\tilde{\omega}_k + \Delta\tilde{\omega}_k}{2}(t - D_{k,1})} & -T_{\text{sub}} \leq |t - D_{k,1}| \leq T_{\text{sub}} \\ 0 & \text{otherwise} \end{cases} \quad (5.9)$$

Note that in the ideal case (i.e., when $\Delta\tilde{\omega}_k = 0$) (5.9) coincides with (5.6), as expected. On the contrary, when $\Delta\tilde{\omega}_k \neq 0$, it can be easily shown that the magnitude of (5.9) is maximum for $t \cong D_{k,1} - [\Delta\tilde{\omega}_k / (\mu\xi_k)]$. Therefore, according to (5.7) the uncertainty contribution due to the frequency offset is approximately $\varepsilon_o \cong -[\Delta\tilde{\omega}_k / (\mu\xi_k)]$. In general $\Delta\tilde{\omega}_k$ can be regarded as a normal random variable with non-zero mean and variance depending on the stability of the chosen oscillators. However, for very short time intervals (e.g., so long as T_{chirp}), can be reasonably assumed to be constant. Therefore, the effect of the frequency offsets in the very short term can be regarded as systematic. The results of some simulations for subchirps $k = 2$ and $k = 3$ are shown in Figure 5.4(a) and 5.4(b), respectively, as a function of the frequency offset, for SNR = 30 dB. In all cases the nominal subchirp delay on the chosen timescale is the same as in Section 5.4.2. Observe that frequency offsets cause a linear time shift proportional to the value of the offset itself (≈ 120 ps/kHz). This means that in the case of a 2.4 GHz oscillator with a tolerance of ± 50 ppm the largest possible frequency offset can reach ± 120 kHz and the total time shift can be so large as ± 14 ns. Consider that the trend of the time shift is related not only to the sign of the offset *per se*, but also to the chirping direction ξ_k . This is the reason why the behavior of the systematic shift in Figure 5.4(a) and 5.4(b) is opposite. Note also that the standard deviation around the systematic time shift is constant and

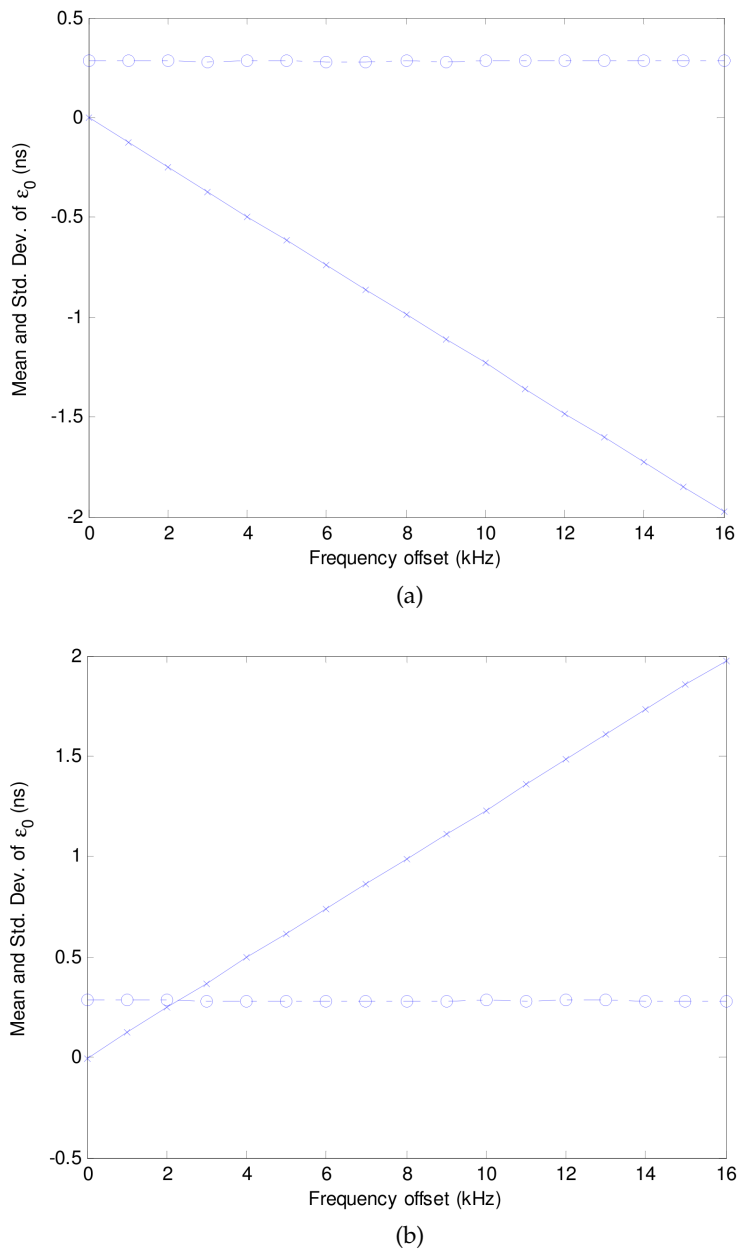


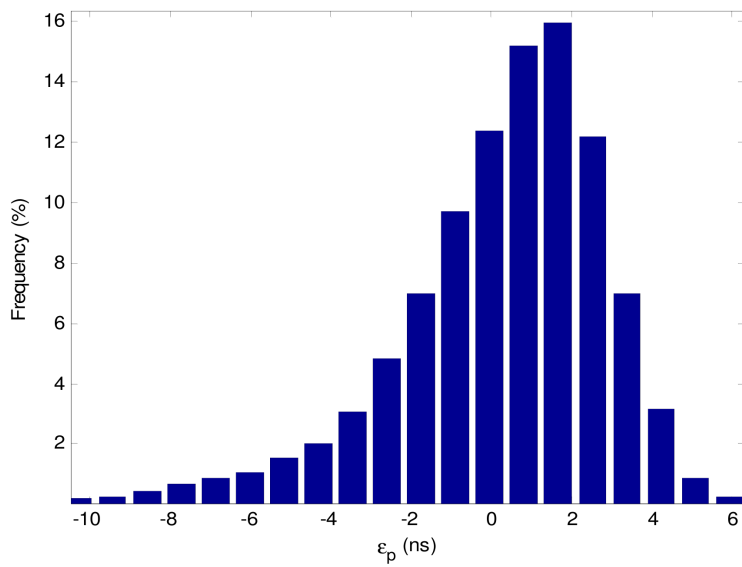
Figure 5.4: Mean value (solid line with cross marks) and standard deviation (dashed line with dot marks) of ϵ_0 as a function of different systematic transmitter-receiver frequency offsets for subchirps $k = 2$ (a) and $k = 3$ (b), respectively, when SNR = 30 dB.

equal to 280 ps, because it is due only to the AWGN. Therefore, ε_o exhibits the same Gaussian distribution shown in Figure 5.3(a), but with a mean value that changes linearly with the frequency offset.

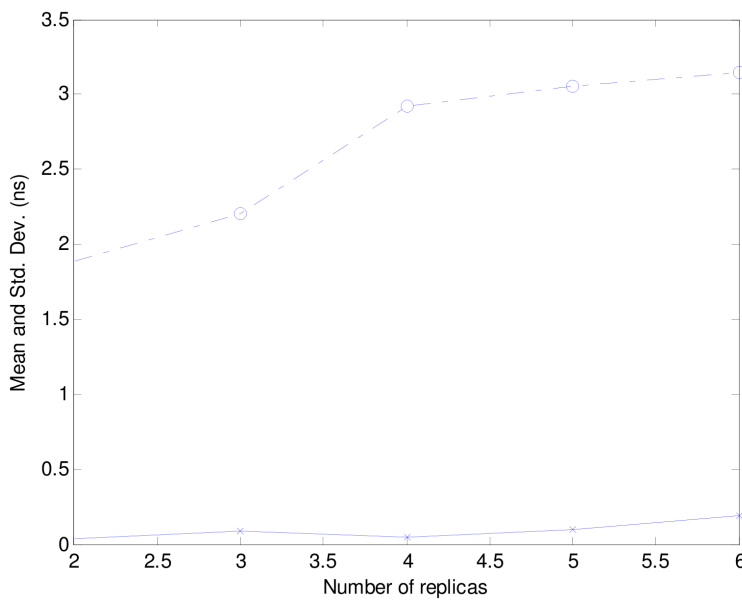
5.4.4 Multipath Propagation

As known, multipath propagation generally changes the ideal shape and the position of the received correlation peaks due to the random overlap of multiple signal replicas. The amount of distortion as well as the time fluctuations affecting the correlation pulses strongly depend on the environment and may be particularly serious in NLOS conditions [87]. Therefore, in order to analyze quantitatively this phenomenon and to build a trustworthy distribution of ε_p , an appropriate propagation model must be preliminarily chosen for simulation purposes. In our case the classic logarithmic path loss model $PL_p = PL_0 + 10\gamma_p \cdot \log(d/d_0)$ is used to describe signal attenuation. PL_0 represents the path loss at a reference distance $d_0 = 1$ m (e.g., $PL_0 = -40$ dB), d is the actual TX-RX distance, and γ_p for $p = 1, \dots, P$ is the path loss coefficient associated with the p th signal replica. In practice, $\gamma_1 = 2$ for the LOS component (i.e., like in the ideal free-space case), while the other γ_p values are assumed to be uniformly distributed between 2.3 and 2.7 [88]. Such random variations model the changeable attenuations experienced by different replicas due to both the reflections caused by different objects and the variable length of the various propagation paths. The interarrival time between subsequent replicas is assumed to be random and exponentially distributed with a mean value which depends on the average distance between TX and RX. This memory-less model is usually too simple to capture the real complexity of specific indoor environments. Nonetheless, it is general enough to describe multipath propagation delays with reasonable accuracy in different contexts [89]. The SNR at the receiving end is set equal to 30 dB as in the previously simulated case. Finally, the phase of the replicas is supposed to be uniformly distributed in $[-\pi, \pi]$. On the basis of the assumptions above, the temporal position of the correlation peak at the output of the interpolation block is subjected to random fluctuations exhibiting a distribution as shown in Figure 5.5(a).

In the considered case study, the mean interarrival time is set equal to 5 ns and $P = 6$. Note that the distribution of ε_p ranges between -10 ns and $+6$ ns, with a mean value of 0.15 ns. In this case, the effect



(a)



(b)

Figure 5.5: (a) Distribution of ϵ_p in the presence of a strong multipath interference for a mean interarrival time equal to 5 ns; (b) Mean value (solid line with cross markers) and standard deviation (dashed line with dot marks) of ϵ_p , as a function of the number of replicas P.

of multipath interference is actually dominated by the phase variations of the replicas. It should be emphasized that this is a quite pessimistic scenario. Indeed, when the transmitter and the receiver are located at a fixed distance from each other and the surrounding environment does not change significantly, the random variations are expected to be smaller and may turn into systematic offsets [66]. In such cases, the measured receiving jitter can be lower than the simulated one reported above. In [Figure 5.5\(b\)](#) the mean and the standard deviation of ε_p are plotted as a function of P using the same values listed above. Clearly, uncertainty tends to grow with the number of received replicas, but their power becomes smaller and smaller till being comparable to the noise floor. In particular, with the chosen values of the simulation parameters this condition occurs for $P > 6$. On the other hand, when the mean interarrival time grows (e.g., in a larger environment), replicas attenuation and dispersion also increase. Therefore, the influence of the LOS component on the correlation pulse tends to prevail over the higher-order replicas. As a result, the jitter affecting the peak decreases.

5.4.5 Definition of Symbol Timestamp

Instead of considering a single subchirp, a radio message can be potentially timestamped at the symbol level as shown in [Figure 5.5](#). In this case, the symbol timestamp \hat{X} can be simply defined as

$$\hat{X} = \frac{1}{4}(\hat{D}_1 + \hat{D}_2 + \hat{D}_3 + \hat{D}_4) \quad (5.10)$$

where \hat{D}_1 , \hat{D}_2 , \hat{D}_3 and \hat{D}_4 refer to the estimated temporal positions of the correlation peaks of four subchirps belonging to the same IEEE 802.15.4 symbol. Again, the subscripts n and m are omitted in (5.10), because this definition is absolutely general, i.e. independent of the symbol shape and of the position of the symbol in the frame. The advantage of using symbol timestamping is a direct consequence of the results shown in the previous subsections. First of all, the symmetrical shape of the subchirps within any IEEE 802.15.4a symbol can be exploited to compensate for the systematic time shifts caused by the residual frequency offset between TX and RX. Indeed, it was shown in [Section 5.4.3](#) that for a given frequency offset such time shifts tends to change in opposite directions when the chirping slopes are also opposite. Since any IEEE 802.15.4a CSS symbol consists of two up-

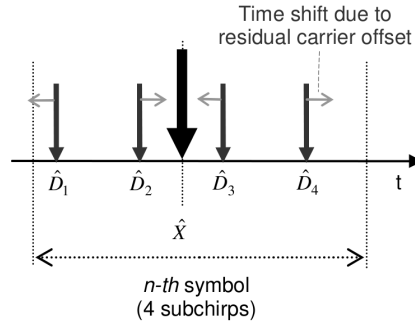


Figure 5.6: Definition and benefits of IEEE 802.15.4a CSS frame timestamping at the symbol level.

subchirps and two down-subchirps with the same rate (in absolute value), using (5.10) the systematic time shifts caused by subsequent subchirps tend to cancel out each other, as shown in Figure 5.6. In addition, by averaging four subsequent and mostly independent time values, the random fluctuations due to noise and multipath can be roughly reduced by a factor 2, thus further improving timestamping precision.

5.5 EXPERIMENTAL CHARACTERIZATION

5.5.1 Experimental Setup

The performances of CSS-based frame timestamping both at subchirp and at a symbol level have been evaluated experimentally on the field using two different universal software radio peripheral (USRP) platforms by Ettus Research LLC. Such platforms (called USRP 1 and USRP N210) are used for up- and down-conversion of RF signals as well as for analog-to-digital and digital-to-analog conversion. The RF front-end of both platforms relies on interchangeable daughterboards receiving and transmitting signals up to 5.8 GHz. In particular, for the tests described in the following, both platforms were equipped with a RFX2400 transceiver connected to a omnidirectional dipole antenna. Baseband digital signal processing is implemented with GNU Radio, a Python-C++ open-source tool for SDR solutions running on two PCs [90]. The USRP 1 is connected to the host PCs through a USB 2.0 link at 480 Mbit/s. It supports radio communications in channels with a bandwidth of up to 16 MHz and it is equipped with four 64 MSa/s 12-bit analog-to-digital converters ADCs and four 128 MSa/s digital-to-analog converters (DACs). Also, it in-

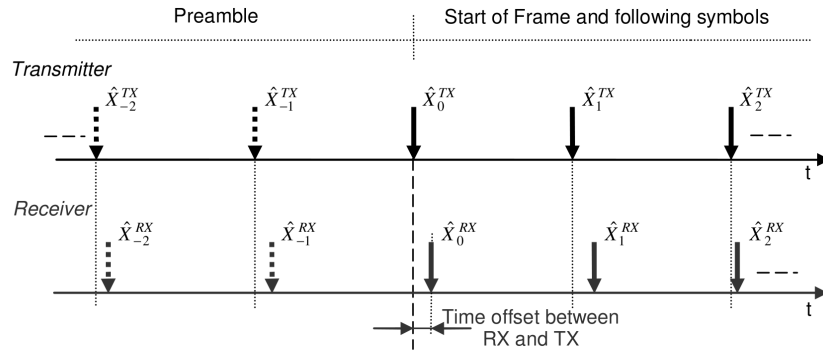


Figure 5.7: Symbol timestamping on the timescales of transmitter and receiver. The initial time offset due to different epochs is preliminary compensated.

cludes an Altera Cyclone field programmable gate array (FPGA) that can be used to implement four digital digital down-converters (DDCs) and two digital up-converters (DUCs) with programmable interpolation rates. The USRP N210 is similar to the USRP 1, but it is connected to the PCs through a Gigabit Ethernet link and it is provided with two 100 MSa/s 14-bit analog-to-digital converters (ADCs), two 400 MSa/s 16-bit DAC and a Xilinx Spartan XC3SD3400A FPGA. This enables real-time data transfers of signals with a bandwidth of up to 50 MHz. During the experiments, the USRP platforms were kept steadily at a distance of a few meters with antennas parallel to one another. No specific setups for multipath reduction were used. Since the daughter-boards operate between 2300 MHz and 2900 MHz, they perfectly cover the band between 2400 and 2483.5 MHz. In order to test the proposed timestamping mechanisms in different conditions, various configurations were used (e.g., using the USRP 1 and USRP N210 alternatively as TX or RX). Unfortunately, neither the USRP 1 nor USRP N210 are able to support real-time data transfers of I/Q samples at a rate of 32 MSa/s. For this reason, the experiments were conducted at variable sample rates between 4 MSa/s and 25 MSa/s. Moreover, due to the limitations of the available experimental setup, the USRP 1 was set only in receiving mode when used in combination with the URSP N210. The in-channel SNR was measured with a spectrum analyzer Tektronix RSA3408A and further estimated a posteriori using the received data stream, in order to make the comparison between experimental and simulated results as trustworthy and consistent as possible.

5.5.2 Performance Metrics

In the experiments the arbitrary epoch of (5.6) corresponds to the transmission instant of the first subchirp of the first symbol on the TX timescale. In normal wireless operation, a common time reference between TX and RX usually is not available, unless a time synchronization protocol is used. Therefore, in general a certain time offset exists between the TX timestamp of the n th symbol and the RX timestamp of the same symbol within a given frame, as shown in Figure 5.7. This time offset is not constant, due to the frequency offsets of the local oscillators and the accumulation of frequency and phase noise contributions. In order to estimate the timestamping uncertainty without implementing any advanced synchronization algorithm, an offline offset compensation procedure is used. The proposed procedure relies on the fact that the TX timestamps are easily calculated as multiples of the sample time, since the subchirps are generated locally and the symbol position is predictable (a symbol is indeed composed of exactly 192 samples). Therefore, the time offset between TX and RX can be reset a posteriori. After compensating the offset, the following metrics can be used for timestamping performance evaluation, i.e.

- *Mean symbol timestamp error.* This is defined as:

$$\text{STE} = \frac{1}{N} \sum_{n=0}^{N-1} \left(\frac{\hat{X}_n^{\text{RX}}}{1 + \hat{\rho}} - \hat{X}_n^{\text{TX}} \right) \quad (5.11)$$

where

- \hat{X}_n^{TX} and \hat{X}_n^{RX} are the timestamps of the n th symbol estimated on the TX and RX timescales, respectively, assuming that the common epoch defined in (5.6) corresponds to the TX time of the first subchirp of the first symbol;
- $\hat{\rho}$ is the estimated relative frequency skew between RX and TX which results from:

$$\hat{\rho} = \frac{2}{N} \sum_{n=0}^{\frac{N}{2}-1} \frac{\hat{X}_{n+\frac{N}{2}}^{\text{RX}} - \hat{X}_n^{\text{RX}}}{\hat{X}_{n+\frac{N}{2}}^{\text{TX}} - \hat{X}_n^{\text{TX}}} - 1 \quad (5.12)$$

where the average is computed taking the differences of $N/2$ pairs of symbols in the same frame at a distance of $N/2$ symbols from each other. In fact, this approach makes

Table 5.3: Single subchirp timestamping accuracy analysis.

TX	RX	F_s	SNR	$\hat{\rho}$	Mean Val.	Std. Dev.
		[MSa/s]	[dB]	[ppm]	[ns]	[ns]
USRP 1	USRP 1	4	33	2.3	58	54
USRP N210	USRP 1	4	31	13	210	225
USRP N210	USRP N210	4	32	0.4	16	22
USRP 1	USRP 1	8	30	1.6	9.8	10
USRP N210	USRP 1	8	31	13	56	57
USRP N210	USRP N210	8	32	0.4	-0.9	4.5
USRP N210	USRP 1	16	30	11	14	15
USRP N210	USRP N210	16	32	0.4	10	12
USRP N210	USRP N210	25	32	0.3	1.9	1.7

the estimation variance smaller than computing the differences between adjacent symbols.

- *Standard deviation of the symbol timestamping error.* This is the standard deviation of the symbol timestamp error within a received frame, i.e.

$$\sigma_{\text{STE}} = \sqrt{\frac{1}{N-1} \sum_{n=0}^{N-1} \left(\frac{\hat{X}_n^{\text{RX}}}{1+\hat{\rho}} - \hat{X}_n^{\text{TX}} - \text{STE} \right)^2} . \quad (5.13)$$

5.6 EXPERIMENTAL RESULTS

In every experimental run 2000 frames of 86 symbols each (corresponding to 344 subchirp and 66 048 samples per frame) were transferred between different platforms. The corresponding measurement results are reported in [Table 5.3](#) and [Table 5.4](#). In all cases the SNR is about 30 dB. Before analyzing the performance metrics mentioned above, we also checked experimentally that the assumptions underlying the symbol timestamping policy defined in [Section 5.4.5](#) hold true. [Table 5.3](#) shows the mean values and the standard deviations of the subchirp timing position errors (namely the differences between

Table 5.4: Symbol timestamping accuracy analysis.

TX	RX	F_s [MSa/s]	SNR [dB]	$\hat{\rho}$ [ppm]	STE [ns]	σ_{STE} [ns]
USRP 1	USRP 1	4	33	2.3	2	10
USRP N210	USRP 1	4	31	13	1.1	2.4
USRP N210	USRP N210	4	32	0.4	0.88	2.2
USRP 1	USRP 1	8	30	1.6	0.12	1.6
USRP N210	USRP 1	8	31	13	0.10	2.1
USRP N210	USRP N210	8	32	0.4	-0.03	1.5
USRP N210	USRP 1	16	30	11	0.1	0.35
USRP N210	USRP N210	16	32	0.4	0.1	0.36
USRP N210	USRP N210	25	32	0.3	-0.2	0.16

the estimated \hat{D}_k values and the nominal ones calculated with respect the beginning of the frame) computed over all the subchirps of the same frame. Observe that the accuracy in detecting the temporal position of the subchirp correlation peaks increases as the sampling rate grows. This is reasonable because the temporal resolution is better and also the absolute resolution of the parabolic interpolator improves. On the other hand, the use of a particular hardware platform does not noticeably affect the estimation of the correlation peak. Observe that the mean estimation errors are strongly affected by the relative TX-RX frequency offset. In this respect, it is worth emphasizing that the uncertainty associated to the $\hat{\rho}$ values resulting from (5.12) and reported in Table 5.3 is negligible. This behavior is in accordance with the simulation-based analysis reported in Section 5.4 and it confirms that the detection of the subchirp correlation peak is not the best choice for frame timestamping. Notice also that at lower sampling rates the mean errors are quite larger than expected because of the bias introduced by the analog RF sections before the ADC stage. However, such systematic contributions become negligible when F_s exceeds 20 MSa/s. As expected, the effect of the frequency offsets can be strongly reduced if the symbol timestamping mechanism defined in Section 5.5.2 is used.

In [Table 5.4](#) the metrics defined in the previous Section are applied to the same data records used to build [Table 5.3](#). The values of STE and σ_{STE} have been estimated accordingly. The performance metric values show that the symbol timestamping is affected by fluctuations with a sub-nanosecond mean value and a standard deviation ranging between a few ns at lower data rates down to some hundreds of ps at 25 MSa/s. Two exemplifying distributions of total symbol timestamping errors are shown in [Figure 5.8\(a\)](#) and [5.8\(b\)](#), for $F_s = 8$ MSa/s and $F_s = 16$ MSa/s, respectively. Such distributions are compatible with the simulations shown in [Section 5.4](#), although the effect of multipath is not particularly evident in the chosen environment. Moreover, we expect that a fully compliant IEEE 802.15.4a CSS-based implementation (i.e., at 32 MSa/s) may assure even better performance, thus enabling joint wireless time synchronization and ranging.

5.7 CONCLUSION

High-accuracy positioning and time synchronization techniques for wireless portable devices are expected to boost the role of PANs in many applicative areas such as AAL, home automation, surveillance and logistics. Unfortunately, wireless ranging based on ToF measurements is heavily influenced by many layered uncertainty contributions introduced by the communication stack and by the usual vagaries of radio propagation. A necessary condition to reduce ToF measurement uncertainty is to timestamp both sent and received frames at the physical layer using special RF communication schemes that are more robust to noise, multipath propagation phenomena and residual frequency offsets between transmitters and receivers. The CSS scheme described in the amendment IEEE 802.15.4a is often considered as one of the most effective solutions to this aim. The analysis and the results reported in this Chapter confirm that IEEE 802.15.4a CSS can be used for accurate frame timestamping, even in the presence of significant nonidealities. Therefore, time synchronization can be also enhanced accordingly. While the native jitter affecting the correlation peak of a single received subchirp is in the order of some nanoseconds, frame timestamping accuracy can be further improved by means of two complementary techniques, i.e.,:

- by using a simple digital parabolic interpolator at the output of the matched filter associated with each subchirp type;

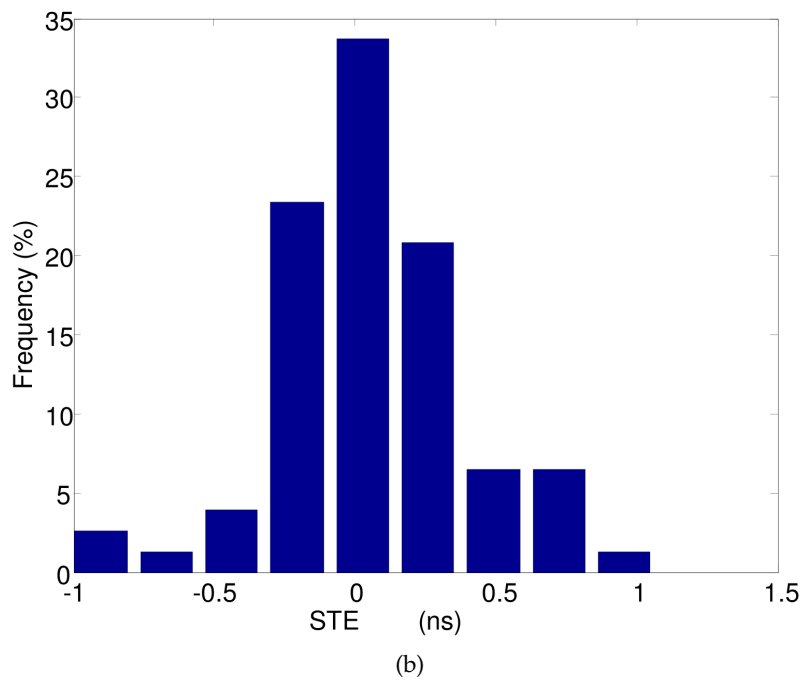
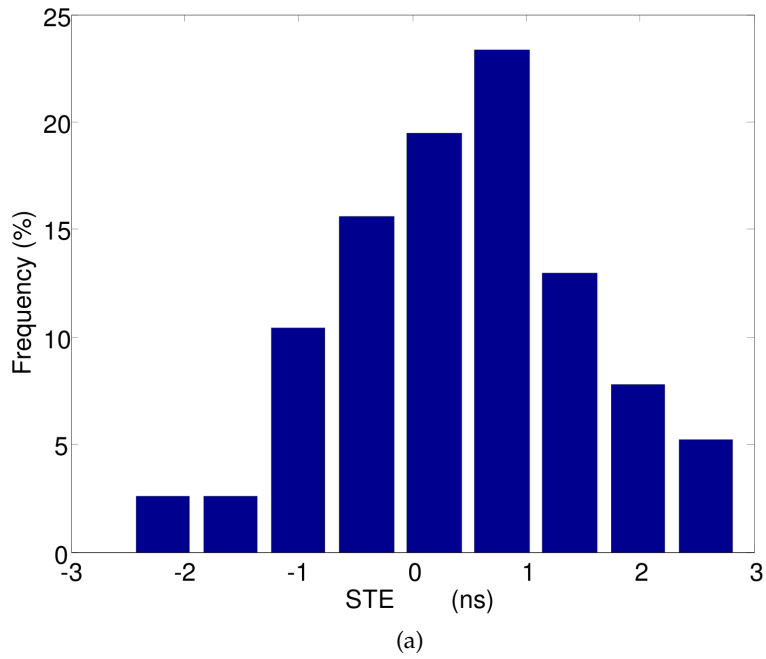


Figure 5.8: Distribution of the symbol timestamping errors in the case of data transfers between two N210 platforms: in (a) $F_s = 8 \text{ MSa/s}$; in (b) $F_s = 16 \text{ MSa/s}$.

- by computing the average of four consecutive subchirp timestamps belonging to the same symbol.

The first solution makes the error due to incoherent sampling and finite clock resolution negligible. The second technique instead has a double benefit: it roughly halves the jitter due to wide-band noise and multipath propagation, and it tends to remove the systematic positive or negative time shifts caused by the frequency offset between transmitter and receiver oscillators. Due to its intrinsic simplicity, the proposed timestamping approach is suitable for a possible on-chip implementation.

CONCLUSION

THE ABILITY to determine the position of objects and people inside of buildings and any other covered structure, where GPS devices typically do not work, is becoming increasingly important. Typical location-enabled applications include but are not limited to:

- A. tracking of equipment and personnel in factories, warehouses and hospitals;
- B. providing location-specific information in museums, library or supermarkets;
- C. controlling access to information and utilities based on users' location;

Another key application is localizing of wireless sensors, in which event detection is useless without some information on *where* such an event occurs.

In this broad applicative scenario, wireless technology represents a viable solution to provide indoors location estimates for any object with embedded radio capability.

Within this context, the work presented in this dissertation faced the following problem: to determine the position of a wireless embedded platform through innovative techniques based on RSS and ToF measurements of RF signals.

Throughout our research we went many steps further towards the solution of the problem. First, we investigated extensively the localization based on RSS measurements. We experimentally analyzed the characteristics of the wireless propagation channel in indoor environment. Then, we evaluated the performance of RSS-based localization algorithms, and analyzed the limitations introduced by ranging error. We therefore developed a novel algorithm which combines the complementary features of RSS and ToF measurements in order to improve the accuracy of distance measurement. Finally, we analyzed a low-level timestamping mechanism based on CSS signals, assessed its efficacy in improving ranging accuracy and, as a side effect, enabling time synchronization.

RSS-based indoor positioning was investigated extensively in [Chapter 3](#). We performed a preliminary systematic study in order to characterize the adopted wireless propagation channel model, i.e., the log-distance path loss model. We demonstrated this model is affected by a quite high relative bias and standard deviation. As a consequence, any distance estimator based on this model is very sensitive to RSS uncertainty. In addition, based on exhaustive measurements, we showed that in indoor cluttered environments the RSS is random, with a primarily left-skewed distribution, contrary to what is commonly assumed in the literature, where the average RSS is modeled by a log-normal distribution which is symmetric around a mean value. We also evidenced that the RSS random process is nonstationary with respect to the distance. Furthermore, we analyzed the accuracy of two classes of positioning algorithms based on the centroid concept, namely WCL and REWL, by means of both theoretical simulations and experimental results. By doing so, we found that the error introduced by the algorithm is usually negligible, whereas the localization error is mainly due to the uncertainty associated with distance estimation.

In [Chapter 4](#) we extended our research on indoor positioning by considering also the ToF-based ranging method. At first, we analyzed and compared in detail the performance limitations of RSS- and two-way ToF-based distance measurement techniques. On the basis of this study, we proposed a data fusion algorithm to combine the complementary features of both methods in order to improve ranging accuracy. The algorithm was implemented and tested on the field using a dedicated embedded prototype made with COTS components. Based on several experimental results, we proved that the combination of both techniques can significantly reduce measurement uncertainty. The proposed solution is absolutely general and it is quite simple and light from the computational point of view.

The study carried out in [Chapter 4](#) provided insights on the fact that ToF measurement accuracy is limited by the joint effect of clock resolution, wideband noise, clock frequency offsets and multipath propagation. If the influence of such phenomena were minimized, and message timestamping was done at the lowest possible level, i.e., when the first bit or the first symbol of a frame were sent or detected by the front-end of the wireless transceiver, ToF uncertainty could be further reduced. One of the most recent and promising communication scheme to reach this goal is CSS modulation. Therefore, in [Chap-](#)

ter 4 we investigated the features of CSS signals for low-level time-stamping, both theoretically and through simulations under the effect of various uncertainty contributions. In order to reduce the effects of such contributions, we proposed an optimal solution for frame time-stamping at the symbol level, thus potentially improving both ranging and, as a side effect, time synchronization. Finally, we performed several experiments by using an SDR implementation of the CSS PHY layer described in the standard IEEE 802.15.4a. The results confirmed that CSS can be successfully adopted both for ranging and time synchronization.

6.1 CONTRIBUTIONS

With particular regard to the topics treated in this research, the major contributions of our work can be summarized as follows:

1. We showed that the log-distance path loss model is characterized by significant relative bias and standard deviation. Thus, any distance estimator based on this model is remarkably sensitive to RSS uncertainty.
2. We presented an extensive analysis of RSS measurements, that revealed characteristics of the RSS and its patterns beyond the general knowledge of the traditional wireless communication. In particular, our measurements highlighted left-skewed distribution for the RSS and suggested a non-stationary behavior for the RSS error with respect to the distance.
3. We found that location measurement uncertainty is mainly due to the noise associated to the channel propagation model, although the error introduced by approximated localization algorithms, such as WCL and REWL, is not negligible.
4. We indicated, supporting by means of experimental results, that the use of RSS-based ranging is preferable in very short range, conversely to the RTT-based technique which looks more promising over a longer range.
5. We proposed and tested on the field a novel data fusion algorithm which, by combining both RSS- and ToF-based ranging methods, significantly reduce distance measurement uncertainty.

6. We introduced the use of CSS signals for accurate frame timestamping, even in the presence of significant nonidealities. This reduces the ToA measurement uncertainty and improves ranging accuracy.

6.2 FUTURE RESEARCH WORK

On the basis of the study, the analysis and the experimental activities carried out in the framework of this thesis, we identified some interesting directions of research as future developments of this work.

- In our opinion a further investigation aimed at improving timestamping accuracy of CSS signals should be carried out. In particular, by using a simple digital parabolic interpolator at the output of the MA associated with each subchirp type.
- Another interesting direction would be the on-chip implementation of the proposed CSS-based timestamping approach.

EQUIVALENCE BETWEEN REWL AND WCL ALGORITHMS

Considering the path loss model given by (2.3), and assuming the noise component \mathbf{w} negligible, the received signal strength experienced by the MT at a distance d_i from FA \mathbf{a}_i can be expressed as

$$s_i = s_0 - 10\eta \log\left(\frac{d_i}{d_0}\right) . \quad (\text{A.1})$$

According to (A.1), the maximum s_{\max} value of the RSS corresponds to the minimum distance d_{\min} between the MT and the FA, i.e.,

$$s_{\max} = s_0 - 10\eta \log\left(\frac{d_{\min}}{d_0}\right) . \quad (\text{A.2})$$

Subtracting (A.1) from (A.2), and replacing (2.3) we obtain, we obtain

$$\hat{p} = \frac{\sum_{i=1}^n \left[(1-\lambda)^{10\eta \log\left(\frac{d_i}{d_{\min}}\right)} \times \mathbf{a}_i \right]}{\sum_{i=1}^n (1-\lambda)^{10\eta \log\left(\frac{d_i}{d_{\min}}\right)}} . \quad (\text{A.3})$$

From which, using the properties of logarithms, we have the following:

$$\hat{p} = \frac{\sum_{i=1}^n \left[\left(\frac{d_i}{d_{\min}}\right)^{10\eta \log(1-\lambda)} \times \mathbf{a}_i \right]}{\sum_{i=1}^n \left(\frac{d_i}{d_{\min}}\right)^{10\eta \log(1-\lambda)}} \quad (\text{A.4})$$

Equation (A.4) reduces to (3.6) defining $g = 10\eta \log(1-\lambda)$. \square

BIBLIOGRAPHY

- [1] K. J. Krizman, T. E. Biedka, and T. S. Rappaport, "Wireless Position Location: Fundamentals, Implementation Strategies, and Sources of Error," in *Proc. 4th IEEE Vehicular Technology Conference (VTC 1997)*, vol. 2, Phoenix, AZ, USA, May 1997, pp. 919–923.
- [2] L. Angrisani, A. Baccigalupi, and R. Schiano Lo Moriello, "Ultrasonic Time-of-flight Estimation through Unscented Kalman Filter," *IEEE Transactions on Instrumentation and Measurement*, vol. 55, no. 4, pp. 1077–1084, Aug. 2006.
- [3] B. Andó and S. Graziani, "Multisensor Strategies to Assist Blind People: A Clear-Path Indicator," *IEEE Transactions on Instrumentation and Measurement*, vol. 58, no. 8, pp. 2488–2494, Aug. 2009.
- [4] D. F. Glas, T. Miyashita, H. Ishiguro, and N. Hagita, "Laser-Based Tracking of Human Position and Orientation Using Parametric Shape Modeling," *Advanced Robotics*, vol. 23, no. 4, pp. 405–428, 2009.
- [5] E. Lobaton, R. Vasudevan, R. Bajcsy, and S. Sastry, "A Distributed Topological Camera Network Representation for Tracking Applications," *IEEE Transactions on Image Processing*, vol. 19, no. 10, pp. 2516–2529, Oct. 2010.
- [6] F. Chavand, E. Colle, Y. Chekhar, and E. C. N'zi, "3-D Measurements Using a Video Camera and a Range Finder," *IEEE Transactions on Instrumentation and Measurement*, vol. 46, no. 6, pp. 1229–1235, Dec. 1997.
- [7] P. Vadakkepat and L. Jing, "Improved Particle Filter in Sensor Fusion for Tracking Randomly Moving Object," *IEEE Transactions on Instrumentation and Measurement*, vol. 55, no. 5, pp. 1823–1832, Dec. 2006.
- [8] A. Bonarini, P. Aliverti, and M. Lucioni, "An Omnidirectional Vision Sensor for Fast Tracking for Mobile Robots," *IEEE Transactions on Instrumentation and Measurement*, vol. 49, no. 3, pp. 509–512, Jun. 2000.

- [9] A. Fod, A. Howard, and M. A. J. Mataric, "A Laser-Based People Tracker," in *Proc. IEEE International Conference on Robotics and Automation (ICRA 2002)*, vol. 3, Washington, DC, USA, May 2002, pp. 3024–3029.
- [10] T. S. Rappaport, *Wireless Communications – Principles and Practice*, 2nd ed. Upper Saddle River, NJ: Prentice Hall PTR, Dec. 2001.
- [11] T. Pavani, G. Costa, M. Mazzotti, A. Conti, and D. Dardari, "Experimental Results on Indoor Localization Techniques through Wireless Sensors Network," in *Proc. IEEE 63rd Vehicular Technology Conference (VTC 2006 - Spring)*, vol. 2, Melbourne, Australia, May 2006, pp. 663–667.
- [12] K. Benkic, M. Malajner, P. Planinsic, and Z. Cucej, "Using RSSI value for distance estimation in wireless sensor networks based on ZigBee," in *Proc. 15th International Conference on Systems, Signals and Image Processing (IWSSIP 2008)*, Bratislava, Slovak Republic, Jun. 2008, pp. 303–306.
- [13] D. Lymberopoulos, Q. Lindsey, and A. Savvides, "An Empirical Characterization of Radio Signal Strength Variability in 3-D IEEE 802.15.4 Networks Using Monopole Antennas," in *Wireless Sensor Networks*, ser. Lecture Notes in Computer Science. Springer Berlin / Heidelberg, 2006, vol. 3868, pp. 326–341.
- [14] K. Whitehouse, C. Karlof, and D. Culler, "A Practical Evaluation of Radio Signal Strength for Ranging-based Localization," *SIGMOBILE Mob. Comput. Commun. Rev.*, vol. 11, pp. 41–52, Jan. 2007.
- [15] E. Elnahrawy, L. Xiaoyan, and R. P. Martin, "The Limits of Localization Using Signal Strength: a Comparative Study," in *Proc. 1st IEEE Communications Society Conference on Sensor and Ad Hoc Communications and Networks (SECON 2004)*, Santa Clara, CA, USA, Oct. 2004, pp. 406–414.
- [16] A. Savvides, H. Park, and M. B. Srivastava, "The Bits and Flops of the n-hop Multilateration Primitive for Node Localization Problems," in *Proc. 1st ACM International Workshop on Wireless Sensor Networks and Applications (WSNA 2002)*, Atlanta, GA, USA, Sep. 2002, pp. 112–121.
- [17] I. Guvenc and C.-C. Chong, "A Survey on TOA Based Wireless Localization and NLOS Mitigation Techniques," *IEEE Communica-*

- tions Surveys & Tutorials*, vol. 11, no. 3, pp. 107–124, Third Quarter 2009.
- [18] J. X. Lee, Z. W. Lin, P. S. Chin, and K. P. Yar, “One-way Ranging Time Drift Compensation for both Synchronized and Non-synchronized Clocks,” in *Proc. International Conference on System Science and Engineering (ICSSE 2010)*, Taipei, Taiwan, Jul. 2010, pp. 327–331.
- [19] Y. Jiang and V. C. M. Leung, “An Asymmetric Double Sided Two-Way Ranging for Crystal Offset,” in *Proc. International Symposium on Signals, Systems and Electronics (ISSSE 2007)*, Montreal, Canada, Jul./Aug. 2007, pp. 525–528.
- [20] D. Wang, R. Kannan, L. Wei, and B. Tay, “Time of Flight based Two Way Ranging for Real-Time Locating Systems,” in *Proc. IEEE International Conference on Robotics, Automation and Mechatronics (RAM 2010)*, Singapore, Jun. 2010, pp. 199–205.
- [21] M. Kwak and J. Chong, “A new Double Two-Way Ranging Algorithm for Ranging System,” in *Proc. 2nd IEEE International Conference on Network Infrastructure and Digital Content (IC-NIDC 2010)*, Beijing, China, Sep. 2010, pp. 470–473.
- [22] A. De Angelis, M. Dionigi, A. Moschitta, and P. Carbone, “A Low-Cost Ultra-Wideband Indoor Ranging System,” *IEEE Transactions on Instrumentation and Measurement*, vol. 58, no. 12, pp. 3935–3942, Dec. 2009.
- [23] J. Zhang, P. V. Orlik, Z. Sahinoglu, A. F. Molisch, and P. Kinney, “UWB Systems for Wireless Sensor Networks,” *Proceedings of the IEEE*, vol. 97, no. 2, pp. 313–331, Feb. 2009.
- [24] C. Röhrig and M. Müller, “Localization of Sensor Nodes in a Wireless Sensor Network Using the nanoLOC TRX Transceiver,” in *Proc. IEEE 69th Vehicular Technology Conference (VTC 2009 - Spring)*, Barcelona, Spain, Apr. 2009, pp. 1–5.
- [25] E. Karapistoli, F.-N. Pavlidou, I. Gragopoulos, and I. Tsetsinas, “An Overview of the IEEE 802.15.4a Standard,” *IEEE Communications Magazine*, vol. 48, no. 1, pp. 47–53, Jan. 2010.
- [26] G. Santinelli, R. Giglietti, and A. Moschitta, “Self-calibrating indoor positioning system based on ZigBee® devices,” in *Proc. IEEE*

- International Instrumentation and Measurement Technology Conference (I2MTC 2009)*, Singapore, May 2009, pp. 1205–1210.
- [27] H. Liu, H. Darabi, P. Banerjee, and J. Liu, "Survey of Wireless Indoor Positioning Techniques and Systems," *IEEE Transactions on Systems, Man, and Cybernetics, Part C: Applications and Reviews*, vol. 37, no. 6, pp. 1067–1080, Nov. 2007.
- [28] Y. Gu, A. Lo, and I. Niemegeers, "A Survey of Indoor Positioning Systems for Wireless Personal Networks," *IEEE Communications Surveys & Tutorials*, vol. 11, no. 1, pp. 13–32, First Quarter 2009.
- [29] R. Want, A. Hopper, V. Falcão, and J. Gibbons, "The Active Badge Location System," *ACM Transactions on Information Systems*, vol. 10, no. 1, pp. 91–102, Jan. 1992.
- [30] A. Ward, A. Jones, and A. Hopper, "A New Location Technique for the Active Office," *IEEE Personal Communications Magazine*, vol. 4, no. 5, pp. 42–47, Oct. 1997.
- [31] J. Hightower, G. Borriello, and R. Want, "SpotON: An indoor 3D location sensing technology based on RF signal strength," University of Washington Computer Science & Engineering, Tech. Rep. 2000-02-02, Feb. 2000.
- [32] P. Bahl and V. N. Padmanabhan, "RADAR: An In-Building RF-based User Location and Tracking System," in *Proc. 19th Annual Joint Conference of the IEEE Computer and Communications Societies (INFOCOM 2000)*, vol. 2, Tel-Aviv, Israel, Mar. 2000, pp. 775–784.
- [33] (2012, Oct.). [Online]. Available: <http://www.ubisense.net>
- [34] G. Chandrasekaran, M. A. Ergin, J. Yang, S. Liu, Y. Chen, M. Gruteser, and R. P. Martin, "Empirical Evaluation of the Limits on Localization Using Signal Strength," in *Proc. 6th Annual IEEE Communications Society Conference on Sensor, Mesh and Ad Hoc Communications and Networks (SECON 2009)*, Rome, Italy, Jun. 2009, pp. 1–9.
- [35] R. Peng and M. L. Sichitiu, "Probabilistic Localization for Outdoor Wireless Sensor Networks," *SIGMOBILE Mob. Comput. Commun. Rev.*, vol. 11, pp. 53–64, Jan. 2007.
- [36] K. Yedavalli, B. Krishnamachari, S. Ravula, and B. Srinivasan, "Ecolocation: A Sequence Based Technique for RF Localization in

- Wireless Sensor Networks,” in *Proc. 4th International Symposium on Information Processing in Sensor Networks (IPSN 2005)*, Los Angeles, CA, USA, Apr. 2005, pp. 285–292.
- [37] K. Langendoen and N. Reijers, “Distributed localization in wireless sensor networks: a quantitative comparison,” *Computer Networks*, vol. 43, no. 4, pp. 499–518, Nov. 2003.
- [38] J. Shirahama and T. Ohtsuki, “RSS-Based Localization in Environments with Different Path Loss Exponent for Each Link,” in *Proc. IEEE 67th Vehicular Technology Conference (VTC 2008 - Spring)*, Singapore, May 2008, pp. 1509–1513.
- [39] J. Polastre, R. Szewczyk, and D. Culler, “Telos: Enabling Ultra-low Power Wireless Research,” in *Proc. 4th International Symposium on Information Processing in Sensor Networks (IPSN 2005)*, Los Angeles, CA, USA, Apr. 2005, pp. 364–369.
- [40] JCGM, *Evaluation of Measurement Data – Guide to the Expression of Uncertainty in Measurement*, JCGM 100:2008. Geneva, Switzerland: JCGM, Sep. 2008.
- [41] T. He, C. Huang, B. M. Blum, J. A. Stankovic, and T. Abdelzaher, “Range-Free Localization Schemes for Large Scale Sensor Networks,” in *Proc. 9th Annual International Conference on Mobile Computing and Networking (MobiCom 2003)*, San Diego, CA, USA, Sep. 2003, pp. 81–95.
- [42] H. Chen, Q. Shi, R. Tan, H. V. Poor, and K. Sezaki, “Mobile Element Assisted Cooperative Localization for Wireless Sensor Networks with Obstacles,” *IEEE Transactions on Wireless Communications*, vol. 9, no. 3, pp. 956–963, Mar. 2010.
- [43] N. Bulusu, J. Heidemann, and D. Estrin, “GPS-less Low-Cost Outdoor Localization for Very Small Devices,” *IEEE Personal Communications Magazine*, vol. 7, no. 5, pp. 28–34, Oct. 2000.
- [44] J. Blumenthal, R. Grossmann, F. Golatowski, and D. Timmermann, “Weighted Centroid Localization in Zigbee-based Sensor Networks,” in *Proc. IEEE International Symposium on Intelligent Signal Processing (WISP 2007)*, Alcala de Henares, Spain, Oct. 2007, pp. 1–6.
- [45] C. Laurendeau and M. Barbeau, “Relative Span Weighted Localization of Uncooperative Nodes in Wireless Networks,” in *Proc.*

- 4th International Conference on Wireless Algorithms, Systems and Applications (WASA 2009)*, Boston, MA, USA, Aug. 2009.
- [46] D. Dardari, A. Conti, U. Ferner, A. Giorgetti, and M. Z. Win, "Ranging With Ultrawide Bandwidth Signals in Multipath Environments," *Proceedings of the IEEE*, vol. 97, no. 2, pp. 404–426, Feb. 2009.
- [47] D. L. Hall and J. Llinas, "An introduction to multisensor data fusion," *Proceedings of the IEEE*, vol. 85, no. 1, pp. 6–23, Jan. 1997.
- [48] D. Macii, A. Boni, M. De Cecco, and D. Petri, "Multisensor Data Fusion," *IEEE Instrumentation and Measurement Magazine*, vol. 11, no. 3, pp. 24–33, Jun. 2008.
- [49] A. Catovic and Z. Sahinoglu, "The Cramér-Rao Bounds of Hybrid TOA/RSS and TDOA/RSS Location Estimation Schemes," *IEEE Communications Letters*, vol. 8, no. 10, pp. 626–628, Oct. 2004.
- [50] A. Hatami and K. Pahlavan, "QRPP1-5: Hybrid TOA-RSS Based Localization Using Neural Networks," in *Proc. IEEE Global Telecommunications Conference (GLOBECOM 2006)*, San Francisco, CA, USA, Nov./Dec. 2006, pp. 1–5.
- [51] C. Fritsche and A. Klein, "Cramér-Rao Lower Bounds for hybrid localization of mobile terminals," in *Proc. 5th Workshop on Positioning, Navigation and Communication (WPNC 2008)*, Mar. 2008, pp. 157–164.
- [52] A. Bahillo, S. Mazuelas, R. M. Lorenzo, P. Fernández, J. Prieto, R. J. Durán, and E. J. Abril, "Hybrid RSS-RTT Localization Scheme for Indoor Wireless Networks," *EURASIP Journal on Advances in Signal Processing*, vol. 2010, no. 1, pp. 1–12, Apr. 2010.
- [53] D. Macii, P. Pivato, and F. Trenti, "A Robust Wireless Proximity Detection Techniques based on RSS and ToF measurements," in *Proc. IEEE International Workshop on Measurement and Networking (M&N 2011)*, Anacapri, Italy, Oct. 2011, pp. 31–36.
- [54] J. D. Gibson, *The Mobile Communication Handbook*, 1st ed. New York: CRC Press, Feb. 1996.
- [55] Y. Lustmann and D. Porrat, "Indoor Channel Spectral Statistics, K-Factor and Reverberation Distance," *IEEE Transactions on Antennas and Propagation*, vol. 58, no. 11, pp. 3685–3692, Nov. 2010.

- [56] V. Nikolopoulos, M. Fiacco, S. Stavrou, and S. R. Saunders, "Narrowband Fading Analysis of Indoor Distributed Antenna Systems," *IEEE Antennas and Wireless Propagation Letters*, vol. 2, no. 1, pp. 89–92, Jan. 2003.
- [57] D. Puccinelli and M. Haenggi, "Multipath Fading in Wireless Sensor Networks: Measurements and Interpretation (IWCMC 2006)," in *Proc. 3rd International Wireless Communications and Mobile Computing Conference (IWCMC 2006)*, Vancouver, Canada, Jul. 2006, pp. 1039–1044.
- [58] S. Wyne, T. Santos, F. Tufvesson, and A. F. Molisch, "Channel Measurements of an Indoor Office Scenario for Wireless Sensor Applications," in *Proc. IEEE Global Telecommunications Conference (GLOBECOM 2007)*, Washington, DC, USA, Nov. 2007, pp. 3831–3836.
- [59] C. M. De Dominicis, P. Ferrari, A. Flammini, and E. Sisinni, "Wireless Sensors Exploiting IEEE802.15.4a for Precise Timestamping," in *Proc. International IEEE Symposium on Precision Clock Synchronization for Measurement, Control and Communication (ISPCS 2010)*, Portsmouth, NH, USA, Sep./Oct. 2010, pp. 48–54.
- [60] S. W. Smith, *Digital Signal Processing: A Practical Guide for Engineers and Scientists*. Newnes, Nov. 2002.
- [61] F. Stefani, M. Moschitta, D. Macii, P. Carbone, and D. Petri, "Fast estimation of ADC nonlinearities using the Sinewave Histogram Test," *Measurement*, vol. 39, no. 3, pp. 232–237, Apr. 2006.
- [62] D. Macii, L. Mari, and D. Petri, "Comparison of Measured Quantity Value Estimators in Nonlinear Models," *IEEE Transactions on Instrumentation and Measurement*, vol. 59, no. 1, pp. 238–246, Jan. 2010.
- [63] G. Arechavaleta, J.-P. Laumond, H. Hicheur, and A. Berthoz, "The Nonholonomic Nature of Human Locomotion: a Modeling Study," in *Proc. 1st IEEE/RAS-EMBS International Conference on Biomedical Robotics and Biomechatronics (BioRob 2006)*, Pisa, Italy, Feb. 2006, pp. 158–163.
- [64] Y. Bar-Shalom, X. Rong Li, and T. Kirubarajan, *Estimation with Applications to Tracking and Navigation: Theory, Algorithms and Software*. John Wiley & Sons, Inc., Jul. 2001.

- [65] *IEEE Standard for Information technology - Telecommunications and information exchange between systems - Local and metropolitan area networks - Specific requirements - Part 15.4: Wireless Medium Access Control (MAC) and Physical Layer (PHY) Specifications for Low-Rate Wireless Personal Area Networks (WPANs)*, IEEE Standard 802.15.4-2006, Rev. of IEEE Standard 802.15.4-2003, Sep. 2006.
- [66] P. Pivato, S. Dalpez, and D. Macii, "Performance Evaluation of Chirp Spread Spectrum Ranging for Indoor Embedded Navigation Systems," in *Proc. 7th IEEE International Symposium on Industrial Embedded Systems (SIES 2012)*, Karlsruhe, Germany, Jun. 2012, pp. 1–4.
- [67] J.-Y. Lee and R. A. Scholtz, "Ranging in a Dense Multipath Environment Using an UWB Radio Link," *IEEE Journal on Selected Areas in Communications*, vol. 20, no. 9, pp. 1677–1683, Dec. 2002.
- [68] C. M. De Dominicis, A. Flammini, S. Rinaldi, E. Sisinni, A. Cazzorla, A. Moschitta, and P. Carbone, "High-precision UWB-based timestamping," in *Proc. International IEEE Symposium on Precision Clock Synchronization for Measurement, Control and Communication (ISPCS 2011)*, Munich, Germany, Sep. 2011, pp. 50–55.
- [69] *IEEE Standard for Information technology - Telecommunications and information exchange between systems - Local and metropolitan area networks - Specific requirements - Part 15.4: Wireless Medium Access Control (MAC) and Physical Layer (PHY) Specifications for Low-Rate Wireless Personal Area Networks (WPANs)*, IEEE Standard 802.15.4a-2007, Amendment to IEEE Standard 802.15.4-2006, Sep. 2007.
- [70] H.-S. Ahn, H. Hur, and W.-S. Choi, "One-way Ranging Technique for CSS-based Indoor Localization," in *Proc. 6th IEEE International Conference on Industrial Informatics (INDIN 2008)*, Daejeon, Korea, Jul. 2008, pp. 1513–1518.
- [71] K. Römer and F. Mattern, "Towards a unified view on space and time in sensor networks," *Computer Communications*, vol. 28, no. 13, pp. 1484–1497, Aug. 2005.
- [72] C.-Y. Chong and S. P. Kumar, "Sensor Networks: Evolution, Opportunities, and Challenges," *Proceedings of the IEEE*, vol. 91, no. 8, pp. 1247–1256, Aug. 2003.
- [73] D. Macii, A. Ageev, and L. Abeni, "An Energy Saving Criterion for Wireless Sensor Networks with Time Synchronization

- Requirements," in *Proc. 5th IEEE International Symposium on Industrial Embedded Systems (SIES 2010)*, Trento, Italy, Jul. 2010, pp. 166–173.
- [74] J. Zheng and Y.-C. Wu, "Joint Time Synchronization and Localization of an Unknown Node in Wireless Sensor Networks," *IEEE Transactions on Signal Processing*, vol. 58, no. 3, pp. 1309–1320, Mar. 2010.
- [75] M. Maróti, B. Kusy, G. Simon, and A. Lédeczi, "The Flooding Time Synchronization Protocol," in *Proc. 2nd ACM Conference on Embedded Networked Sensor Systems (SenSys 2004)*, Baltimore, MD, USA, Nov. 2004, pp. 39–49.
- [76] S. Yoon, C. Veerarittiphan, and M. L. Sichitiu, "Tiny-sync: Tight Time Synchronization for Wireless Sensor Networks," *ACM Trans. Sen. Netw. (TOSN)*, vol. 3, no. 2, pp. 1–33, Jun. 2007.
- [77] L. Schenato and F. Fiorentin, "Average TimeSynch: A consensus-based protocol for clock synchronization in wireless sensor networks," *Automatica*, vol. 47, no. 9, pp. 1878–1886, Sep. 2011.
- [78] P. Ferrari, A. Flammini, D. Marioli, S. Rinaldi, and E. Sisinni, "On the Implementation and Performance Assessment of a WirelessHART Distributed Packet Analyzer," *IEEE Transactions on Instrumentation and Measurement*, vol. 59, no. 5, pp. 1342–1352, May 2010.
- [79] J. Elson, L. Girod, and D. Estrin, "Fine-Grained Network Time Synchronization using Reference Broadcasts," in *Proc. 5th Symposium on Operating Systems Design and Implementation (OSDI 2002)*, vol. 36. Boston, MA, USA: ACM, Dec. 2002, pp. 147–163.
- [80] *IEEE Standard for a Precision Clock Synchronization Protocol for Networked Measurement and Control Systems*, IEEE Standard 1588-2008, Rev. of IEEE Standard 1588-2002, Jul. 2008.
- [81] T. Cooklev, J. C. Eidson, and A. Pakdaman, "An Implementation of IEEE 1588 Over IEEE 802.11b for Synchronization of Wireless Local Area Network Nodes," *IEEE Transactions on Instrumentation and Measurement*, vol. 56, no. 5, pp. 1632–1639, Oct. 2007.
- [82] A. Mahmood and G. Gaderer, "Timestamping for IEEE 1588 based Clock Synchronization in Wireless LAN," in *Proc. International IEEE Symposium on Precision Clock Synchronization for Mea-*

- urement, Control and Communication (ISPCS 2009)*, Brescia, Italy, Oct. 2009, pp. 1–6.
- [83] A. Mahmood, G. Gaderer, H. Trsek, S. Schwalowsky, and N. Kero, “Towards High Accuracy in IEEE 802.11 based Clock Synchronization using PTP,” in *Proc. International IEEE Symposium on Precision Clock Synchronization for Measurement, Control and Communication (ISPCS 2011)*, Munich, Germany, Sep. 2011, pp. 13–18.
- [84] C. M. De Dominicis, P. Ferrari, E. Sisinni, A. Flammini, P. Pivato, and D. Macii, “Timestamping Performance Analysis of IEEE 802.15.4a Systems based on SDR Platforms,” in *Proc. IEEE International Instrumentation and Measurement Technology Conference (I2MTC 2012)*, Graz, Austria, May 2012, pp. 2034–2039.
- [85] M. I. Skolnik, *Radar Handbook*, 3rd ed. McGraw-Hill, Jan. 2008.
- [86] G. Jacovitti and G. Scarano, “Discrete Time Techniques for Time Delay Estimation,” *IEEE Transactions on Signal Processing*, vol. 41, no. 2, pp. 525–533, Feb. 1993.
- [87] C. Yoon and H. Cha, “Experimental analysis of IEEE 802.15.4a CSS ranging and its implications,” *Computer Communications*, vol. 34, no. 11, pp. 1361–1374, Jul. 2011.
- [88] D. Lu and D. Rutledge, “Investigation of Indoor Radio Channels from 2.4 GHz to 24 GHz,” in *Proc. IEEE Antennas and Propagation Society International Symposium*, vol. 2, Columbus, OH, USA, Jun. 2003, pp. 134–137.
- [89] H. Hashemi, “The Indoor Radio Propagation Channel,” *Proceedings of the IEEE*, vol. 81, no. 7, pp. 943–968, Jul. 1993.
- [90] (2012, Oct.) GNU Radio. [Online]. Available: <http://gnuradio.org>

COLOPHON

This document was typeset with L^AT_EX 2_ε using the typographical style classicthesis developed by André Miede.

